

CHAPTER 4

SIMULATION

The data collected by the ATLAS experiment must be compared to a well understood dataset. This dataset is most often a dataset of simulation particle collisions that approximate to great precision physics processes and particle interaction with detector material, as well as the detector's response. Figure 4.1 shows the chain of simulations by which these datasets are produced.

Many particle physics experiments, ATLAS included, use Monte Carlo (MC) simulation techniques to produce these datasets. Monte Carlo simulation techniques use repeated random sampling of underlying probability density functions to closely model various processes.

4.1 Event Generation and Hadronization

Since protons and other hadrons are not fundamental particles, it is impossible to know the exact constituents (partons) that interacted during a collision. To mimic this intrinsic probabilistic nature, Parton Distribution Functions (PDFs) are used. A Parton Distribution Function (PDF) models the probability of any parton within a proton (or hadron) to carry a fraction of the beam energy at a given hadron momentum. The PDF and subsequent inelastic hard scattering of the interacting partons are modeled via a Matrix Element (ME) calculation, which can be depicted through Feynman diagrams. This ME calculation is done to fixed order in perturbation theory, Leading Order (LO), Next-to-Leading Order (NLO), Leading-Logarithmic Order (LL), etc. This first level event generation can be done by a

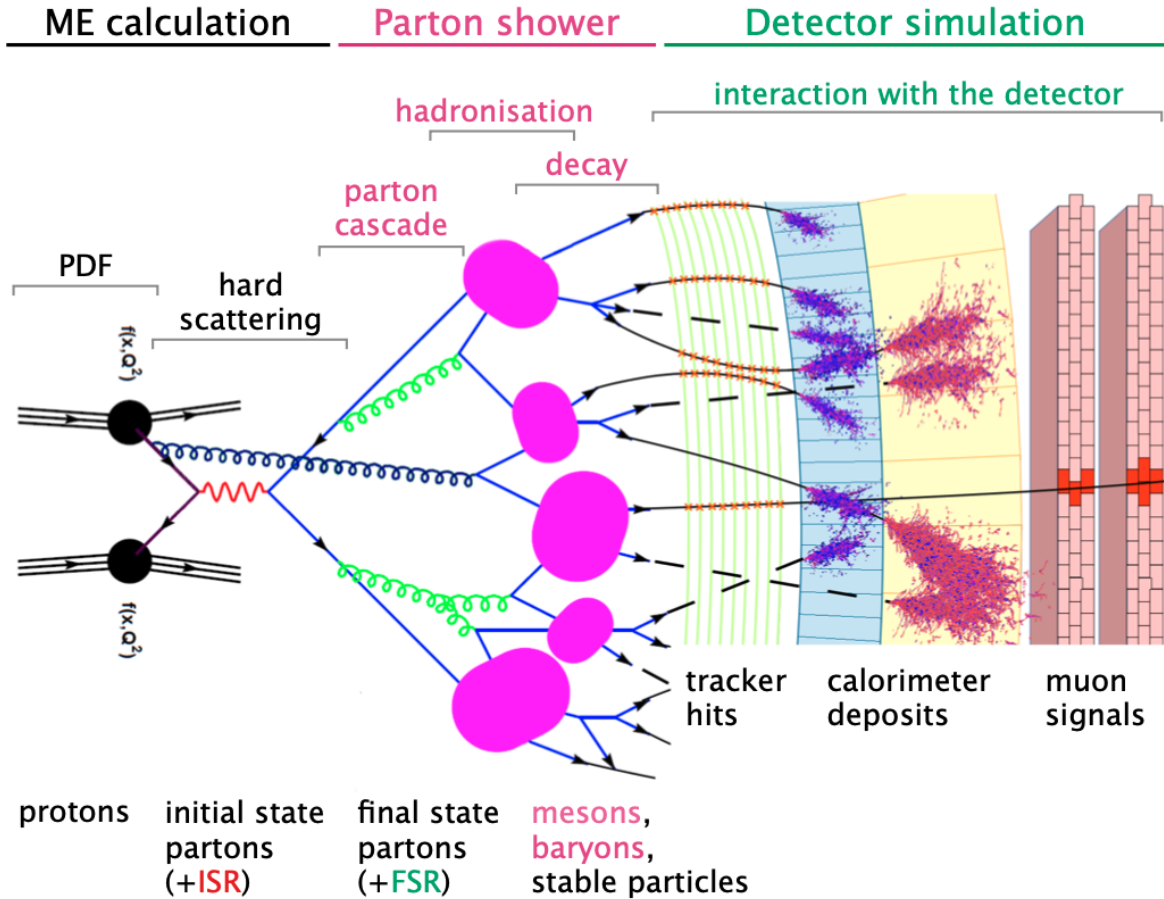


Figure 4.1: A pictorial representation of the simulation chain used in the ATLAS experiment [36].

myriad of MC event generators. Often specific choices are made based on individual generator performance for a given physics process.

The next step in the simulation chain is the parton showering and hadronization. This can be done with a different set of MC simulations. Parton showering and hadronization are complex, computationally expensive steps to simulate and are done iteratively. An example of a parton shower generator output can be seen in Figure 4.2.

The MC generators used in this dissertation are Pythia [37], Powheg-Box [38, 39], and Sherpa [40].

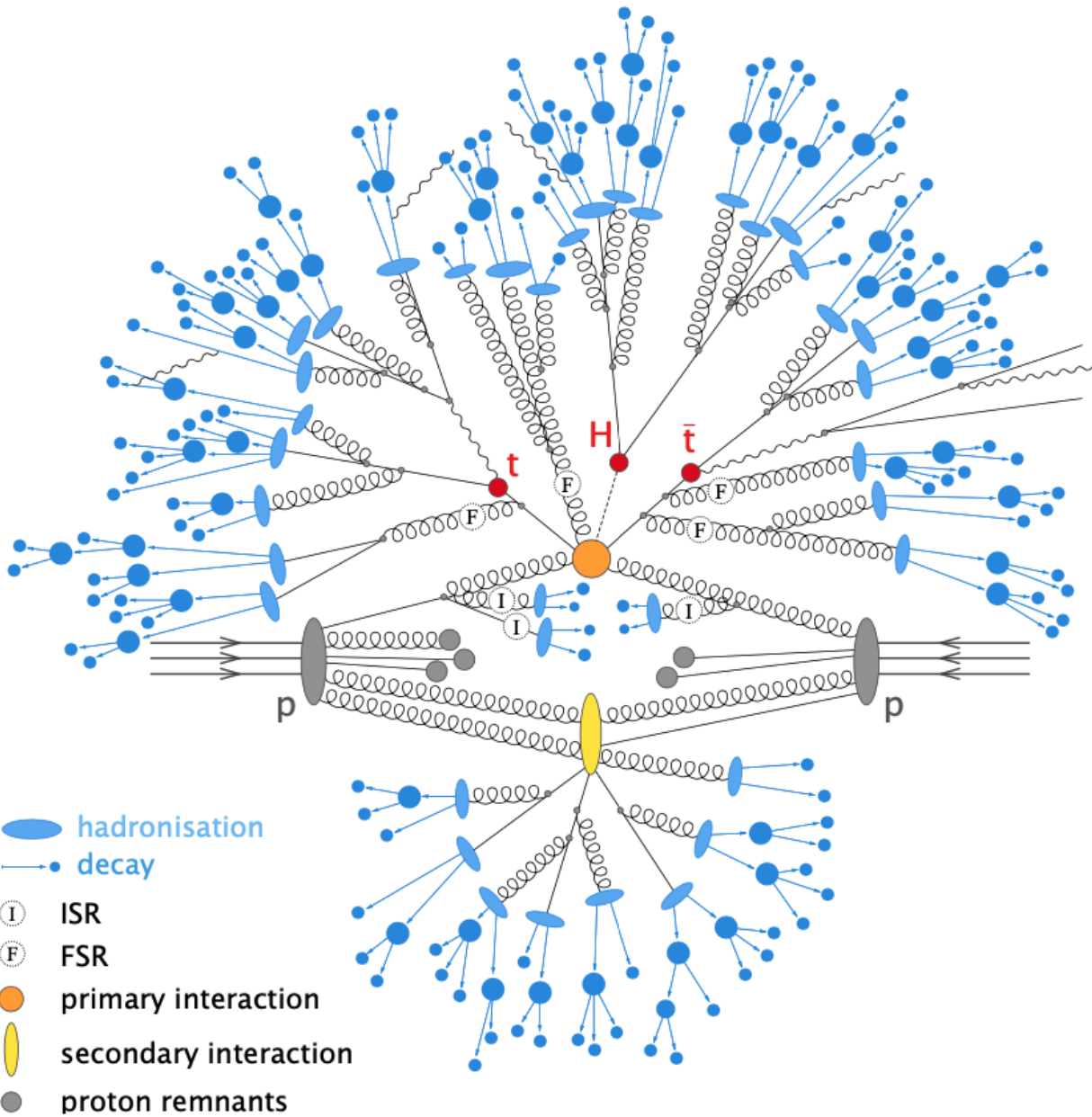


Figure 4.2: A pictorial representation of a parton shower of a $t\bar{t}H$ event [36].

4.2 Detector Simulation

The final step in the simulation chain is simulating the particle's interaction with the detector material and the detector's response. Up until this point, the MC generators used are generic non-experiment dependent simulations. The ATLAS collaboration uses a GEANT4 based generator suite to simulate these interactions [41]. These detailed simulations include all support structure, material densities, readout electronics, and digitization in order to fully simulate the path of a real particle through the ATLAS detector. In fact, these simulations are often too detailed to produce enough statistics for physics analyses. In the full simulation, around 80% of the simulation time is spent on particles traversing the calorimeters and 75% is spent on electromagnetic particles alone [42]. Instead, several methods were developed to speed up the simulation known as FAST simulations. A detailed description of the ATLAS simulation chain and options can be seen in [42]. The final simulated dataset is output into a raw data format identical to real data coming off of the ATLAS detector.

CHAPTER 5

EVENT RECONSTRUCTION

Before any physics analysis can be performed on the raw data from the ATLAS detector or MC simulations the raw datasets go through a reconstruction software suite called Athena [43]. Various algorithms are employed to identify energy deposits as particles based on shower shapes, tracker hits, calculated charge to mass ratios, etc. Figure 5.1 shows the signatures of various particles within the ATLAS detector.

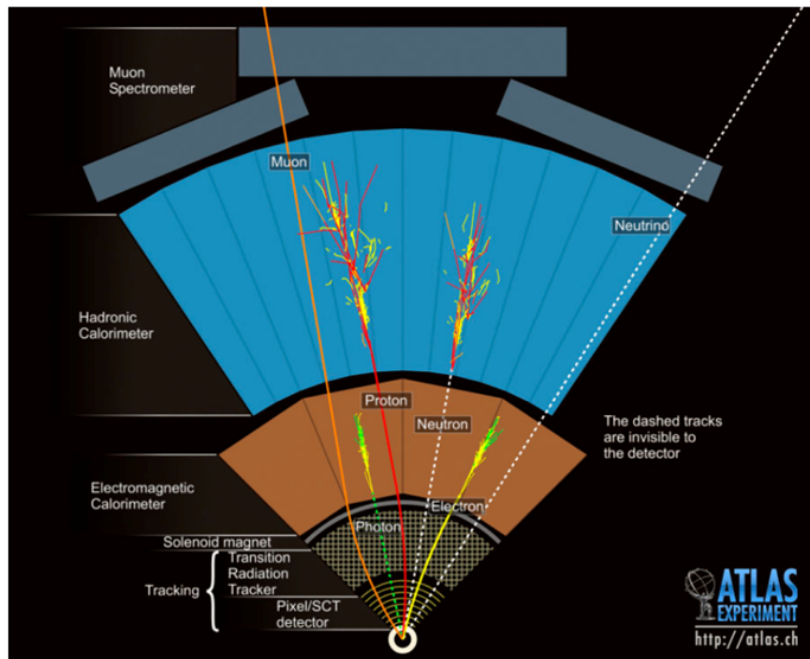


Figure 5.1: Cross section view of the ATLAS detector with subdetectors labeled. Various types of particles radial trajectories are shown [31].

The following sections detail the identification processes of muons, electrons, photons, jets, τ leptons, and a calculated quantity called missing transverse energy (E_T^{miss}). These reconstructed physics objects are the inputs to the majority of physics analyses.

5.1 Tracks

Tracks are fit-connected three-dimensional space-points in the ID. These space-points are created from clusters of hits in the  A set of three space-points are combined into one track seed, then fed into three methods in the ATLAS detector: inside-out, outside-in, and TRT-standalone. The inside-out method creates tracks by starting with a seed hit in the pixel detector, then SCT hits are added, finally the track is extrapolated out into the TRT. This method creates tracks of particles that are mostly produced in the hard pp interaction and has a requirement of $p_T > 400$ MeV. On the other-hand the outside-in method starts with track segments in the TRT and extrapolates towards the beamline using silicon that were not used in the inside-out method. Outside-in tracking typically reconstructs secondary vertices from particles that have long enough lifetimes to decay while inside the ID, including b quarks and τ leptons. Lastly, TRT-standalone tracks are made only from seeds within the TRT and are not extrapolated to the silicon subdetectors [44]. The reconstructed tracks are used in the identification of various types of particles.

5.2 Topological Clusters

A topocluster is defined as a cluster of topologically connected calorimeter cell signals. Topological clusters in the ATLAS detector’s calorimeters are vital to the identification of hadronic final states, meaning jets (Section 5.5), isolated hadrons, and hadronically decaying τ leptons (Section 5.6). Topoclusters are also included in the calculation of missing transverse energy discussed in Section 5.7, as they represent the direction and energy of softer particles in a collision event.

A topocluster is created via a growing volume algorithm that operates based on a set of three thresholds. These thresholds are defined using the calorimeter cell significance ξ_{cell} [45]:

$$\xi_{cell} = \frac{E_{cell}}{\sigma_{noise,cell}} \quad (5.1)$$

where E_{cell} is the energy in the calorimeter cell and $\sigma_{noise,cell}$ is the average expected noise of a given calorimeter cell. An in-depth review of how the $\sigma_{noise,cell}$ value is calculated for TileCal is given in Appendix A. A topocluster starts with a seed cell that has a significance greater than the seed threshold S . From the seed cell, all three-dimensionally neighboring cells with a significance greater than the growth threshold N are added to the topocluster. This is done repeatedly until there are no more neighboring cells that pass the requirement $|\xi_{cell}| > N$. If a neighboring cell also passes the $|\xi_{cell}| > S$ threshold, then the topocluster corresponding to the neighbor cell is merged into the original topocluster. Finally, a last layer of the topocluster is added from all neighboring cells passing a threshold of $|\xi_{cell}| > P$. In the ATLAS experiment, the threshold values are set at $(S, N, P) = (4, 2, 0)$.

5.3 Muon Identification

Muons are identified using a combination of information from the ID and the MS. Within the ID, muons leave tracks identical to any other charged particle; however, in the MS tracks are identified within the MDTs through a straight-line fit in a single layer and by doing a combinatorial search of CSC hits in the $\eta - \phi$ plane [46]. Muons are identified through five strategies, each using the information from the ID, MS, and calorimeter (in one case).

- Combined (CB): Match ID and MS tracks. Perform a combined track fit on ID and MS hits. Takes into account energy loss in calorimeters

- Inside-Out (IO): Extrapolate ID tracks, look for at least three loosely aligned MS hits. Calorimeter energy loss is accounted for.
- Muon Spectrometer Extrapolated (ME): Extrapolate MS tracks back to the beamline. No ID hits are taken into account.
- Segmented-Tagged (ST): Extrapolate ID tracks and match to MS segments with tight angular requirements. Muon parameters are taken directly from the ID.
- Calorimeter-Tagged (CT): Extrapolate ID tracks into the calorimeters. Look for energy deposits consistent with minimum ionizing particles. Tag as muon, take parameters from ID.

All muon identification strategies have a transverse momentum cut on ID tracks of $p_T^{track} > 2$ GeV, except for CT, which has a cut on the transverse momentum of the tracks of $p_T^{track} > 5$ GeV.

Reconstructed muons are divided into three Working Points (WPs) to allow analyzers a choice of purity, efficiency, and background rejection [46]. 

- Loose: Optimized for reconstruction of $H \rightarrow 4\mu$. Lowest purity and highest efficiency.
- Medium: Efficiency and purity are suitable for a wide range of analyses with small systematic uncertainties.
- Tight: High purity, slightly lower efficiency than medium WP. Significantly higher background rejection.

The analysis discussed in this dissertation uses the Loose WP for muons to allow for larger statistics in the signal region.

To ensure muons originated at a hard-scatter and discriminate them from muons in hadronic decays an isolation requirement is applied. The isolation is defined as the transverse

energy (momentum) inside a reconstructed cone around the muon divided by the muon p_T [33]. This isolation can be calculated either using calorimeter information (energy) or ID information (momentum). As with identification, several isolation WPs are defined. This dissertation uses a tight isolation requirement.

5.4 $e\gamma$ Identification

Electrons and photons deposit the majority of their energy in the EM calorimeters in similar fashion. Electrons produce Bremsstrahlung photons as they interact with the EM calorimeter, the produced photons then convert into an electron-positron pair. This process repeats and produces a shower. A photon that is produced in the ID and travels to the EM calorimeters creates a very similar shower by converting into an electron-antielectron (positron) pair. The discerning difference between an electron's signature and that of a photon is angular matching tracks. An electron carries an EM charge, thus leaving a track in the ID; whereas a photon does not carry an EM charge, therefore does not leave a track. The process of identifying an EM shower as either electron initiated or photon initiated is detailed in Ref [47]. A brief algorithm flow chart of this process can be seen in Figure 5.2. If tracks in the ID are found to match a topocluster in the EM calorimeter, then it is identified as an electron, re-clustered into so called superclusters to ensure the full shower is captured, calibrated, then lastly made into an analysis object for use in physics analyses. The same algorithm is used to identify photons with the exception of matching tracks to the ID. Instead, photons are matched to conversion vertices where the initial photon first converted into an electron-positron pair. Both electrons and photons are reconstructed at three WPs. As with muons, there are three WPs, Loose, Medium, and Tight; the stricter WPs being subsets of the looser WPs.

To ensure that an electron or photon is indeed an initial particle and not part of another shower, whether it be from a converted photon in a hadron decay, electrons from heavy flavor hadrons or a light hadron mis-identified as an electron, an isolation variable is calculated. The isolation variable is based on track isolation and defined as the sum of transverse momenta of all tracks within a cone around the electron candidate of $\Delta R = 0.2$ or in the case of high energy photons, $10 \text{ GeV}/E_T$, where E_T is the transverse energy of the electron.

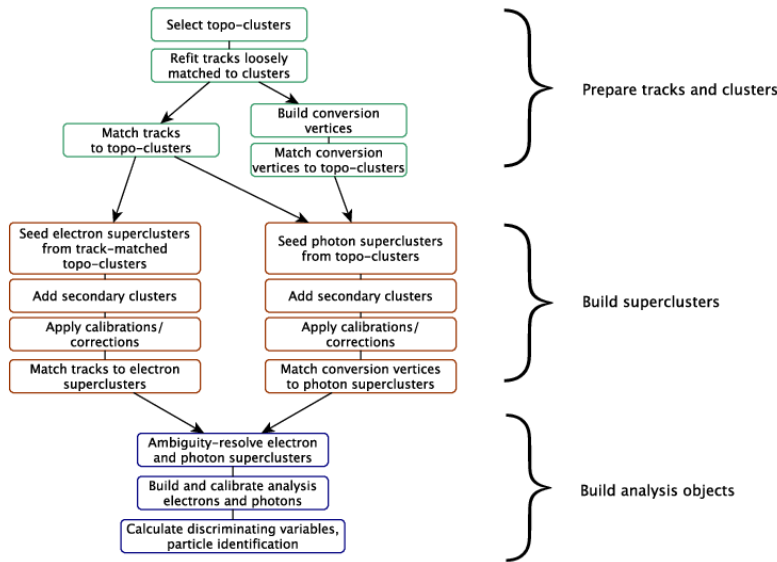


Figure 5.2: Algorithm flow diagram for the electron and photon reconstruction [47].

5.5 Jets

A jet is a reconstructed object of calorimeter energy¹ that is meant to capture the energy and direction of a hadronic shower, typically initiated from hard scatter quarks, hadrons, or gluons. There are several algorithms available to perform a clustering of calorimeter

¹The jet objects in this dissertation use the particle flow algorithm that includes track objects in the full jet energy calculation.

topoclusters to form jets. This dissertation uses jets created from particle flow objects. The particle flow algorithm is described in detail in Ref. [48], a flow chart of the algorithm is shown in Figure 5.3 and an idealized example of the particle flow algorithm performing the reconstruction of hadrons is shown in Figure 5.4.

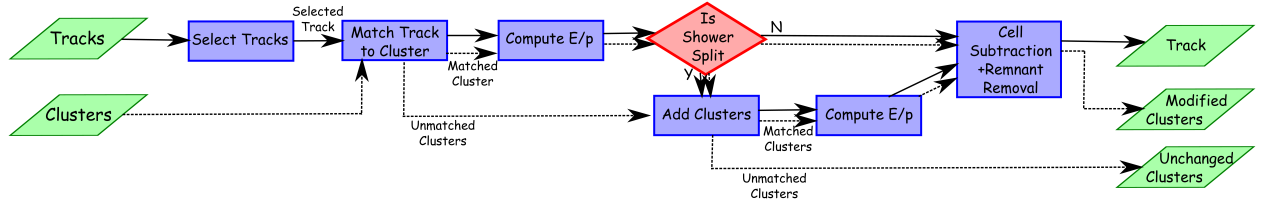


Figure 5.3: A flow chart of how the particle flow algorithm proceeds, starting with track selection and continuing until the energy associated with the selected tracks has been removed from the calorimeter. At the end, charged particles, topoclusters which have not been modified by the algorithm, and remnants of topoclusters which have had part of their energy removed [48].

The particle flow algorithm starts by matching selected tracks to a single topocluster. The expected energy of the initial particle in the calorimeter is calculated from the track momentum and the topocluster position. The probability of the track-topocluster system being deposited in multiple topoclusters is then calculated. The algorithm then adds in more topoclusters to the output object based on this probability. The expected energy of the initial particle is subtracted from the energy of the matched topoclusters cell by cell. If the energy of the output object is consistent with a single particle signal, then the remaining topocluster remnants are removed. The outputs of the particle flow algorithm are then fed into the anti- k_t algorithm [49] with a radius value of $R = 0.4$.

The anti- k_t algorithm is a jet finding algorithm that is collinear and infrared safe, meaning the number of identified jets does not change due to splitting or merging of high transverse momentum particles, nor the presence of soft gluon emission between jets [50]. A jet is constructed in the anti- k_t algorithm through an iterative process using a the distance parameter defined as

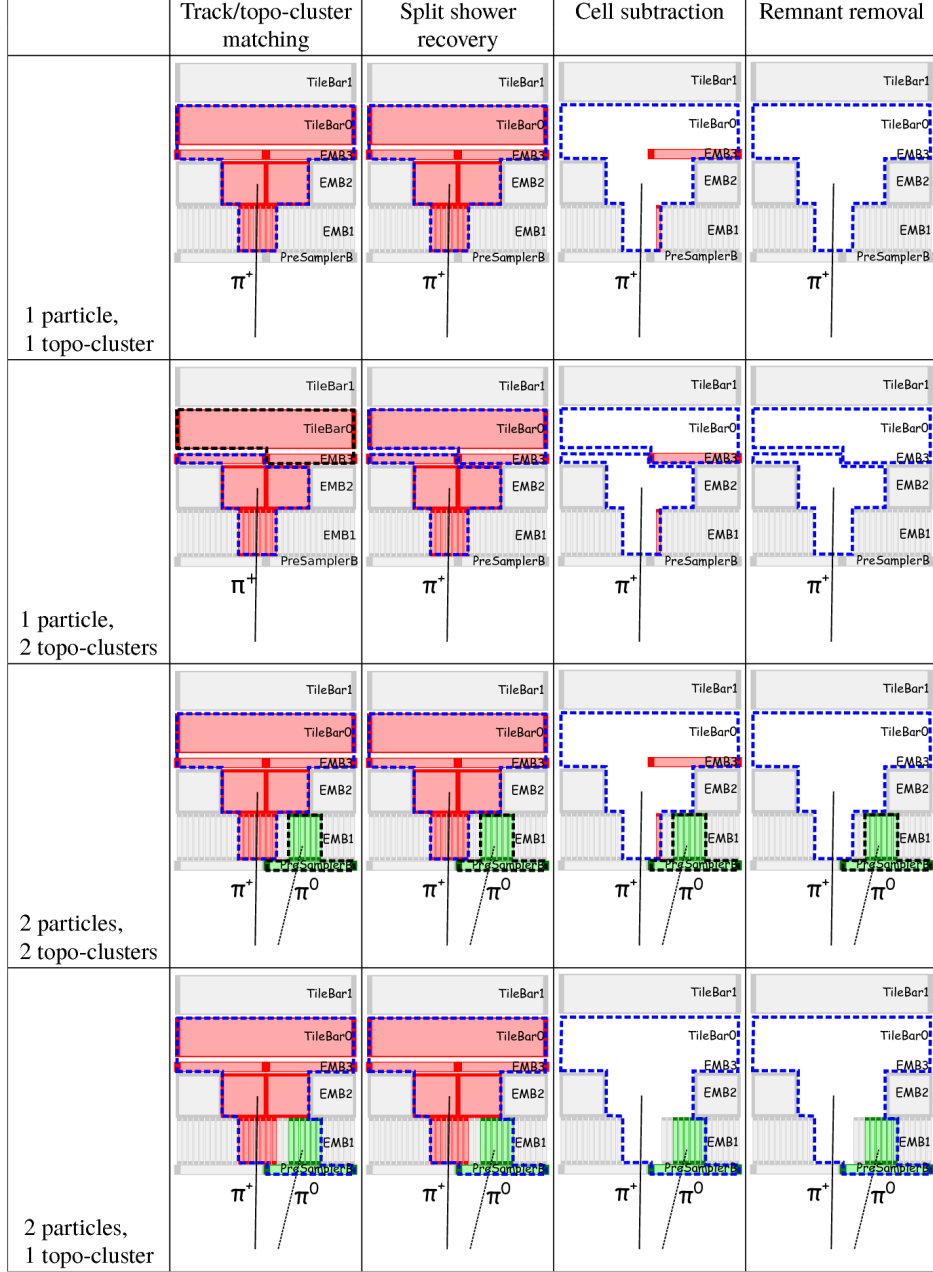


Figure 5.4: Idealized examples of how the algorithm is designed to deal with several different cases. The red cells are those which have energy from the π^+ , the green have cells energy from the photons in the π^0 decay, the dotted lines represent the original topocluster boundaries with those outlined in blue having been matched by the algorithm to the π^+ , while those in black are yet to be selected. The different layers in the EM calorimeter (Presampler, EMB1, EMB2, EMB3) are indicated. In this sketch only the first two layers of the Tile calorimeter are shown (TileBar0 and TileBar1) [48].

$$d_{ij} = \min(k_{t,i}^{-2}, k_{t,j}^{-2}) \frac{\Delta_{ij}^2}{R^2} \quad (5.2)$$

where k_t is the transverse momentum, R is an input parameter defining the radius of the jet cone, and Δ_{ij} is the distance between objects i and j defined as

$$\Delta_{ij} = (y_i - y_j)^2 + (\phi_i - \phi_j)^2 \quad (5.3)$$

The anti- k_t algorithm first identifies the smallest d_{ij} and clusters the particle flow objects if $d_{ij} > k_{t,i}^{-2}$. If $d_{ij} > k_{t,i}^{-2}$ then the particle flow object is discarded. This process continues iteratively until there are no more objects to consider. Objects with $\Delta > R$ are still considered, making the R input parameter an energy cut-off for clustering and not a direct radius value. Figure 5.5 shows the anti- k_t algorithm's performance compared to other jet finding algorithms. The anti- k_t algorithm results in a more conical shape than other jet finding algorithms; better encapsulating the shower profile of jets.

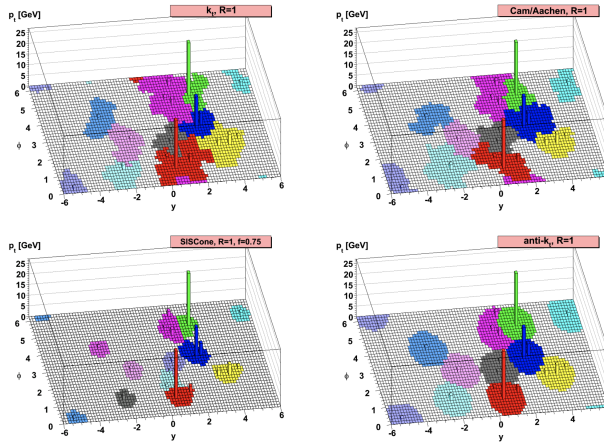


Figure 5.5: Comparison between several jet finding algorithms [49].

After jets are reconstructed, they must be calibrated at the jet energy scale. This process is detailed in Ref [51]. A flow chart showing the process of calibrating a jet is shown in Figure 5.6.

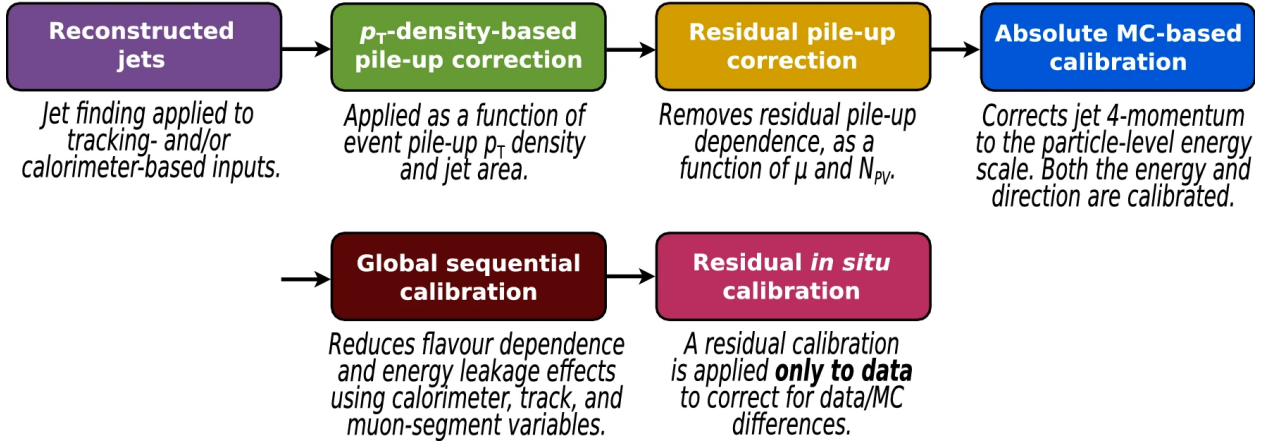


Figure 5.6: Stages of jet energy scale calibrations. Each one is applied to the four-momentum of the jet. [51]

5.5.1 b -jet Tagging

Jets originating from hard scatter b quarks are an important signature in high energy physics colliders, especially so in the analysis discussed in this dissertation. An initial state b quark hadronizes into B-hadrons which have a relatively long lifetime. Due to the relativistic speeds and long lifetime of the B-hadrons they travel a distance away from the IP before decaying and creating a hadronic shower. This leads to a secondary vertex that can be measured. A pictorial representation is shown in Figure 5.7. The impact parameter d_0 shown is the minimum distance between the tracks from the secondary vertex and IP.

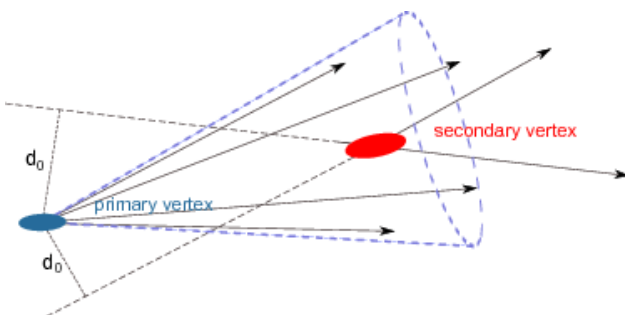


Figure 5.7: Schematic view of the tracks in a b -jet [52].

There are several methods used to tag a jet as coming from a b quark; this analysis uses the DL1 high level tagger [53] that is based on an artificial deep neural network. Neural networks are discussed in detail in Section 6.4. DL1 not only tags b -jets, but also outputs the probability for a jet to be initiated from a charm or light flavor quark. The DL1 tagger has over 20 input variables, including the p_T and η of jets [54]. For a b -jet tagging efficiency of 10% the DL1 tagger will mistag a charm/light-flavor jet at a rate of 0.02% [53]. The analysis discussed in this dissertation uses a fixed cut working point that corresponds to an average efficiency of 70% for b -jets in $t\bar{t}$ events.

5.6 τ Identification

One of the most important particles in the final state of the search discussed in this dissertation is the τ lepton. The decay channels of τ leptons make them difficult to reconstruct. A τ lepton can decay to hadrons, an electron, or a muon; in each decay mode, at least one neutrino is also present. Due to the great difficulty in discerning lepton τ decays from true leptons, the analysis discussed in this dissertation only considers τ leptons that have decayed hadronically. The hadronic decay mode consists charged hadrons (π^\pm), a neutrino, and possible neutral hadrons (π^0). A τ lepton decaying in this manner within the ATLAS detector leaves tracks in the ID and collimated showers of energy in the calorimeters; the neutrino does not interact with the ATLAS detector, therefore no direct signature is left behind. Reconstruction is done on the visible part of the hadronically decaying τ lepton, further referred to as $\tau_{had-vis}$ in the rest of this dissertation.

The $\tau_{had-vis}$ candidates start with an anti- k_t jet seed with $E_T > 10$ GeV in the calorimeter; tracks and topoclusters within $\Delta R = 0.2$ are added to the $\tau_{had-vis}$ candidate. The axis of the original jet seed is redefined in the direction of the $\tau_{had-vis}$ candidate and calibration is

done at the $\tau_{had-vis}$ scale [55]. An overlap removal is done to ensure the $\tau_{had-vis}$ candidate is isolated from electrons and muons. Tracks are required to have $E_T > 30$ GeV, $|\eta| < 2.3$ and strictly either 1 or 3 tracks. A $\tau_{had-vis}$ candidate is referred to as 1-prong or 3-prong based on the associated number of tracks. To discern $\tau_{had-vis}$ objects from quark-initiated and gluon-initiated jets a Recurrent Neural Network (RNN) is used [56]. The search described in this analysis uses a medium WP that corresponds to 75% identification efficiency for 1-prong and 60% for 3-prong in $\gamma \rightarrow \tau\tau$ collision events with a rejection factor of $\sim 35 - 240$ for jets [56].

5.7 E_T^{miss}

The final SM particle in the reconstruction scheme is the neutrino². The presence of a neutrino, or another minimally interacting particle, can be inferred through the calculation of E_T^{miss} ³; which takes advantage of the initial collision having a small momentum in the transverse plane ($p_T \simeq 0$). The initial momentum in the z direction (along the beamline) cannot be known due to the composite nature of the colliding protons and the associated PDFs of their components.

The calculation of E_T^{miss} in the ATLAS detector is defined as

$$E_T^{\text{miss}} = - \sum E_T = \sum p_T^\mu + \sum p_T^e + \sum p_T^\gamma + \sum p_T^\tau + \sum p_T^{\text{jets}} + \sum p_T^{\text{soft}} \quad (5.4)$$

²The W, Z and gluon do not have long enough lifetimes to leave signatures within the ATLAS detector volume. Instead, their presence is inferred through their decay products

³The choice of E_T^{miss} to represent missing transverse momentum is a common nomenclature. Other choices include p_T^{miss} , MET, and et miss.

where the p_T^{soft} term comes from soft tracks that are not associated with any physics objects [57]. The analysis discussed in this dissertation uses E_T^{miss} triggers in one of the subchannels to select events and is described in Chapter 6.

CHAPTER 6

SEARCH FOR CHARGED HIGGS BOSONS

This chapter details a search for a charged Higgs boson decaying to a hadronically decaying tau lepton and a neutrino; the phenomenology is discussed in Section 2.3. The search contains two subchannels, $\tau + \text{jets}$ and $\tau + \ell$ based on the decay of the associated top quark in the collision event. The $\tau + \text{jets}$ subchannel ($t \rightarrow Wb$, $W \rightarrow q\bar{q}$) has a higher branching fraction, leading to higher sensitivity at larger m_{H^\pm} values. The $\tau + \ell$ subchannel ($t \rightarrow Wb$, $W \rightarrow \ell\nu$) has a much lower branching fraction, but takes advantage of single-lepton triggers which enhance background suppression of QCD jet $\rightarrow \tau$ fakes. This leads to an increased sensitivity at lower m_{H^\pm} values. The extra neutrino in the $\tau + \ell$ decay mode creates extra difficulties in separating signal from background in this subchannel by adding a significant contribution to the E_T^{miss} calculation for the event.

The search described by this dissertation uses a profile likelihood ratio as the test statistic in a simultaneous fit in two Control Regions (CRs) and three SRs. The discriminating variable is chosen to be the output score distribution of a Multivariate Analysis Technique (MVA). In the previous publication described in Section 2.3.1 several BDT were used, binned in m_{H^\pm} ; this analysis uses a PNN to classify events as signal-like or background-like.

This chapter discusses in detail the entire analysis, including the signal signatures, event selections, analyzed datasets, modeling of backgrounds, training and evaluation of classifiers, studies of systematic uncertainties, and results.

6.1 Signature and Event Selection

As shown in Figure 2.4, the production of the H^\pm is dependent on its mass m_{H^\pm} . Table 6.1 shows the production mechanisms for m_{H^\pm} values in bins of the top quark mass m_t as well as the main decay mode (and theoretical constraints), and the main source of background. Three mass ranges are defined, low mass $80 \leq m_{H^\pm} \leq 130$ GeV, intermediate mass $140 \leq m_{H^\pm} \leq 190$, and high mass $200 \leq m_{H^\pm} \leq 3000$ GeV. The two subchannels have similar signal signatures with a hard-scatter source of E_T^{miss} , one $\tau_{\text{had-vis}}$, and at least 1 b -jet from the associated top decay. In the $\tau + \ell$ subchannel there is an extra requirement of a lepton (e or μ). Due to the variable amount of energy available to the final state products based on m_{H^\pm} the event topology changes as a function of m_{H^\pm} . As described in Section 6.4, classifiers are trained and evaluated in m_{H^\pm} bins to account for the varying event topology.

H^\pm Mass	Production Mechanism	Decay	Main Background
$m_{H^\pm} < m_t$	double-resonant $t \rightarrow H^\pm b$ (LO) 	$H^\pm \rightarrow \tau^\pm \nu_\tau$ (low $\tan \beta \implies H^\pm \rightarrow cs$ or $H^\pm \rightarrow cb$)	
$m_{H^\pm} \simeq m_t$	non-resonant $t \rightarrow H^\pm b$ (LO) interferences taken into account	$H^\pm \rightarrow \tau \nu$	
$m_{H^\pm} > m_t$	single-resonant $gg \rightarrow tbH^\pm$ (NLO) 	$H^\pm \rightarrow tb$ ($\cos(\beta - \alpha) \simeq 0$ and large $\tan(\beta) \implies H^\pm \rightarrow \tau \nu$ $BR(H^\pm \rightarrow \tau^\pm \nu_\tau) \simeq 10 - 15\%$)	multi-jet

Table 6.1: H^\pm production mechanisms based on m_{H^\pm} , dominant H^\pm decay mode, and the main background associated with the diagram.

6.1.1 Object Definitions

After physics objects are reconstructed additional kinematic and identification cuts are applied to allow for high identification efficiency while keeping significant statistics [56, 51, 53, 47, 46]. Table 6.2 shows the identification requirements on all objects used in the analysis. In both subchannels $\tau_{had-vis}$ candidates are required to fit the medium working point described in Section 5.6 that corresponds to a 75% efficiency for 1-prong and 60% efficiency for 3-prong $\tau_{had-vis}$ identification, an $|\eta|$ cut of < 2.3 that also excludes the gap and crack region of the ATLAS calorimeters at $1.37 < |\eta| < 1.52$, and an overlap removal with electrons. For the $\tau+jets$ subchannel, the $\tau_{had-vis} p_T$ is required to be greater than 40 GeV and greater than 30 GeV for the $\tau + \ell$ subchannel. Although muons and electrons are not part of the $\tau+jets$ signal final state, a loose identification and isolation requirement is used to veto events; while the $\tau + \ell$ subchannel requires there to be either an electron or a muon that passes the tight identification and isolation requirements as well as a p_T above 30 GeV. The jets in candidate events are required to have greater than 25 GeV in p_T and are made with the anti- k_t algorithm with $R=0.4$. The p_T cut of 24 GeV ensures that no jet is consistent with having originated from instrumental effects or non-collision backgrounds. Jets tagged as b -jets are done so at a 70% efficient working point using the DL1r tagger described in Section 5.5.1.

6.1.2 Event Selections

Each subchannel signal region has stricter requirements than the object definitions described in Section 6.1.1. Table 6.3 details these selections. The channels differ in the triggers used; the $\tau+jets$ subchannel relies on E_T^{miss} triggers while the $\tau + \ell$ subchannel relies

Object	$\tau + \text{jets}$	$\tau + \ell$
$\tau_{\text{had-vis}}$	Leading reconstructed τ (regardless of its ID), mediumID*, $p_T > 40$ GeV, $ \eta ^{***} < 2.3$, e OLR	Leading reconstructed τ (regardless of its ID), mediumID*, $p_T > 30$ GeV, $ \eta ^{***} < 2.3$, e OLR
e	LoseLLH, $p_T > 20$ GeV, $ \eta ^{***} < 2.47$, Loose isolation, IP cuts	TightLLH, $p_T > 30$ GeV, $ \eta ^{***} < 2.47$, Tight isolation, IP cuts
μ	LooseID, $p_T > 20$ GeV, $ \eta < 2.5$, Loose isolation, IP cuts	TightID, $p_T > 30$ GeV, $ \eta < 2.5$, Tight isolation, IP cuts
jet	AntiKt4EMPFlow, $p_T > 25$, GeV $ \eta < 2.5$, JVT** > 0.59, Btag=70%, DL1r	AntiKt4EMPFlow, $p_T > 25$ GeV, $ \eta < 2.5$, JVT** > 0.59, Btag=70%, DL1r

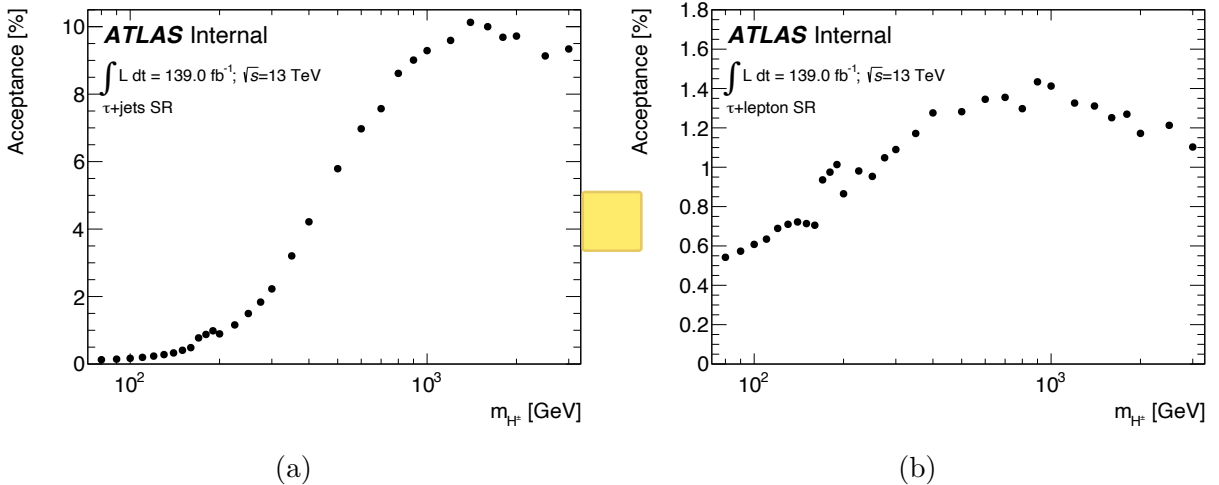
Table 6.2: Definitions of physics objects used in this analysis.

on single lepton triggers. Due to the difficulty of separating signal from background and the large amount of background, the $\tau + \text{jets}$ subchannel has a higher p_T cut on the $\tau_{\text{had-vis}}$ of 40 GeV as opposed to the $\tau + \ell$ value of 30 GeV. In addition, a higher value of E_T^{miss} of 150 GeV is required for the $\tau + \text{jets}$ subchannel compared to 50 GeV in the $\tau + \ell$ subchannel. In the $\tau + \text{jets}$ subchannel a value of 50 GeV is also required of the transverse mass m_T defined as

$$m_T = \sqrt{2p_T^\tau E_T^{\text{miss}}(1 - \cos\Delta\phi_{\tau, E_T^{\text{miss}}})} \quad (6.1)$$

The $\tau + \ell$ has no such requirement, but does require the $\tau_{\text{had-vis}}$ and lepton to have opposite electromagnetic charge. A set of orthogonal CRs are defined for each subchannel to verify proper background modelling and are described in Section 6.3. The acceptance of signal in the signal regions defined in Table 6.3 is shown in Figure 6.1. Due to the larger branching fraction of $t \rightarrow W + b; W \rightarrow q\bar{q}$ as opposed to $t \rightarrow W + b; W \rightarrow \ell + \nu$ the $\tau + \text{jets}$ subchannel has a factor of 10 larger signal acceptance than the $\tau + \ell$ subchannel. In both channels, the signal acceptance decreases for m_{H^\pm} values > 1000 GeV. This is an artifact of objects becoming boosted, meaning their decay products are extremely collimated, resulting in lower efficiencies for object identification.

$\tau + jets \text{ SR}$	$\tau + \ell \text{ SR}$
E_T^{miss} Trigger	Single lepton triggers (e or μ)
$1 \tau_{\text{had-vis}}; p_T^\tau > 40 \text{ GeV}$	$1 \tau_{\text{had-vis}}; p_T^\tau > 30 \text{ GeV}$
$0 \ell \text{ (e or } \mu) ; p_T^\ell > 20 \text{ GeV}$	$1 \ell \text{ (e or } \mu) ; p_T^\ell > 30 \text{ GeV}$
$\geq 3 \text{ jets} ; p_T^j > 25 \text{ GeV}$	$\geq 1 \text{ jet} ; p_T^j > 25 \text{ GeV}$
$\geq 1 b\text{-jets}; p_T^{b\text{-jet}} > 25 \text{ GeV}$	$\geq 1 b\text{-jets}; p_T^{b\text{-jet}} > 25 \text{ GeV}$
$E_T^{\text{miss}} > 150 \text{ GeV}$	$E_T^{\text{miss}} > 50 \text{ GeV}$
$m_T(\tau, E_T^{\text{miss}}) > 50 \text{ GeV}$	Opposite sign τ and ℓ

Table 6.3: $\tau + jets$ and $\tau + \ell$ signal region definitions.Figure 6.1: Signal acceptance as a function of the charged Higgs boson mass for both the $\tau + jets$ (a) and $\tau + \ell$ subchannels (b). Statistical errors are shown but are negligible.

6.2 Datasets

This analysis uses the full Run-2 ATLAS dataset collected between 2015 and 2018 corresponding to $139.0 \pm 2.4 \text{ fb}^{-1}$ [58]. The datasets used are required to be included in the ATLAS ‘‘Good Run Lists’’ (GRLs), meaning they have passed nominal data quality checks with all detector subsystems operating within normal conditions. Further event cleaning is

applied that removes events in which a reconstructed jet originated from detector noise or non-collision backgrounds. The collection of data throughout Run-2 can be seen in Figure 3.4.

6.2.1 Signal Modeling

MC simulations of H^\pm signal events are generated at varying orders dependent on m_{H^\pm} . In all cases, the 2HDM Type II model described in Section 2.2.2 is assumed and the generator MadGraph is used. The lower mass range corresponding to $m_{H^\pm} < 140$ GeV where a H^\pm takes the place of a W^\pm in a top decay is generated at LO. The intermediate mass range of $140 \leq m_{H^\pm} < 200$ GeV is generated at LO, taking into account the non-resonant, single-top resonant and double-resonant diagrams and their interferences. In this mass range, the final state contains one H^\pm , one W^\pm , and two b quark. For charged Higgs masses of 200 GeV and above, the H^\pm is produced in association with a top quark and is generated at NLO. The Powheg-box v2 [38, 39] generator is used with the NNPDF3.0 NLO PDF [59] set in the matrix element calculations to generate $t\bar{t}$ and single top-quarks in the W t- and s-channels. In all cases, the parton generator is interfaced with Pythia v8.230 [37] with the NNPDF2.3 LO PDF [60] using the A14 underlying event tuning parameters [61]. Table 6.4 shows the cross section and raw number of events generated for each m_{H^\pm} point for both subchannels.

6.3 Background Modeling

The main sources of backgrounds are shown in Table 6.5, separated between backgrounds with a prompt $\tau_{had-vis}$ in the hard scatter process and those that arise from the misidentification of other physics objects as a $\tau_{had-vis}$. The cross section of all simulated background

m_{H^\pm} [GeV]	σ [pb]	$\tau + \ell$ Generated Events	$\tau + \text{jets}$ Generated Events
80	61.639	220k	110k
90	52.823	220k	110k
100	43.777	220k	110k
110	34.770	220k	110k
120	26.092	220k	110k
130	18.069	220k	110k
140	15.023	220k	220k
150	7.681	220k	220k
160	2.665	220k	220k
170	0.63748	220k	220k
180	0.52979	220k	220k
190	0.47201	220k	220k
200	0.55632	110k	220k
225	0.44081	110k	220k
250	0.3573	110k	220k
275	0.28592	110k	220k
300	0.23373	110k	220k
350	0.15774	110k	220k
400	0.10818	110k	220k
500	0.054139	110k	220k
600	0.02847	110k	220k
700	0.015764	110k	220k
800	0.009067	110k	220k
900	0.005324	110k	220k
1000	0.003271	110k	220k
1200	0.001311	110k	220k
1400	0.000558	110k	220k
1600	0.000252	110k	220k
1800	0.000120	110k	220k
2000	0.0000587	110k	220k
2500	0.0000111	110k	220k
3000	0.00000234	110k	220k

Table 6.4: For each H^\pm mass the generator cross-section ($\sigma \times BR(H^\pm \rightarrow \tau^\pm \nu_\tau)$) is given, as well as the number of generated events for both $\tau + \ell$ and $\tau + \text{jets}$ subchannels.

samples and the relevant generators can be seen in Table 6.6. Control regions that are designed to be orthogonal to the signal region are created for both subchannels in order to study the modeling of the backgrounds. These control regions are defined by the cuts in Table 6.7 ($\tau + \text{jets}$) and Table 6.8 ($\tau + \ell$). For the $\tau + \ell$ subchannel the Same Sign and b-veto control regions are further split into two control regions, one that requires a μ in the event and another that requires an electron.

Backgrounds w/ prompt $\tau_{had-vis}$	Backgrounds w/ fake τ
$t\bar{t}$ estimated with MC	Fake $j \rightarrow \tau$ estimated with data driven fake factor method
$W(Z) + \text{jets}$ estimated with MC	Fake $\ell \rightarrow \tau$ estimated with MC, validated on $Z \rightarrow ee$
Diboson estimated with MC	

Table 6.5: Dominant backgrounds from prompt $\tau_{had-vis}$ and fake $\tau_{had-vis}$ candidates.

Background process	Generator & parton shower	Cross section number(s) [pb]
$t\bar{t}$ with at least one lepton ℓ	Powheg & Pythia8	729.77*
Single top-quark <i>t</i> -channel		59.17*
Single top-quark <i>s</i> -channel	Powheg & Pythia8	3.29*
Single top-quark <i>Wt</i> -channel		83.83
$W(\ell\nu) + \text{jets}$	Sherpa 2.2.1	2.0×10^4 2.0×10^4 2.0×10^4
$Z/\gamma^*(\ell\ell, \nu\nu) + \text{jets}$	Sherpa 2.2.1	2.1×10^3 2.1×10^3 2.1×10^3
WW		54.81
WZ	Powheg & Pythia8	16.34
ZZ		8.94

Table 6.6: Cross sections for the main SM background samples at $\sqrt{s} = 13$ TeV. Here, ℓ refers to the three lepton families e , μ and τ . All background cross sections are normalized to NNLO predictions, except for diboson events, where the NLO prediction is used. A '*' indicates that the quoted cross section for the sample is neglecting leptonic/hadronic branching ratios.

As seen in Table 6.5 misidentified objects appearing as $\tau_{had-vis}$ candidates comprise a significant portion of the total background. Fakes arising from $\ell \rightarrow \tau$ misidentification

	$t\bar{t}$ CR	W+Jets CR	b-veto CR	b-veto $m_T > 100$ CR
Number of $\tau_{had-vis}$	1	1	0	0
p_T^τ	> 40 GeV	> 40 GeV	> 40 GeV	> 40 GeV
Number of jets	≥ 3	≥ 3	≥ 3	≥ 3
p_T^{jet}	≥ 25 GeV	≥ 25 GeV	≥ 25 GeV	≥ 25 GeV
Number of b -jets	≥ 2	0	0	0
Number of ℓ	0	0	0	0
E_T^{miss}	> 150 GeV	> 150 GeV	> 150 GeV	> 150 GeV
$m_T(\tau, E_T^{\text{miss}})$	< 100 GeV	< 100 GeV	> 50 GeV	> 100 GeV
Type of modeling	$t\bar{t}$	W+Jets	Close to SR	Fake $j \rightarrow \tau$ enriched

Table 6.7: Control region definitions for the $\tau+\text{jets}$ subchannel.

	Dilepton-btag CR	Zee CR	b-veto CR	Same Sign CR
Number of $\tau_{had-vis}$	0	1	0	0
p_T^τ	> 30 GeV	> 30 GeV	> 30 GeV	> 30 GeV
Number of jets	≥ 1	≥ 1	≥ 1	≥ 1
p_T^{jet}	≥ 25 GeV	≥ 25 GeV	≥ 25 GeV	≥ 25 GeV
Number of b -jets	≥ 1	0	0	≥ 1
Number of ℓ	2 (1 e , 1 μ)	1 e	1 tight e (μ)	1 tight e (μ)
E_T^{miss}	> 50 GeV	> 50 GeV	> 50 GeV	> 50 GeV
mass(τ, e)	N/A	$> 40; < 140$ GeV	N/A	N/A
Type of modeling	$t\bar{t}$ and single-top	Fake $\ell \rightarrow \tau$ enriched	Close to SR	Fake $j \rightarrow \tau$ enriched

Table 6.8: Control region definitions for the $t\bar{t} + \ell$ subchannel.

are well modeled in MC simulations and are reweighted with scale factors provided by the ATLAS τ combined performance [1]. The mass of the $\tau_{had-vis}$ electron system can be seen in Figure 6.2 as verification of fake $\ell \rightarrow \tau$ modeling. However, fakes due to $j \rightarrow \tau$ misidentification are not well modeled in MC simulations due to a poor misunderstanding of systematic uncertainties associated with the fake $\tau_{had-vis}$ object and limited statistics of simulated events. Instead, a data driven method is used to extract a scaling constant referred to as a fake factor.

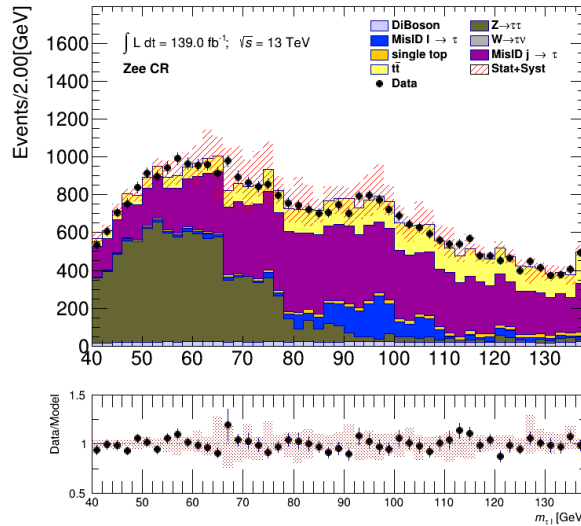


Figure 6.2: Mass of τ - e system in the Zee control region. All systematics except for $t\bar{t}$ theory uncertainties are included.

In the $\tau + \ell$ final state a significant portion of $j \rightarrow \tau$ fakes come from misidentifying $\tau_{had-vis}$ candidates in W+jets events that contain a true ℓ in the W decay and have a misidentified jet as a $\tau_{had-vis}$. Fakes of this manner also arise from QCD-like multi-jet interactions. The FF method used to estimate the amount of expected fake $\tau_{had-vis}$ objects that pass the $\tau_{had-vis}$ identification procedure is described in Section 5.6. This method applies weights, or fake factors, to a subset of "anti- $\tau_{had-vis}$ " objects that have failed the selection and identification criteria in the signal region. A control region is defined to be rich in anti- $\tau_{had-vis}$ objects,

where the $\tau_{had-vis}$ candidates fail the loose τ working point but have a small, non-zero τ identification RNN score. The FF and number of events with misidentified $\tau_{had-vis}$ objects (N_{fakes}^τ) are defined as:

$$\begin{aligned} FF &= \frac{N^{\tau-id}}{N^{anti-\tau-id}} \\ N_{fakes}^\tau &= N_{fakes}^{anti-\tau} \times FF \end{aligned} \quad (6.2)$$

Both of these values are then corrected for $\tau_{had-vis}$ candidates matching a true hadronic τ at generator level:

$$\begin{aligned} N^{\tau-id} &= N^{\tau-id}(Data) - N^{\tau-id}(MC) \\ N_{fakes}^{anti-\tau} &= N^{anti-\tau}(Data) - N_{true}^{anti-\tau}(MC) \end{aligned} \quad (6.3)$$

Two CRs are created, one to capture the multi-jet (MJ) fakes and the other to study the W+jets fakes. The  J CR uses the $\tau + \text{jets}$ signal region definition with an additional b-veto and an $E_T^{\text{miss}} < 80$ GeV cut. The W+jets CR¹ uses the $\tau + \ell$ signal region definition with a b-veto, no E_T^{miss} cut, and a cut on the transverse mass of the $\ell-E_T^{\text{miss}}$ system of $60 < m_T(\ell, E_T^{\text{miss}}) < 160$ GeV. The FF in the signal region is defined as

$$FF_{sig} = \alpha_{MJ} \times FF_{MJ} + (1 - \alpha_{MJ}) \times FF_{W+jets} \quad (6.4)$$

where α is taken from a template fit of the τ -ID score distributions of the anti- τ s using template shapes from the anti- τ distributions in the MJ and W+jets control regions. In the signal regions, the number of events containing fake- $\tau_{had-vis}$ candidates is defined as

$$N_{fake-\tau} = FF_{sig} \times N_{anti-\tau} \quad (6.5)$$

¹This W+jets CR is not the one defined in Table 6.7. This is a new region used to extract the fake factors.

Figure 6.3 shows FF plotted in each control region for 1-prong and 3-prong $\tau_{had-vis}$ binned in $p_T\tau$; extracted α values and their fits can be seen in Appendix B.

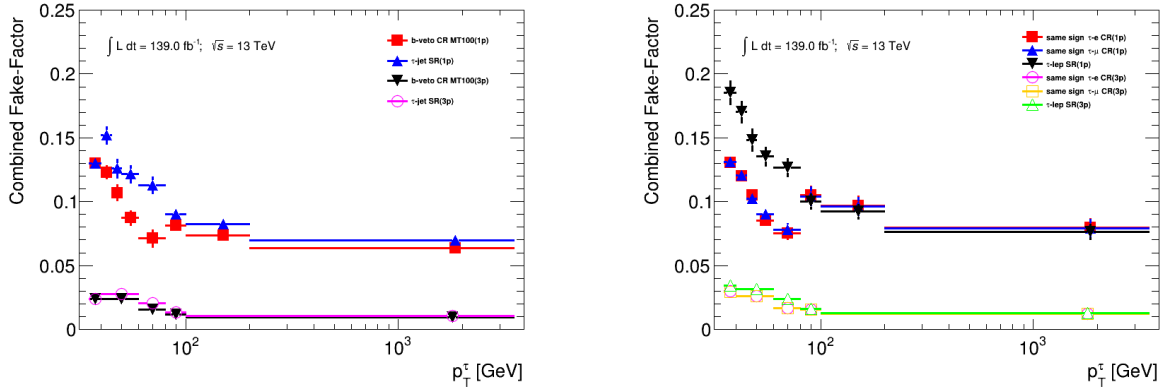


Figure 6.3: Combined FF for the τ +jets b-veto $m_T > 100$ control region, τ +jets signal region, τ +electron(muon) with same-sign control region and the $\tau + \ell$ signal region. Error bars represent systematic uncertainties of the method.

To verify background modeling, the E_T^{miss} distributions in each of the control regions are plotted with final scale factors including fake factors in Figure C.7 (τ +jets) and Figure C.25 ($\tau + \ell$). These plots include a ratio of reconstructed data events and simulated MC events bin by bin to ensure proper modeling a variable shapes. More background modeling plots can be seen in Appendix C. Tables 6.9 6.10 and 6.11 show the expected event yields and the effect of each selection cut on the background sources as well as selected m_{H^\pm} values of 110, 170, and 1000 GeV. At the time of writing, the analysis is still blinded so Data yields are not known.

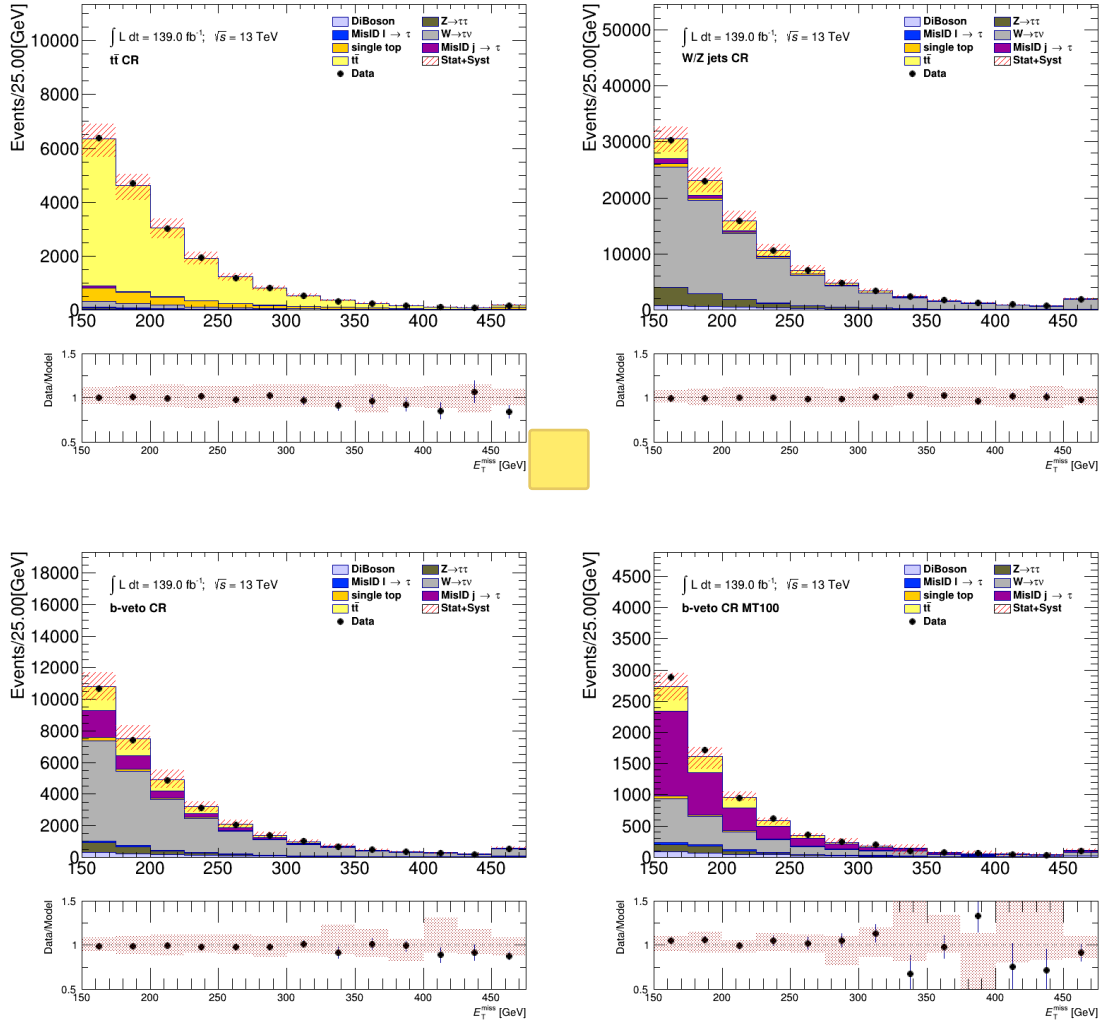


Figure 6.4: Comparison between the predicted and the measured E_T^{miss} distributions in various control regions defined for the $\tau + \text{jets}$ channel. The uncertainty band includes both statistical and systematic uncertainties on the background prediction.

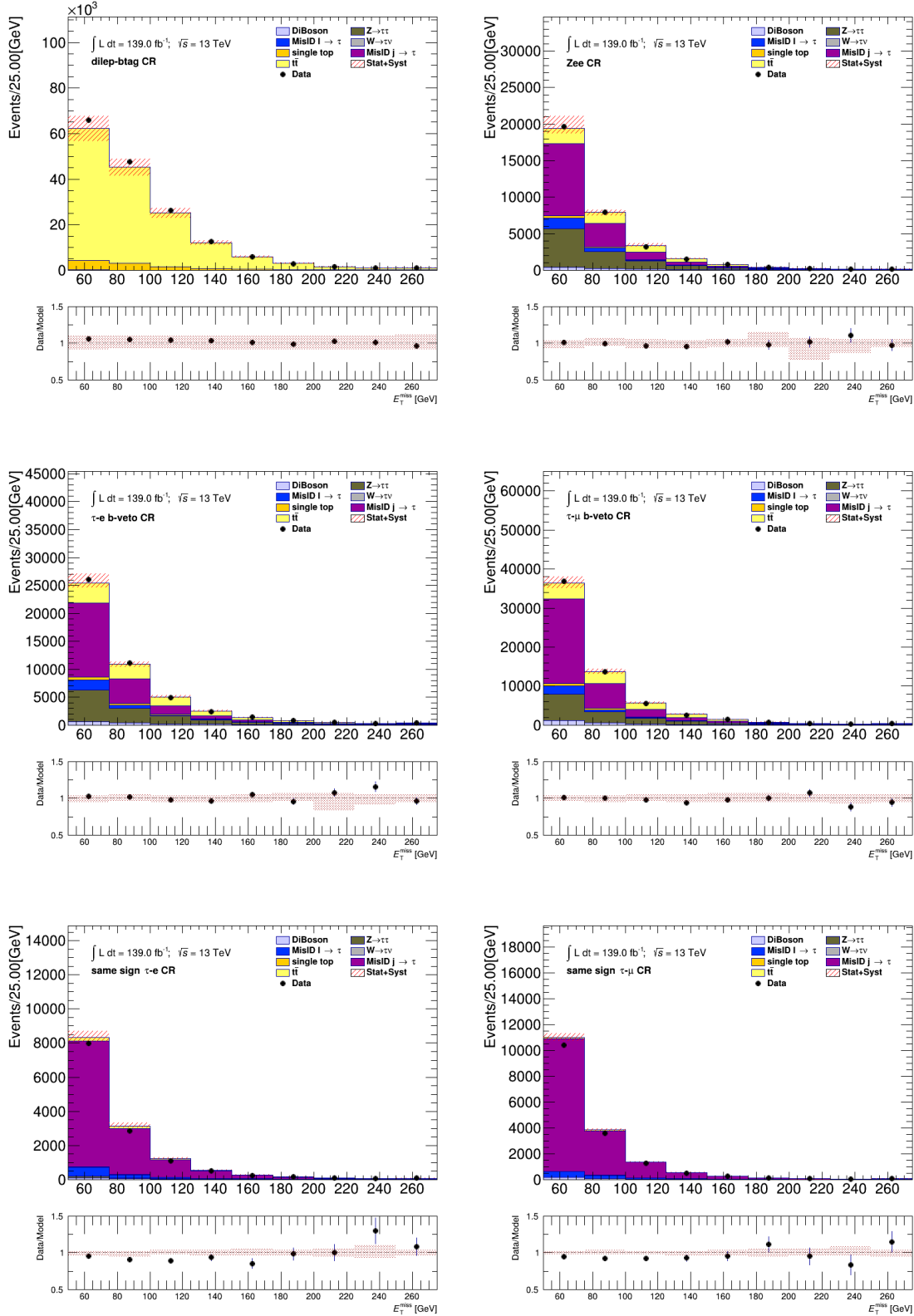


Figure 6.5: Comparison between the predicted and the measured E_T^{miss} distributions in various control regions defined for the $\tau + \ell$ channel. The uncertainty band includes both statistical and systematic uncertainties on the background prediction.

Selection	$t\bar{t}$	Single-top-quark	$W \rightarrow \tau\nu$	$Z \rightarrow \tau\tau$
Trigger and skim	342315.32 \pm 205.10	38154.55 \pm 66.40	296087.10 \pm 539.63	52976.26 \pm 148.89
Loose tau, $p_T^{\tau} > 40$ GeV	231610.69 \pm 169.16 (68%)	26454.25 \pm 55.97 (69%)	197122.72 \pm 436.12 (67%)	37617.08 \pm 119.38 (71%)
Medium tau	133237.32 \pm 127.99 (58%)	16879.04 \pm 44.91 (64%)	142441.76 \pm 319.72 (72%)	27017.86 \pm 101.54 (72%)
Lepton veto	114888.70 \pm 118.99 (86%)	15450.09 \pm 42.79 (92%)	142390.47 \pm 319.70 (100%)	23911.34 \pm 97.78 (89%)
≥ 1 b-jet	93242.48 \pm 106.97 (81%)	11711.18 \pm 37.03 (76%)	11788.34 \pm 62.30 (8%)	2923.99 \pm 23.68 (12%)
$E_T^{\text{miss}} > 150$ GeV	48457.24 \pm 78.37 (52%)	7129.31 \pm 29.82 (61%)	7160.34 \pm 43.20 (61%)	1194.29 \pm 11.05 (41%)
$m_T > 50$ GeV (SR)	18369.33 \pm 48.16 (38%)	2276.08 \pm 16.69 (32%)	1972.76 \pm 23.54 (28%)	241.05 \pm 5.47 (20%)
Selection	Diboson (WW, WZ, ZZ)	Misidentified $e, \mu \rightarrow \tau_{\text{had-vis}}$	Misidentified jet $\rightarrow \tau_{\text{had-vis}}$	All backgrounds
Trigger and skim	13094.19 \pm 53.23	708734.11 \pm 890.75	3195982.69 \pm 560.82	4647344.22 \pm 1212.70
Loose tau, $p_T^{\tau} > 40$ GeV	9387.33 \pm 45.05 (72%)	375566.87 \pm 328.44 (53%)	1645126.81 \pm 354.50 (51%)	2522885.75 \pm 686.86 (54%)
Medium tau	6591.35 \pm 37.96 (70%)	2924.49 \pm 84.42 (1%)	198869.55 \pm 137.33 (12%)	527961.36 \pm 397.94 (21%)
Lepton veto	5976.46 \pm 37.70 (91%)	2247.49 \pm 83.45 (77%)	191880.62 \pm 134.54 (96%)	496745.16 \pm 392.74 (94%)
≥ 1 b-jet	625.84 \pm 10.33 (10%)	1194.29 \pm 40.93 (53%)	38868.36 \pm 61.73 (20%)	160354.47 \pm 151.16 (32%)
$E_T^{\text{miss}} > 150$ GeV	414.89 \pm 8.66 (66%)	428.96 \pm 7.80 (36%)	3009.41 \pm 21.14 (8%)	67794.44 \pm 97.99 (42%)
$m_T > 50$ GeV (SR)	133.30 \pm 4.67 (32%)	327.51 \pm 6.82 (76%)	2490.58 \pm 17.35 (83%)	25810.61 \pm 59.60 (38%)
Selection	H^{\pm} (110 GeV)	H^{\pm} (170 GeV)	H^{\pm} (1000 GeV)	Data (139 fb $^{-1}$)
Trigger and skim	1951.47 \pm 11.05	4992.07 \pm 19.02	34812.84 \pm 94.47	XXX \pm XXX
Loose tau, $p_T^{\tau} > 40$ GeV	1554.18 \pm 9.87 (80%)	4047.73 \pm 17.14 (81%)	27900.09 \pm 84.24 (80%)	XXX \pm XXX
Medium tau	1016.12 \pm 7.99 (65%)	2890.75 \pm 14.52 (71%)	19994.71 \pm 72.07 (72%)	XXX \pm XXX
Lepton veto	901.33 \pm 7.53 (89%)	2694.19 \pm 14.02 (93%)	18343.94 \pm 68.93 (92%)	XXX \pm XXX
≥ 1 b-jet	729.40 \pm 6.76 (81%)	2075.45 \pm 12.29 (77%)	13611.31 \pm 60.35 (74%)	XXX \pm XXX
$E_T^{\text{miss}} > 150$ GeV	425.52 \pm 5.25 (58%)	1333.74 \pm 10.03 (64%)	12797.45 \pm 58.63 (94%)	XXX \pm XXX
$m_T > 50$ GeV (SR)	264.68 \pm 4.13 (62%)	1044.07 \pm 8.86 (78%)	12728.36 \pm 58.47 (99%)	XXX \pm XXX

Table 6.9: Expected event yields and efficiencies after cumulative selection cuts and comparison with 139 fb $^{-1}$ of data for $\tau+\text{jets}$ sub-channel. The values shown for the signal correspond to $\sigma(pp \rightarrow [b]tH^{\pm}) \times Br(H^{\pm} \rightarrow \tau^{\pm}\nu_{\tau}) = 1$ pb. Statistical uncertainties are shown.

Selection	$t\bar{t}$	Single-top-quark	$W \rightarrow \tau\nu$	$Z \rightarrow \tau\tau$
Trigger and skim	410886.20 \pm 232.60	40098.96 \pm 68.91	1504.99 \pm 67.50	214323.27 \pm 1518.06
Loose tau, $p_T^{\tau} > 30$ GeV	355267.50 \pm 216.28 (86%)	34634.86 \pm 64.10 (86%)	1280.89 \pm 61.15 (85%)	184446.15 \pm 1411.31 (86%)
Medium tau	179348.02 \pm 154.01 (50%)	17098.32 \pm 46.93 (49%)	426.20 \pm 44.28 (33%)	128420.09 \pm 1199.81 (70%)
Tight electron, $p_T^e > 30$ GeV	80461.17 \pm 104.31 (45%)	6920.81 \pm 30.31 (40%)	112.68 \pm 16.71 (26%)	39581.52 \pm 621.39 (31%)
Electron and tau with OS	79604.45 \pm 103.76 (99%)	6837.95 \pm 30.14 (99%)	83.19 \pm 15.00 (74%)	39164.25 \pm 618.78 (99%)
$E_T^{\text{miss}} > 50$ GeV	53813.81 \pm 85.27 (68%)	4547.93 \pm 24.61 (67%)	38.97 \pm 6.28 (47%)	12448.80 \pm 218.27 (32%)
≥ 1 b-jet (SR)	43814.66 \pm 76.84 (81%)	3260.70 \pm 20.81 (72%)	2.41 \pm 0.56 (6%)	913.61 \pm 20.42 (7%)
Selection	Diboson (WW, WZ, ZZ)	Misidentified $e, \mu \rightarrow \tau_{\text{had-vis}}$	Misidentified jet $\rightarrow \tau_{\text{had-vis}}$	All backgrounds
Trigger and skim	18533.34 \pm 23.85	3537419.24 \pm 4942.14	2403411.34 \pm 714.76	6626177.34 \pm 5225.34
Loose tau, $p_T^{\tau} > 30$ GeV	16060.23 \pm 22.20 (87%)	1939418.21 \pm 2933.87 (55%)	2027356.60 \pm 588.57 (84%)	4558464.44 \pm 3316.76 (69%)
Medium tau	10957.22 \pm 17.56 (68%)	56819.79 \pm 851.44 (3%)	443714.51 \pm 304.58 (22%)	836784.15 \pm 1511.77 (18%)
Tight electron, $p_T^e > 30$ GeV	3619.35 \pm 10.40 (33%)	20011.76 \pm 495.63 (35%)	152485.84 \pm 182.97 (34%)	303193.13 \pm 823.07 (36%)
Electron and tau with OS	3122.54 \pm 9.91 (86%)	17202.16 \pm 452.06 (86%)	95723.92 \pm 147.37 (63%)	241738.46 \pm 788.01 (80%)
$E_T^{\text{miss}} > 50$ GeV	1903.40 \pm 7.70 (61%)	3616.05 \pm 157.27 (21%)	31529.78 \pm 79.00 (33%)	107898.73 \pm 294.27 (45%)
≥ 1 b-jet (SR)	73.21 \pm 1.53 (4%)	1096.64 \pm 24.36 (30%)	8773.81 \pm 37.64 (28%)	57935.04 \pm 93.63 (54%)
Selection	H^{\pm} (110 GeV)	H^{\pm} (170 GeV)	H^{\pm} (1000 GeV)	Data (139 fb $^{-1}$)
Trigger and skim	3202.25 \pm 13.97	4116.46 \pm 17.10	5268.21 \pm 30.05	XXX \pm XXX
Loose tau, $p_T^{\tau} > 30$ GeV	2793.23 \pm 13.05 (87%)	3600.92 \pm 15.99 (87%)	4313.45 \pm 27.22 (82%)	XXX \pm XXX
Medium tau	1915.08 \pm 10.81 (69%)	2592.01 \pm 13.58 (72%)	3132.37 \pm 23.23 (73%)	XXX \pm XXX
Tight electron, $p_T^e > 30$ GeV	852.54 \pm 7.40 (45%)	1107.30 \pm 9.12 (43%)	1356.64 \pm 15.63 (43%)	XXX \pm XXX
Electron and tau with OS	845.17 \pm 7.37 (99%)	1094.53 \pm 9.06 (99%)	1330.08 \pm 15.48 (98%)	XXX \pm XXX
$E_T^{\text{miss}} > 50$ GeV	547.00 \pm 5.94 (65%)	837.08 \pm 7.93 (76%)	1302.14 \pm 15.29 (98%)	XXX \pm XXX
≥ 1 b-jet (SR)	440.11 \pm 5.33 (80%)	613.35 \pm 6.78 (73%)	956.26 \pm 13.50 (73%)	XXX \pm XXX

Table 6.10: Expected event yields and efficiencies after cumulative selection cuts and comparison with 139 fb $^{-1}$ of data for $\tau+e$ channel. The values shown for the signal correspond to $\sigma(pp \rightarrow [b]tH^{\pm}) \times Br(H^{\pm} \rightarrow \tau^{\pm}\nu_{\tau}) = 1$ pb. Statistical uncertainties are shown.

Selection	$t\bar{t}$	Single-top-quark	$W \rightarrow \tau\nu$	$Z \rightarrow \tau\tau$
Trigger and skim	410886.20 \pm 232.60	40098.96 \pm 68.91	1504.99 \pm 67.50	214323.26 \pm 1518.06
Loose tau, $p_T^\tau > 30$ GeV	355267.50 \pm 216.28 (86%)	34634.86 \pm 64.10 (86%)	1280.89 \pm 61.15 (85%)	184446.15 \pm 1411.31 (86%)
Medium tau	179348.02 \pm 154.01 (50%)	17098.32 \pm 46.93 (49%)	426.20 \pm 44.28 (33%)	128420.09 \pm 1199.81 (70%)
Tight muon, $p_T^e > 30$ GeV	83293.59 \pm 103.84 (46%)	8704.78 \pm 33.09 (51%)	44.56 \pm 12.50 (10%)	57089.24 \pm 811.41 (44%)
Muon and tau with OS	82852.63 \pm 103.57 (99%)	8653.92 \pm 33.01 (99%)	42.72 \pm 12.17 (96%)	56860.99 \pm 810.34 (100%)
$E_T^{\text{miss}} > 50$ GeV	55250.05 \pm 84.70 (67%)	5516.70 \pm 26.38 (64%)	7.66 \pm 2.72 (18%)	13803.33 \pm 220.41 (24%)
≥ 1 b-jet (SR)	44490.69 \pm 75.96 (81%)	3874.57 \pm 22.06 (70%)	0.07 \pm 0.12 (1%)	845.89 \pm 22.07 (6%)
Selection	Diboson (WW, WZ, ZZ)	Misidentified $e, \mu \rightarrow \tau_{\text{had-vis}}$	Misidentified jet $\rightarrow \tau_{\text{had-vis}}$	All backgrounds
Trigger and skim	18533.34 \pm 23.85	3537419.44 \pm 4942.14	2403411.34 \pm 714.76	6626177.54 \pm 5225.34
Loose tau, $p_T^\tau > 30$ GeV	16060.23 \pm 22.20 (87%)	1939418.20 \pm 2933.87 (55%)	2027356.60 \pm 588.57 (84%)	4558464.43 \pm 3316.76 (69%)
Medium tau	10957.22 \pm 17.56 (68%)	56819.79 \pm 851.44 (3%)	443714.51 \pm 304.58 (22%)	836784.15 \pm 1511.77 (18%)
Tight muon, $p_T^e > 30$ GeV	5709.54 \pm 12.47 (52%)	30268.99 \pm 623.62 (53%)	199706.03 \pm 205.19 (45%)	384816.73 \pm 1049.56 (46%)
Muon and tau with OS	4960.17 \pm 11.89 (87%)	27996.60 \pm 611.93 (92%)	131414.33 \pm 171.52 (66%)	312781.35 \pm 1035.68 (81%)
$E_T^{\text{miss}} > 50$ GeV	2799.13 \pm 8.89 (56%)	3766.50 \pm 161.20 (13%)	42513.90 \pm 90.25 (32%)	123657.27 \pm 301.10 (40%)
≥ 1 b-jet (SR)	81.32 \pm 1.53 (3%)	1074.28 \pm 15.90 (29%)	8558.21 \pm 37.23 (20%)	58925.03 \pm 91.57 (48%)
Selection	H^\pm (110 GeV)	H^\pm (170 GeV)	H^\pm (1000 GeV)	Data (139 fb $^{-1}$)
Trigger and skim	3202.25 \pm 13.97	4116.46 \pm 17.10	5268.21 \pm 30.05	XXX \pm XXX
Loose tau, $p_T^\tau > 30$ GeV	2793.23 \pm 13.05 (87%)	3600.92 \pm 15.99 (87%)	4313.45 \pm 27.22 (82%)	XXX \pm XXX
Medium tau	1915.08 \pm 10.81 (69%)	2592.01 \pm 13.58 (72%)	3132.37 \pm 23.23 (73%)	XXX \pm XXX
Tight muon, $p_T^e > 30$ GeV	889.27 \pm 7.17 (46%)	1264.26 \pm 9.25 (49%)	1499.58 \pm 15.93 (48%)	XXX \pm XXX
Muon and tau with OS	884.48 \pm 7.15 (99%)	1258.52 \pm 9.22 (100%)	1485.25 \pm 15.88 (99%)	XXX \pm XXX
$E_T^{\text{miss}} > 50$ GeV	563.90 \pm 5.71 (64%)	946.69 \pm 8.01 (75%)	1447.52 \pm 15.62 (97%)	XXX \pm XXX
≥ 1 b-jet (SR)	447.73 \pm 5.07 (79%)	693.80 \pm 6.85 (73%)	1004.35 \pm 12.95 (69%)	XXX \pm XXX

Table 6.11: Expected event yields and efficiencies after cumulative selection cuts and comparison with 139 fb $^{-1}$ of data for $\tau + \mu$ channel. The values shown for the signal correspond to $\sigma(pp \rightarrow [b]tH^\pm) \times Br(H^\pm \rightarrow \tau^\pm \nu_\tau) = 1$ pb. Statistical uncertainties are shown.

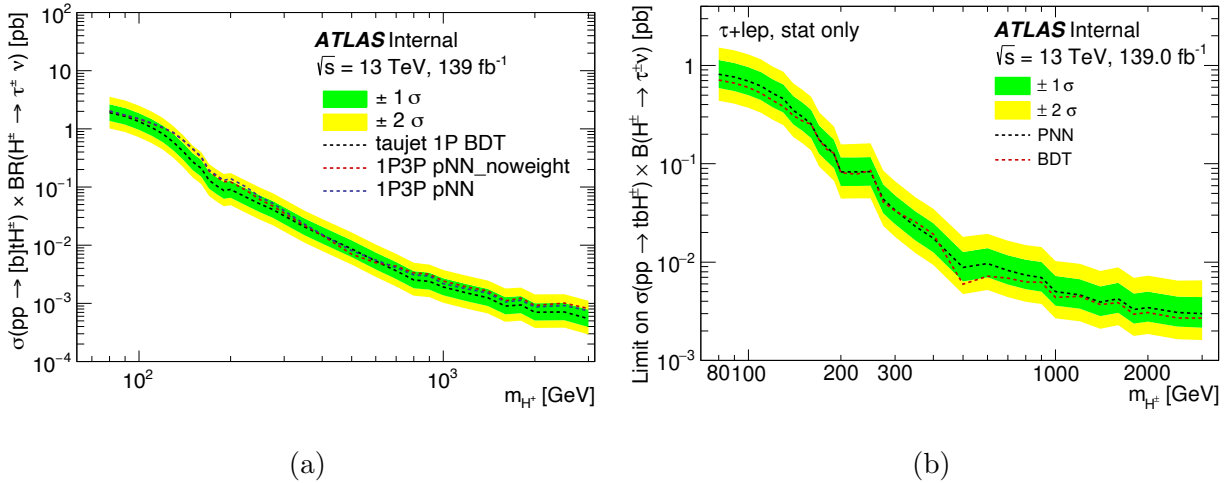


Figure 6.6: Comparison of performance of an optimized BDT and an unoptimized PNN on expected limits on $\sigma(pp \rightarrow tbH^\pm) \times \mathcal{B}(H^\pm \rightarrow \tau\nu)$ in the $\tau + \text{jets}$ (a) and $\tau + \ell$ (b) signal regions.

6.4 Multivariate Analysis Techniques

Once variables distributions are properly scaled and data/MC agreement is verified, multivariate analysis techniques are employed to separate signal-like events from background-like events in the signal regions. In the previous publication (described in Section 2.3.1), BDTs binned in m_{H^\pm} were used as the classifier, this publication use one PNN for the entire m_{H^\pm} spectrum. BDTs excel at separating linear correlations, whereas neural networks take advantage of nonlinear correlations. In the case of a PNN the parameterized variable, here m_{H^\pm} , is taken as an input to the network in addition with other input variables. PNNs offer the advantage of having one classifier model that can evaluate at any m_{H^\pm} value by learning how the signal event topology changes as m_{H^\pm} varies [62]. For illustrative purposes, expected limits on $\sigma(pp \rightarrow tbH^\pm) \times \mathcal{B}(H^\pm \rightarrow \tau\nu)$ in both subchannels is shown comparing an optimized BDT and an unoptimized PNN in Figure 6.6. It is seen that the PNN performs similarly to the BDTs used in the previous analysis. A PNN was chosen as the discriminator.

A Neural Network (NN) is a computing system loosely inspired by the human brain. NNs combine adaptive nonlinear basis functions in an attempt to perform a task; classification in the context of this dissertation. A NN contains layers of nodes connected to each other with an associated weight and threshold. As long as a node has output greater than the given threshold value, data will flow through that node². Otherwise, that node is not activated and data are not sent to the next layer. The NN as a whole relies on a process called training where the node weights are varied, an accuracy is calculated based on a given loss function, the weights are then varied again and the process repeats. This is done until a preferred accuracy is reached; the final node weights are saved and new data can be evaluated. A diagram of a PNN can be seen in Figure 6.7, where the parameterized input is labeled as θ . The learned function of a NN can be written as:

$$y(x) = w_0^2 + \sum_{m=1}^M [w_m^2 \cdot h(w_{0m}^1 + \sum_{k=1}^D w_{km}^1 x_k)] \quad (6.6)$$

where w is the neuron weights, M is the number of basis functions being combined, D is the number of inputs and h is the activation function.

This analysis uses four PNNs, events with 1-prong τ and 3-prong τ are divided into separate datasets within both subchannels.

6.4.1 Training

The training of the PNNs used in this dissertation are done with the Keras [63] library using the TensorFlow [64] library as backend. In order to increase the significance of training statistics and protect from overtraining, the k -fold method is used. Overtraining occurs

²This is true of basic NNs. In some cases, this dissertation included, nodes are allowed small non-zero weights (negative or positive) to retain a so called “leaky” node.

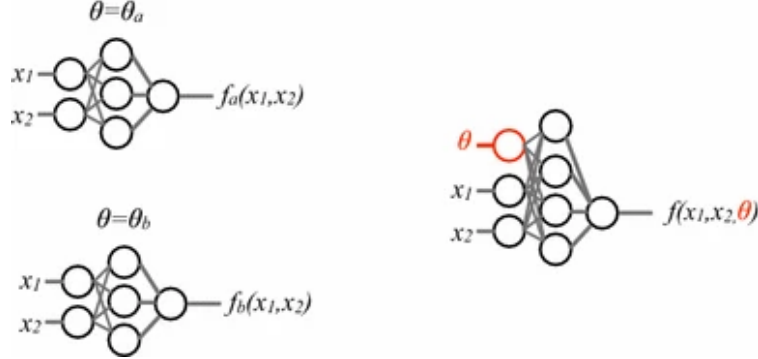


Figure 6.7: *Left*, individual networks with input variables (x_1, x_2), each trained with examples with a single value of some parameter $\theta = \theta_a, \theta_b$. The individual networks are purely functions of the input variables. Performance for intermediate values of θ is not optimal nor does it necessarily vary smoothly between the networks. *Right*, a single network trained with input variables (x_1, x_2) as well as input parameter θ ; such a network is trained with examples at several values of the parameter θ [62].

	Fold 1	Fold 2	Fold 3	Fold 4	Fold 5	Background
Partition 1	Evaluation	Train	Train	Train	Train	Fold 1
Partition 2	Train	Evaluation	Train	Train	Train	Fold 2
Partition 3	Train	Train	Evaluation	Train	Train	Fold 3
Partition 4	Train	Train	Train	Evaluation	Train	Fold 4
Partition 5	Train	Train	Train	Train	Evaluation	Fold 5

Figure 6.8: The k -fold method for $k = 5$ [66].

when a NN has been fine tuned to have a high accuracy with a specific dataset and does not generalize to other datasets. To protect against this, dropout is used [65]. The k -fold method divides input training samples into k equal-sized subsets. The k -th subset is trained on the other $k - 1$ subsets and evaluated on the k -th subset. Figure 6.8 shows a pictorial representation of the k -fold method. The standard choice of $k = 5$ is used in this analysis.

A single PNN training is performed on all m_{H^\pm} values at once, with the m_{H^\pm} value being taken as an input variable. For signal events, the m_{H^\pm} value from the MC generator is given; background events are replicated 32 times (the number of simulated m_{H^\pm} points is 32) and each m_{H^\pm} value is given for each set. To avoid biasing the training due to varying statistics at each m_{H^\pm} value, the background events are weighted by a factor of $w = N_S^i/N_B^i$ where i

corresponds to a given m_{H^\pm} value and N_S^i and N_B^i are the number of signal and background events, respectively. When the PNN is evaluated, the m_{H^\pm} value is assumed and the output is used as the discriminant at that m_{H^\pm} .

6.4.2 Input Variables Selection

The choice of input variables to the PNNs is critical to the performance of the analysis. Several sets of variables were compared using expected limits as the figure of merit. All studies were performed in the $\tau + \ell$ signal region, as this region proves the most difficult challenge to separate signal-like events from background-like events. One such study investigated the discriminating power of two sets of input variables. Input variables set A, consisting of the four vector components of the main physical objects in each event, were compared against another set of input variables B. Tables of the two sets of input variables are shown in Table 6.12.

The variable $m_{H^\pm}^{Truth}$ corresponds to the m_{H^\pm} value the training and evaluation is performed at. In both cases, the variable Υ is used. Υ is a measure of the $\tau_{had-vis}$ polarization, computed by taking the asymmetry of energies carried by the charged and neutron pions from the 1-prong τ decay measured in the laboratory frame. Υ is defined as

$$\Upsilon = \frac{E_T^{\pi^\pm} - E_T^{\pi^0}}{E_T^\tau} \approx 2 \frac{p_T^{\tau-track}}{p_T^\tau} - 1 \quad (6.7)$$

where $p_T^{\tau-track}$ is the transverse momentum of the track associated with the 1-prong $\tau_{had-vis}$ candidate. As such, Υ is only defined for 1-prong $\tau_{had-vis}$ candidates. As demonstrated in the previous analysis, Υ provides a large contribution to signal-backgrounds separation at charged Higgs masses below 400 GeV [10]. This is due to W^- bosons coupling exclusively to left-handed τ^- leptons in $W \rightarrow \tau\nu$ decays and W^+ bosons coupling exclusively to τ^+ leptons.

In such a case, Υ is expected to have a value of -1 . Whereas in the MSSM, a charged scalar Higgs boson would lead to an Υ value of $+1$ [67].

Set A Input Variables

p_T^τ	η^τ	ϕ^τ
p_T^ℓ	η^ℓ	ϕ^ℓ
p_T^{b-jet}	η^{b-jet}	ϕ^{b-jet}
p_T^{jet}	η^{jet}	ϕ^{jet}
E_T^{miss}	$\phi^{E_T^{\text{miss}}}$	$p_T^{j_1}$
Υ	$m_{H^\pm}^{\text{Truth}}$	

(a) Set A of input variables



Set B Input Variables

E_T^{miss}
p_T^τ
p_T^{b-jet}
p_T^ℓ
$\Delta\phi_{\tau, \text{miss}}$
$\Delta\phi_{b-jet, \text{miss}}$
$\Delta\phi_{\ell, \text{miss}}$
$\Delta R_{\tau, \ell}$
$\Delta R_{b-jet, \ell}$
$\Delta R_{b-jet, \tau}$
$\Delta\phi_{\tau, \text{miss}}/\Delta\phi_{\text{jet}, \text{miss}}$
Υ
$m_{H^\pm}^{\text{Truth}}$



(b) Set B of input variables

Table 6.12: Two sets of kinematic variables used as input to the PNN in the $\tau + \ell$ subchannel. $\Delta\phi_{X, \text{miss}}$ denotes the difference in azimuthal angle between a reconstructed object X ($X = \tau, b-jet, \ell$) and the direction of the missing transverse momentum.

An estimate of the impact of two sets of input variables on the expected limits on $\sigma(pp \rightarrow tbH^\pm) \times \mathcal{B}(H^\pm \rightarrow \tau\nu)$ is shown in 6.9. Input variables set A was chosen as performance was similar at low m_{H^\pm} and greater at high m_{H^\pm} . A optimization of the number



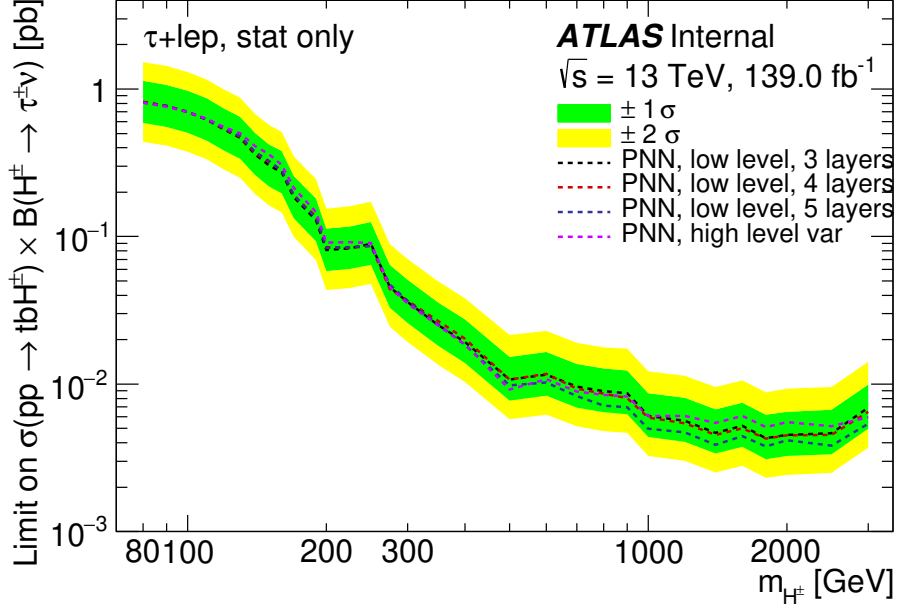


Figure 6.9: Expected limits comparing input variables set A and B with various depths in the PNN architecture. X layers refers to the number of layers in the PNN.

of layers in the PNN and several other parameters of the PNN is discussed in detail in Section 6.4.3.

6.4.3 Hyperparameter Optimization

In order to optimize the PNN, a scan of hyperparameters and network architecture was done, referred to as HPO. A calculated Area Under the Curve (AUC) was used as the figure of merit. As in the normal training scheme, the k -fold method with $k = 5$ was used to keep background modelling and classifier training statistically independent. To prevent overtraining, the early stopping method was used and the best weights kept to calculate the AUC. The early stopping method has two parameters, Δ_{min} and patience. Δ_{min} is the minimum allowed difference in AUC between training epochs. Once the Δ_{min} value is lower

than the user defined threshold several more epochs are trained to ensure a global minima is found. The number of extra training epochs is the previously mentioned patience value. For this dissertation $\Delta_{min} = 0.00001$ and a patience of 10 were used. Due to the low signal acceptance and the increased difficulty of separating signal from background at lower m_{H^\pm} values, the PNN was optimized for low m_{H^\pm} values. To optimize for PNN performance in low H^\pm mass points, a separate average taking into account only H^\pm mass values between 80 and 500 GeV was used as the final figure of merit. In an effort to keep the computational needs low, several small grids of hyperparameters and architecture structures were scanned. Tables 6.13 - 6.17 show the hyperparameter grids that were searched. Here, width refers to the number of neurons per layer and depth is the number of layers. The final hyperparameter from each grid search is highlighted in red. The results of the final grid search can be seen in Tables 6.18 and 6.19; the quoted errors were taken from the difference in k -folds. The AUC values for each m_{H^\pm} point for the final chosen model are shown in Figure 6.10.

Parameter			
activation function	softsign	relu	LeakyReLU
loss function	binary cross-entropy	mean squared error	mean absolute error
width	32		
depth	10		
batch size	1025		

Table 6.13: First grid, scanning over activation function and loss function. Binary cross-entropy was the chosen loss function, highlighted in red.

Parameter				
width	8	16	32	
depth	3	5	10	
dropout	0.1	0.3		
activation function	softsign			
loss function	binary cross-entropy			
batch size	1024			

Table 6.14: Second grid, scanning over width, depth, and dropout value. 0.1 was chosen for the dropout value, highlighted in red.

Parameter	32	64	128
width	32	64	128
depth	2	3	4
activation function	softsign	relu	LeakyReLU
dropout	0.1		
batch size	1024		
loss function	binary cross-entropy		

Table 6.15: Third grid, scanning over activation function. LeakyReLU was chosen, highlighted in red.

Parameter	32	64	128	
width	32	64	128	
depth	2	3	4	
α	0.01	0.05	0.001	0.005
batch size	1024			
dropout	0.1			
activation function	LeakyReLU			
loss function	binary cross-entropy			

Table 6.16: Fourth grid, scanning over LeakyReLU α value. $\alpha = 0.05$ was chosen, highlighted in red.

Parameter	32	64	128	256
width	32	64	128	256
depth	2	3	4	5
batch size	1024			
dropout	0.1			
activation function	LeakyReLU			
batch size	1024			
α	0.05			
loss function	binary cross-entropy			

Table 6.17: Fifth grid, scanning over network width and depth. $width = 128$ and $depth = 3$ was chosen, highlighted in red.

width	depth	80	150	250	500	Avg	LowMassAvg
128	3	0.6661 ± 0.0000	0.8145 ± 0.0000	0.9031 ± 0.0000	0.9633 ± 0.0000	0.8876 ± 0.0000	0.8261 ± 0.0968
128	5	0.6492 ± 0.0000	0.8043 ± 0.0000	0.9078 ± 0.0000	0.9628 ± 0.0000	0.8861 ± 0.0000	0.8235 ± 0.1000
128	4	0.6593 ± 0.0000	0.8117 ± 0.0000	0.9012 ± 0.0000	0.9638 ± 0.0000	0.8858 ± 0.0000	0.8232 ± 0.0994
128	2	0.6444 ± 0.0000	0.8070 ± 0.0000	0.9075 ± 0.0000	0.9631 ± 0.0000	0.8857 ± 0.0000	0.8231 ± 0.1006
64	4	0.6576 ± 0.0050	0.8080 ± 0.0013	0.9052 ± 0.0045	0.9656 ± 0.0016	0.8857 ± 0.0002	0.8230 ± 0.0994
64	2	0.6528 ± 0.0066	0.8052 ± 0.0023	0.9057 ± 0.0032	0.9651 ± 0.0007	0.8855 ± 0.0004	0.8228 ± 0.0996
64	5	0.6538 ± 0.0050	0.8044 ± 0.0019	0.9058 ± 0.0037	0.9653 ± 0.0014	0.8853 ± 0.0005	0.8224 ± 0.0997
64	3	0.6520 ± 0.0067	0.8051 ± 0.0018	0.9042 ± 0.0044	0.9649 ± 0.0019	0.8853 ± 0.0011	0.8223 ± 0.0994
256	5	0.6536 ± 0.0010	0.8044 ± 0.0033	0.9036 ± 0.0042	0.9644 ± 0.0022	0.8844 ± 0.0002	0.8213 ± 0.1003
256	4	0.6434 ± 0.0000	0.8018 ± 0.0000	0.9017 ± 0.0000	0.9619 ± 0.0000	0.8823 ± 0.0000	0.8181 ± 0.1013
32	3	0.6369 ± 0.0094	0.7950 ± 0.0041	0.8977 ± 0.0032	0.9635 ± 0.0022	0.8798 ± 0.0012	0.8139 ± 0.1031
32	4	0.6384 ± 0.0037	0.7935 ± 0.0033	0.8986 ± 0.0037	0.9636 ± 0.0016	0.8799 ± 0.0009	0.8139 ± 0.1031
32	2	0.6399 ± 0.0058	0.7924 ± 0.0024	0.8983 ± 0.0033	0.9629 ± 0.0023	0.8796 ± 0.0004	0.8135 ± 0.1023
32	5	0.6350 ± 0.0077	0.7931 ± 0.0056	0.8981 ± 0.0022	0.9625 ± 0.0005	0.8792 ± 0.0011	0.8128 ± 0.1035
256	2	0.6320 ± 0.0044	0.7971 ± 0.0000	0.8939 ± 0.0034	0.9587 ± 0.0018	0.8781 ± 0.0002	0.8120 ± 0.1023

Table 6.18: AUCs of final HPO grid. An error of 0 corresponds to only one job k-fold finishing training due to computational limits. The LowMassAvg error takes into account difference between k-folds and the associated error from the averaging calculation.

width	depth	Avg	LowMassAvg
128	3	0.8876 ± 0.0000	0.8261 ± 0.0968
128	5	0.8861 ± 0.0000	0.8235 ± 0.1000
128	4	0.8858 ± 0.0000	0.8232 ± 0.0994
128	2	0.8857 ± 0.0000	0.8231 ± 0.1006
64	4	0.8857 ± 0.0002	0.8230 ± 0.0994
64	2	0.8855 ± 0.0004	0.8228 ± 0.0996
64	5	0.8853 ± 0.0005	0.8224 ± 0.0997
64	3	0.8853 ± 0.0011	0.8223 ± 0.0994
256	5	0.8844 ± 0.0002	0.8213 ± 0.1003
256	4	0.8823 ± 0.0000	0.8181 ± 0.1013
32	3	0.8798 ± 0.0012	0.8139 ± 0.1031
32	4	0.8799 ± 0.0009	0.8139 ± 0.1031
32	2	0.8796 ± 0.0004	0.8135 ± 0.1023
32	5	0.8792 ± 0.0011	0.8128 ± 0.1035
256	2	0.8781 ± 0.0002	0.8120 ± 0.1023

Table 6.19: Average AUCs of final HPO grid. An error of 0 corresponds to only one job k-fold finishing training due to computational limits.

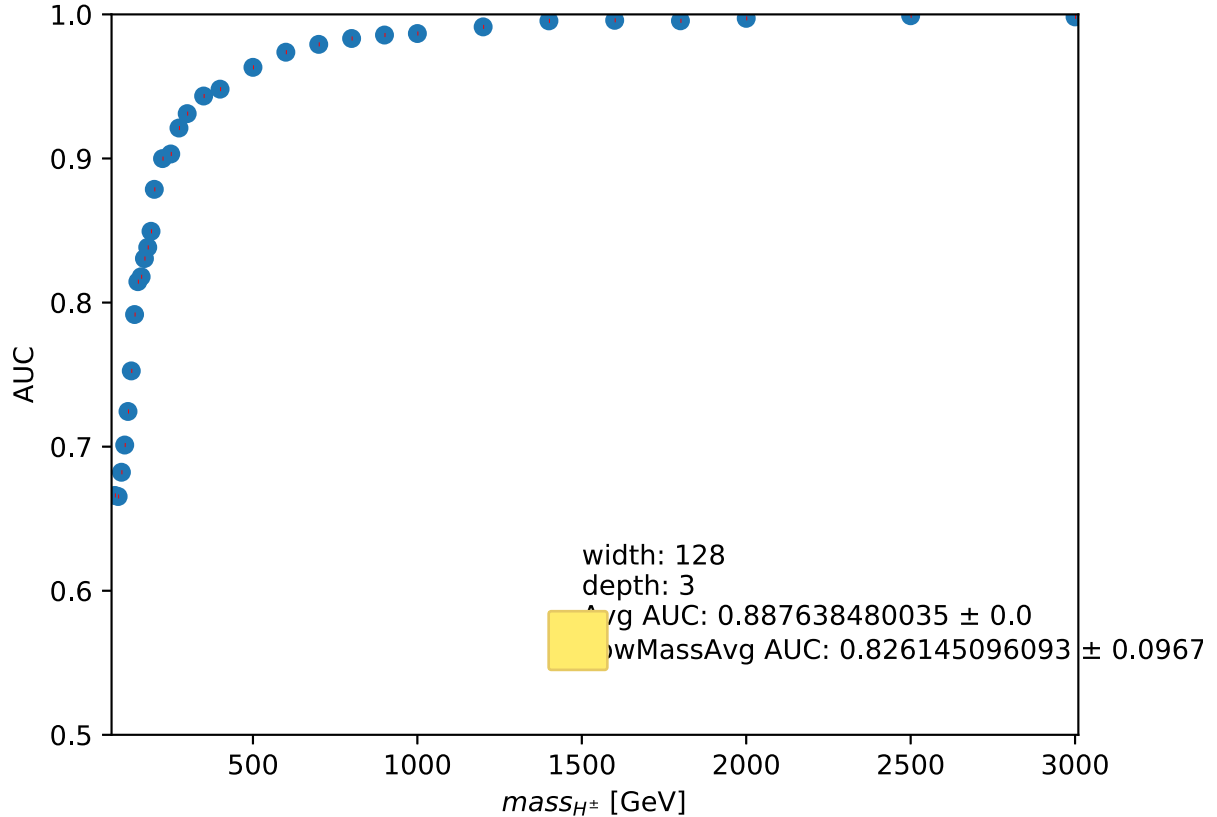


Figure 6.10: Final model AUC for each mass point. Individual points correspond to the AUC average over 5 kfolds.

The final model was chosen to have 128 neurons per layer with three layers, with the binary cross-entropy chosen as the loss function, a dropout of 0.1, LeakyReLU as the activation function with $\alpha = 0.05$. The LeakyReLU activation function is depicted in Figure 6.11, where the α value is the slope of the negative portion. Allowing negative weight values prevents neurons from becoming deactivated prematurely.

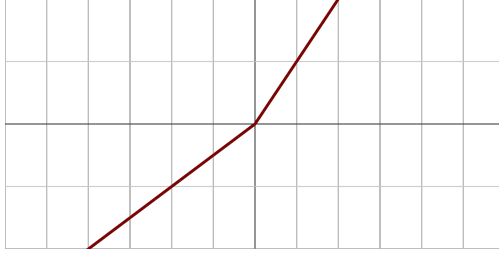


Figure 6.11: LeakyReLU activation function. The associated hyperparameter α is the slope of the negative portion of the function.

6.5 Systematic Uncertainties



Systematic uncertainties have a variety of sources and are discussed in detail here. Detector-related systematic uncertainties from the reconstruction and identification of leptons and $\tau_{had-vis}$ objects [68], simulation of the electron and muon triggers, reconstruction of E_T^{miss} , and energy/momentum scale and resolution of all physics objects [68, 51, 69, 57, 70] are studied by varying selection cuts by ± 1 standard deviation. The difference in event yields is then taken as a systematic error and summed in quadrature with all other sources of error to give the final quoted errors. Systematic errors resulting in an upward fluctuation are kept separate from downward fluctuations. The effect of the main sources of uncertainties on the event yield for $t\bar{t}$ and an arbitrary mass point of $m_{H^\pm} = 200$ GeV are shown in Table 6.20 for all SRs. Jet systematic uncertainties arising from reconstruction, identification, flavor composition, resolution account for the largest contribution. Systematic uncertainties arising from the data-driven fake factor method are shown in Table 6.21. The uncertainty listed as “Fake factors: True $\tau_{had-vis}$ in the anti- $\tau_{had-vis}$ CR” is a conservative uncertainty of 50% applied to account for amount of $\tau_{had-vis}$ candidates that are subtracted when computing $N_{fakes}^{anti-\tau}$. Table 6.22 shows systematic uncertainties combined by their source. The combined fake factor systematic uncertainty is the largest contributor, followed by the jet systematics listed above. Theoretical uncertainties for signal and $t\bar{t}$ background were considered in the

Source	Impact on the expected event yield (%)					
	$\tau + \text{jets}$		$\tau + e$		$\tau + \mu$	
	$t\bar{t}$	$H^\pm 200 \text{ GeV}$	$t\bar{t}$	$H^\pm 200 \text{ GeV}$	$t\bar{t}$	$H^\pm 200 \text{ GeV}$
$\tau_{had-vis}$ reconstruction efficiency	± 1.24	± 1.22	± 1.23	$+1.22$ -1.23	± 1.23	± 1.22
$\tau_{had-vis}$ -id	± 1.79	± 0.52	± 1.40	± 0.50	± 1.40	± 0.48
$\tau_{had-vis}$ energy scale	$+2.53$ -2.80	$+2.00$ -1.66	$+1.60$ -1.44	$+1.28$ -1.66	$+1.53$ -1.39	$+1.72$ -1.46
$\tau_{had-vis}$ energy scale (detector)	$+1.96$ -1.55	$+1.64$ -1.49	$+0.23$ -0.21	$+1.15$ -1.08	$+0.16$ -0.55	$+0.49$ -1.5
$\tau_{had-vis}$ energy scale (in-situ)	$+1.44$ -1.43	$+0.22$ -0.74	$+1.17$ -1.20	$+0.74$ -0.63	$+1.14$ -1.15	$+0.54$ -0.37
$\tau_{had-vis}$ energy scale (model)	$+0.56$ -0.61	-0.06	$+0.23$ -0.21	$+1.15$ -1.08	$+0.16$ -0.55	$+0.49$ -1.50
$\tau_{had-vis}$ energy scale (physics list)	$+1.27$ -1.26	-0.72	$+0.74$ -0.65	$+0.67$ -0.25	$+0.72$ -0.63	$+0.83$ -0.60
jet uncertainties	$+7.38$ -8.39	$+6.51$ -9.06	$+3.41$ -3.31	$+4.49$ -2.78	$+3.18$ -3.24	$+3.67$ -2.96
E_T^{miss} soft term scale/resolution	$+1.31$ -1.12	$+1.15$ -1.49	$+0.29$ -0.24	$+0.88$ -0.34	$+0.30$ -0.23	$+0.21$ -0.11
trigger	$+1.23$ -1.61	0	± 0.03	0	$+0.55$ -0.56	± 0.56
e -id	0	0	± 0.71	± 0.73	0	0
μ -id/reconstruction/isolation	0	0	0 -0.01	0 -0.11	$+0.97$ -1.40	$+1.00$ -2.94
μ MS	0	0	0	0	$+0.09$ -0.12	$+0.40$ -0.34

Table 6.20: Effect of the main systematic uncertainties on the expected event yield for $t\bar{t}$ and signal events ($m_{H^\pm} = 200 \text{ GeV}$) passing the nominal event selection of the three SRs. The three components of the $\tau_{had-vis}$ energy scale uncertainty are shown in the table. Impacts are shown in percent change with respect to the nominal SR selections.

last publication; at the time of writing this dissertation the simulations are being produced and therefore are not included.

6.6 Results

The expected event yields for backgrounds and signal³ are summarized in Table 6.23 ($\tau + \text{jets}$) and Table 6.24 ($\tau + \ell$).

³At the time of writing, the analysis is still blinded Data is not included.

Source of uncertainty	$\tau + \text{jets}$		$\tau + \ell$	
	Effect on yield	Shape	Effect on yield	Shape
Fake factors: statistical uncertainties	3.9%	✗	3.2%	✗
Fake factors: True $\tau_{\text{had-vis}}$ in the anti- $\tau_{\text{had-vis}}$ CR	+3.4% -3.2%	✗	+4% -4.3%	✗
Fake factors: tau RNN Identification SF	2.7%	✓	2.7%	✓
Fake factors: α_{MJ} uncertainty	3.6%	✗	1.9%	✗
Fake factors: Smirnov transform	0%	✓	0%	✓
Fake factors: heavy flavor jet fraction	6%	✓	5.53%	✓

Table 6.21: Effect on the shape variation and the yields of systematic uncertainties associated with the data-driven fake factor method, used to estimate the $j \rightarrow \tau$ background in the $\tau + \text{jets}$ and $\tau + \ell$ channel.

Source	Impact on the expected event yield (%)					
	$\tau + \text{jets}$		$\tau + e$		$\tau + \mu$	
	$t\bar{t}$	H^\pm 200 GeV	$t\bar{t}$	H^\pm 200 GeV	$t\bar{t}$	H^\pm 200 GeV
Fake factor uncertainties	+9.11 -9.04	+9.11 -9.04	+8.23 -8.34	+8.23 -8.34	+8.23 -8.34	+8.23 -8.34
jet uncertainties	+7.38 -8.39	+6.51 -9.06	+3.41 -3.31	+4.49 -2.78	+3.18 -3.24	+3.67 -2.96
τ uncertainties	± 4.36	+2.91 -2.80	+2.84 -2.74	+2.65 -2.70	+2.77 -2.78	+2.58 -2.97
E_T^{miss} uncertainties	+1.31 -1.12	+1.15 -1.49	+0.29 -0.24	+0.88 -0.34	+0.30 -0.23	+0.21 -0.11
trigger uncertainties	+1.23 -1.61	0	± 0.03	0	+0.55 -0.56	± 0.56
e uncertainties	0	0	± 0.71	± 0.73	0	0
μ uncertainties	0	0	-0.01	-0.11	+0.97 -1.41	+1.08 -2.96

Table 6.22: Effect of the combined main systematic uncertainties on the expected event yield for $t\bar{t}$ and signal events ($m_{H^\pm} = 200$ GeV) passing the nominal event selection of the three SRs. The three components of the $\tau_{\text{had-vis}}$ energy scale uncertainty are shown in the table. Impacts are shown in percent change with respect to the nominal SR selections.

The test statistic \tilde{q}_μ [71] is used to test the agreement of the data with the background-only and signal+background hypotheses. The test statistic is based on a profile likelihood ratio where the binned likelihood function $\mathcal{L}(\mu, \theta)$ is constructed as the product of Poisson probability terms over all bins and regions. The likelihood ratio is the ratio between the

Table 6.23: Expected event yields for the backgrounds and a hypothetical H^\pm signal after applying all $\tau+jets$ selection criteria, and comparison with 139 fb^{-1} of data. The values shown for the signal assuming a charged Higgs boson mass of 170 GeV and 1000 GeV, with a cross-section times branching fraction $\sigma(pp \rightarrow tbH^\pm) \times \mathcal{B}(H^\pm \rightarrow \tau\nu)$ corresponding to $\tan\beta = 40$ in the hMSSM benchmark scenario. Statistical and Systematic uncertainties are quoted, respectively.

Sample	Event yields $\tau_{had-vis}+jets$		
True τ_{had}			
$t\bar{t}$	18443.27	\pm	48.35
	+1545.67		
	-1697.11		
Single-top-quark	2284.34	\pm	17.39
	+184.69		
	-207.49		
$W \rightarrow \tau\nu$	1979.17	\pm	23.63
	+179.85		
	-229.80		
$Z \rightarrow \tau\tau$	242.12	\pm	5.50
	-24.27		
	-32.88		
Diboson (WW, WZ, ZZ)	133.76	\pm	4.69
	+9.47		
	-12.61		
Misidentified $e, \mu \rightarrow \tau_{had-vis}$	328.89	\pm	6.85
	+25.60		
	-34.58		
Misidentified jet $\rightarrow \tau_{had-vis}$	2506.28	\pm	17.39
	+130.53		
	-133.40		
All backgrounds	25917.83	\pm	59.82
	+1572.87		
	-1730.97		
H^\pm (170 GeV), hMSSM $\tan\beta = 40$	1075.81	\pm	9.12
	+82.89		
	-79.19		
H^\pm (1000 GeV), hMSSM $\tan\beta = 40$	12910.36	\pm	59.30
	+784.57		
	-720.17		

Table 6.24: Expected event yields for the backgrounds and a hypothetical H^\pm signal after applying all $\tau + \ell$ selection criteria, and comparison with 139 fb^{-1} of data. The values shown for the signal assuming a charged Higgs boson mass of 170 GeV and 1000 GeV, with a cross-section times branching fraction $\sigma(pp \rightarrow tbH^\pm) \times \mathcal{B}(H^\pm \rightarrow \tau\nu)$ corresponding to $\tan\beta = 40$ in the hMSSM benchmark scenario. Statistical and Systematic uncertainties are quoted, respectively.

Sample	Event yields $\tau+e$			Event yields $\tau+\mu$				
True τ_{had}								
$t\bar{t}$	43813.50	\pm	76.85	+1749.82 -1833.87	44486.48	\pm	75.33	+1811.78 -1907.08
Single-top-quark	3260.52	\pm	20.81	+124.27 -134.66	3873.35	\pm	22.06	+158.03 -165.92
$W \rightarrow \tau\nu$	2.41	\pm	0.56	+0.22 -2.15	0.07	\pm	0.12	+0.08 -0.16
$Z \rightarrow \tau\tau$	913.55	\pm	42	+64.56 -149.42	845.89	\pm	22.07	+88.71 -111.03
Diboson (WW, WZ, ZZ)	72.64	\pm	1.52	+5.25 -3.91	80.81	\pm	1.53	+5.40 -6.45
Misidentified $e, \mu \rightarrow \tau_{\text{had-vis}}$	1083.97	\pm	24.33	+41.65 -73.42	1060.30	\pm	15.84	+43.44 -70.69
Misidentified jet $\rightarrow \tau_{\text{had-vis}}$	8662.43	\pm	49	+450.65 -470.53	8426.64	\pm	37.12	+440.04 -459.88
All backgrounds	57809.03	\pm	93.57	+1812.82 -1846.46	58773.63	\pm	90.99	+1873.75 -1970.06
H^\pm (170 GeV), hMSSM $\tan\beta = 40$	598.17	\pm	6.60	+20.84 -22.52	702.21	\pm	6.93	+22.39 -16.12
H^\pm (1000 GeV), hMSSM $\tan\beta = 40$	938.90	\pm	13.25	+48.99 -37.72	1024.06	\pm	13.21	+48.42 -57.01

conditional maximum-likelihood estimator of the nuisance parameters, θ , for a given signal hypothesis μ and the unconditional maximum-likelihood estimator for μ and the nuisance parameters. \tilde{q}_μ is defined as:

$$\tilde{q}_\mu = \begin{cases} -2 \ln \frac{\mathcal{L}(\mu, \hat{\theta}(\mu))}{\mathcal{L}(0, \hat{\theta}(0))}, & \hat{\mu} < 0 \\ -2 \ln \frac{\mathcal{L}(\mu, \hat{\theta}(\mu))}{\mathcal{L}(\hat{\mu}, \hat{\theta})}, & 0 \leq \hat{\mu} \leq \mu \\ 0 & \hat{\mu} > \mu \end{cases} \quad (6.8)$$

The fit is performed on the PNN score distributions in the three signal regions, $\tau+\text{jets}$, $\tau+\text{e}$, $\tau+\mu$, and the dilepton-btag control region which is enriched in the dominant $t\bar{t}$ background. Pre-fit PNN score distributions are shown in Figures 6.12, 6.13, and 6.14. At the time of writing this dissertation, the analysis is still blinded. Assuming the fit agrees with the background-only hypothesis expected limits of $\sigma(pp \rightarrow tbH^\pm) \times \mathcal{B}(H^\pm \rightarrow \tau\nu)$ are calculated. Exclusion limits are set at the 95% confidence level (CL) using the CL_s procedure [72]. The expected exclusion limits on $\sigma(pp \rightarrow tbH^\pm) \times \mathcal{B}(H^\pm \rightarrow \tau\nu)$ can be seen in Figure 6.15 compared to the previous 36.1 fb^{-1} result. In all three subchannels an improvement across the entire m_{H^\pm} range can be seen. The $\tau+\text{e}$ and $\tau+\mu$ SRs outperform the $\tau+\text{jets}$ SR at low m_{H^\pm} while the $\tau+\text{jets}$ SR excels at high mass values. In all three SRs the limits turn upwards between 2500 GeV and 3000 GeV; this is due to the decreased signal acceptance shown in Figure 6.1. At the time of writing the combination of the $\tau + \ell$ and $\tau+\text{jets}$ subchannels is underway. As in the previous result [10] the combined limit will be extrapolated to set limits on $\tan\beta$.

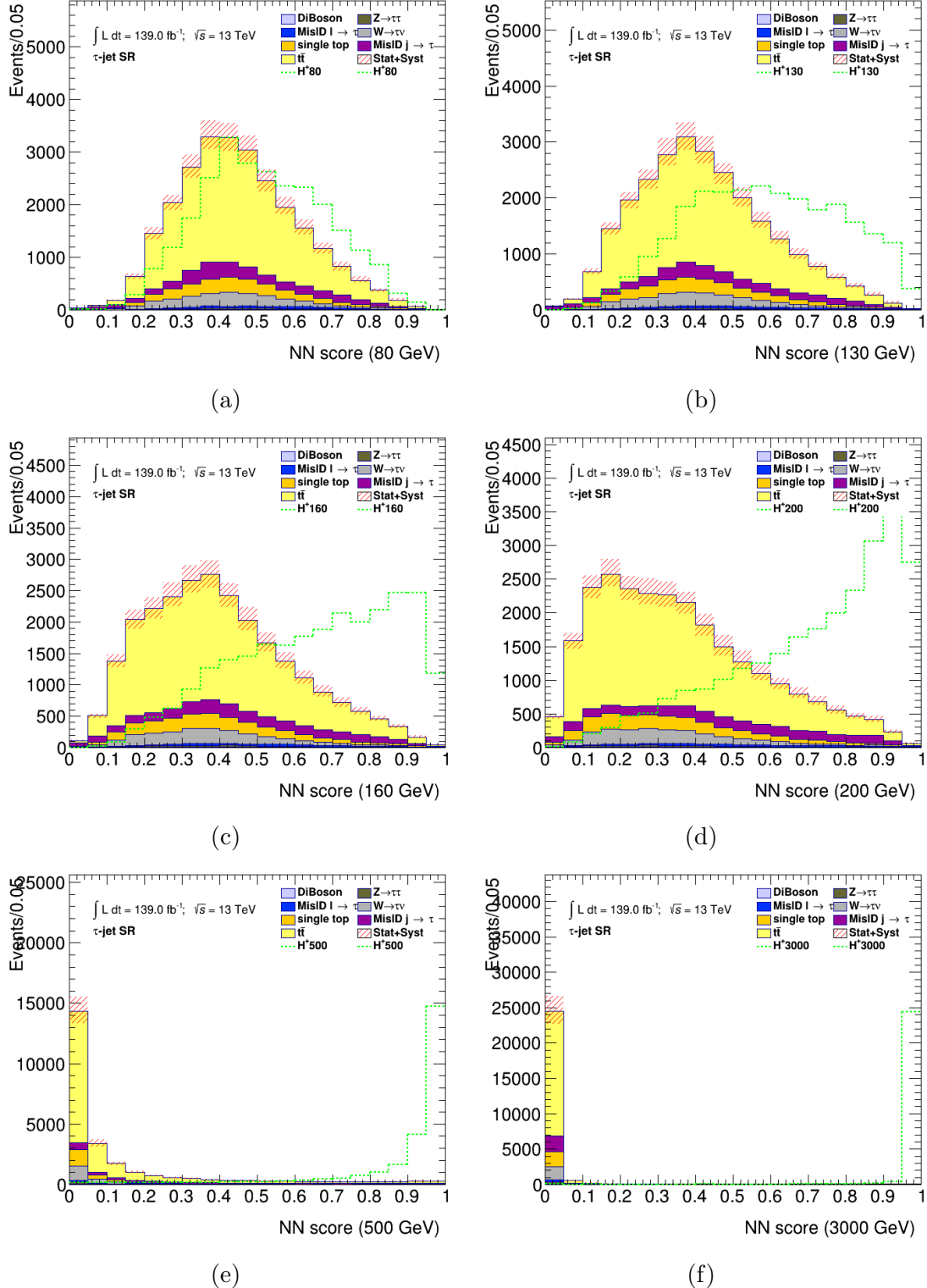


Figure 6.12: PNN score distributions in the signal region of the $\tau + \text{jets}$ channel, for the six charged Higgs boson mass parameters. The lower panel of each plot shows the ratio of data to the SM background prediction. The uncertainty bands include all statistical and systematic uncertainties. The normalization of the signal (shown for illustration) corresponds to the integral of the background.

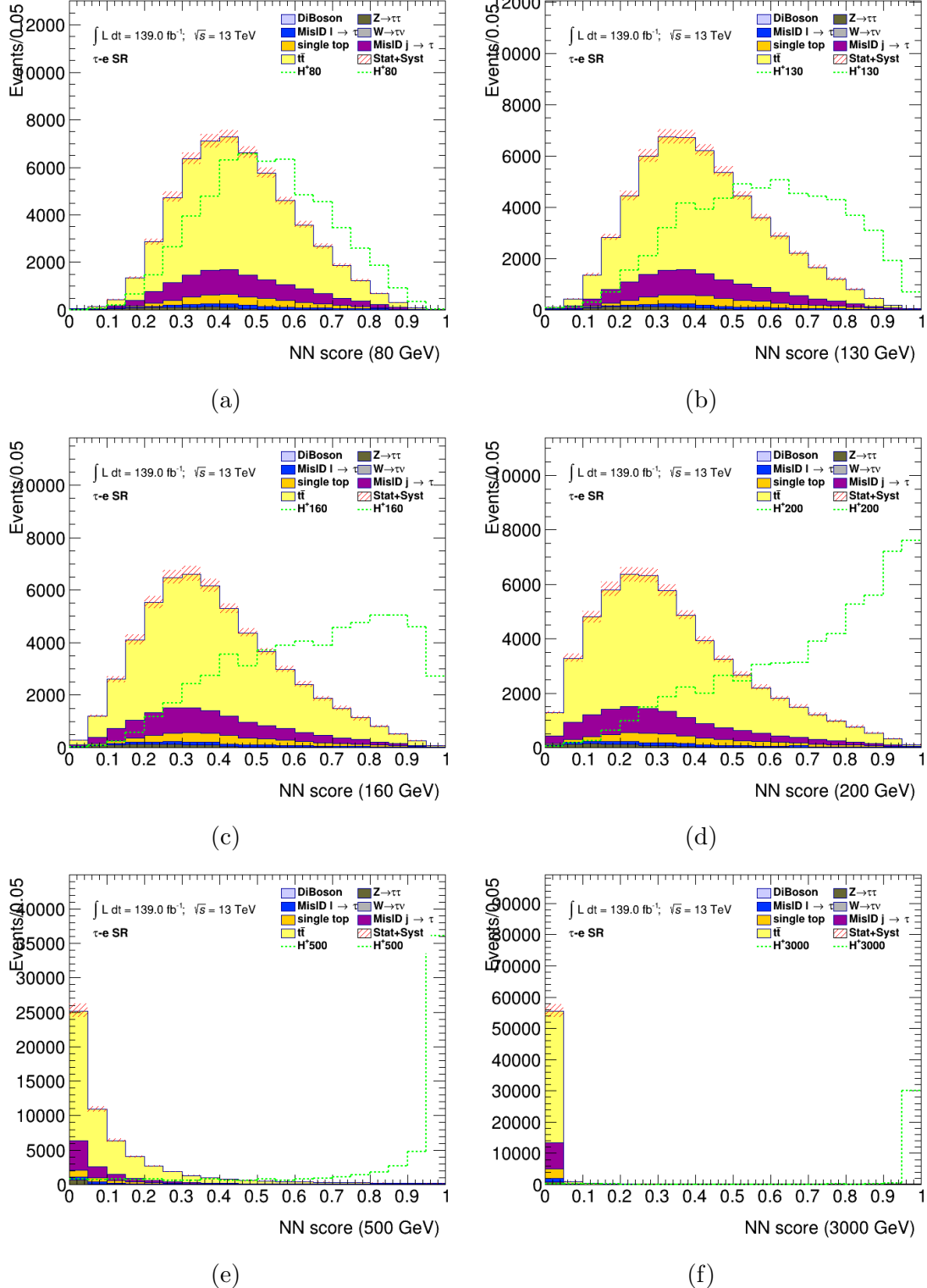


Figure 6.13: PNN score distributions in the signal region of the τ +e sub-channel, for the six charged Higgs boson mass parameters. The lower panel of each plot shows the ratio of data to the SM background prediction. The uncertainty bands include all statistical and systematic uncertainties. The normalization of the signal (shown for illustration) corresponds to the integral of the background.

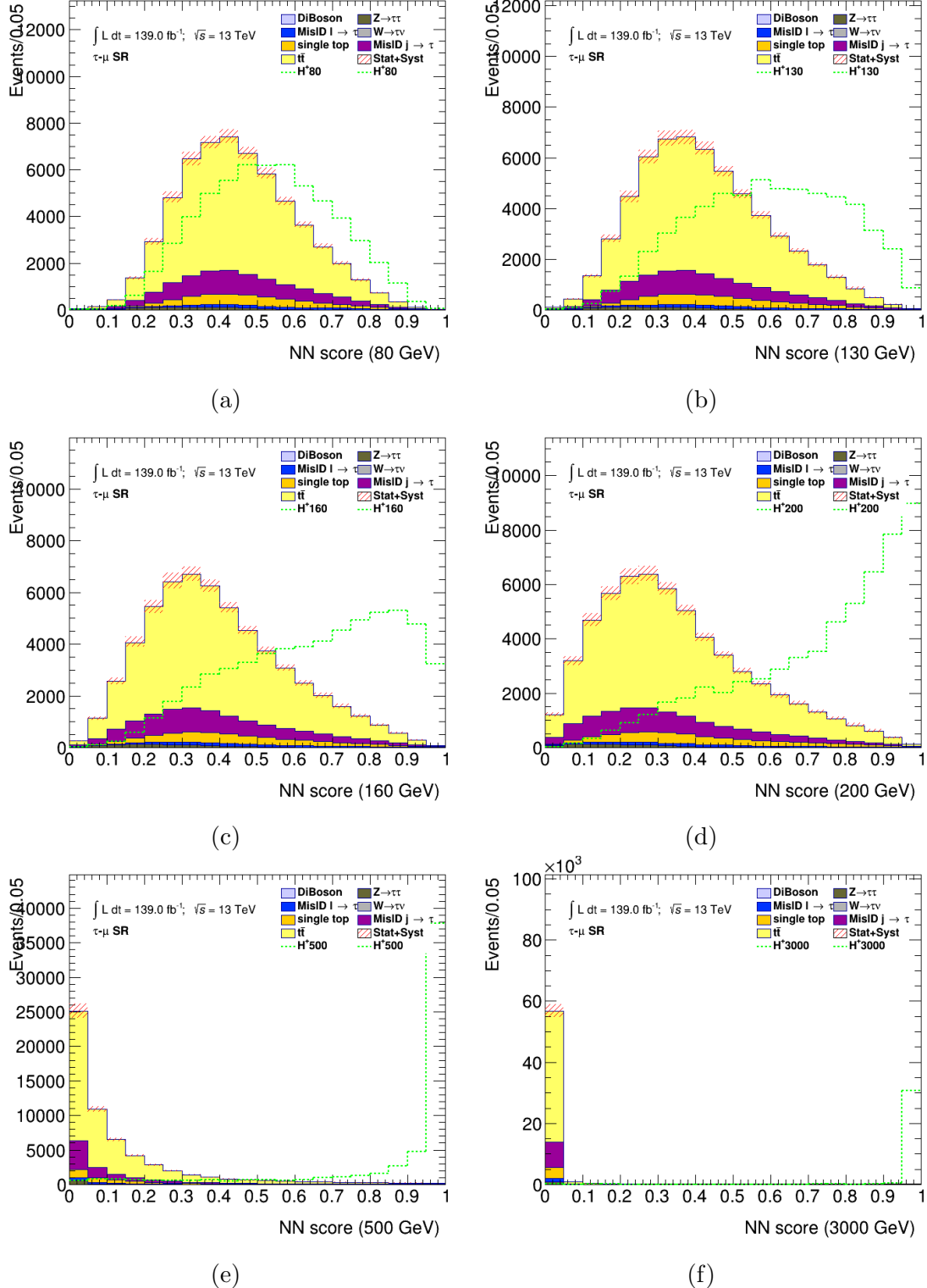


Figure 6.14: PNN score distributions in the signal region of the $\tau + \mu$ sub-channel, for the six charged Higgs boson mass parameters. The lower panel of each plot shows the ratio of data to the SM background prediction. The uncertainty bands include all statistical and systematic uncertainties. The normalization of the signal (shown for illustration) corresponds to the integral of the background.

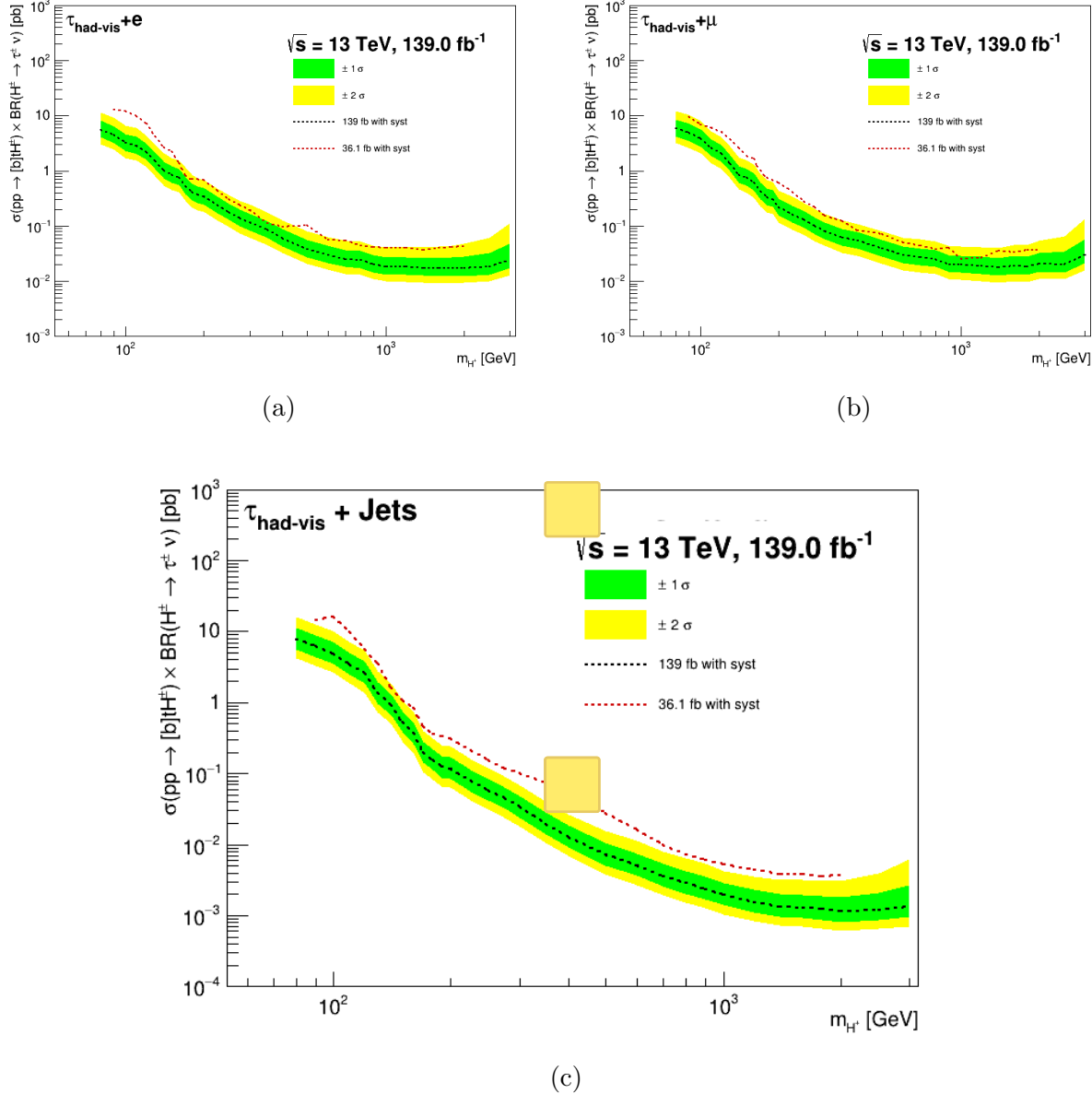


Figure 6.15: Expected 95% CL exclusion limits on $\sigma(pp \rightarrow tbH^\pm) \times \mathcal{B}(H^\pm \rightarrow \tau\nu)$ as a function of the charged Higgs boson mass in 139 fb^{-1} of pp collision data at $\sqrt{s} = 13\text{ TeV}$ in the $\tau+e$ signal region (a), the $\tau+\mu$ signal region (b), and the $\tau+\text{jets}$ signal region (c). In the case of the expected limits, one- and two-standard-deviation uncertainty bands are also shown. As a comparison, the expected exclusion limits obtained with the dataset collected in 2015 and 2016 [10] are also shown.

CHAPTER 7

CONCLUSION

The Standard Model is an incredibly accurate model of fundamental particle physics, but is ultimately incomplete. There are many possible extensions to the Standard Model; this dissertation covers a search for a charged Higgs boson in the $H^\pm \rightarrow \tau^\pm \nu_\tau$ final state within the 2-Higgs Doublet Model (2HDM) theory.

The search consists of two subchannels based on the decay of the associated top quark; $\tau + \ell$ for the leptonic decay channel and $\tau + \text{jets}$ for the hadronic decay channel. Parameterized Neural Networks were investigated and optimized to separate signal from background in the Signal Regions. Assuming a result consistent with the SM expected results are shown compared to previously observed results. At the time of writing, the final unblinding procedure within the ATLAS collaboration is underway.



Appendices

APPENDIX A

TILECAL DATA QUALITY

This appendix gives an overview of the TileCal and ATLAS Data Quality Monitoring (DQM) systems. The author served as Data Quality (DQ) Co-Coordinator for a significant portion of their time in the Ph.D. program. During their tenure, it was their responsibility to verify the integrity and sign off on all physics data coming out of TileCal.

A.1 ATLAS Data Quality

The process of data collection with the ATLAS detector begins with an LHC fill. Each fill corresponds to injections of protons into the LHC in preparation for data taking. When the beams are collimated and focused, the LHC team declares a period of “stable beams”. At this point, the ATLAS team begins to ramp up the high voltage in the tracker and muon systems. Once the pixel preamplifiers are turned on, ATLAS declares “ready for physics”. Data collected by ATLAS is recorded against a six digit number referred to as a run number. Each run is subdivided into Luminosity Blocks (LBs), with each LB corresponding to 60 seconds of data taking. LBs provide a granularity for checking quality of data and sorting of data based on its quality.

A.2 Calibration Systems

To ensure the data being collected by TileCal is accurate and meets the required standards a series of calibration checks are performed with varying frequency. The systems used for calibration were designed to be built into the full detector; allowing calibration between physics data taking runs without requiring physical access to the detector. A diagram of the various calibration systems and where in the readout chain each calibration is done can be seen in Figure A.1.

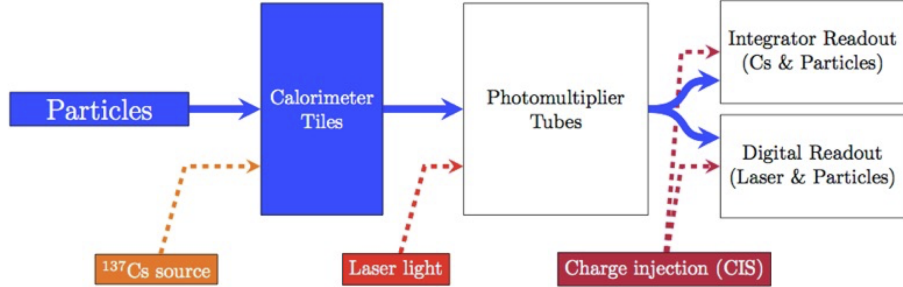


Figure A.1: TileCal calibration checks within the readout chain [26].

The cesium calibration system within TileCal is meant to calibrate the entire readout chain from scintillator to final digital signal readout. Several sources of CS_{137} are hydraulically moved throughout the detector. The cesium calibration was designed to be run once a month.¹ The laser calibration system measures the response of the PMTs with respect to the last cesium scan. Laser calibration can be done during empty bunches within the LHC fill and with dedicated calibration runs as well. The Charge Injection System (CIS) measures the response of digitizers and readout electronics by injecting controlled charges into the electronics. CIS calibration is done with dedicated calibration runs. The last calibration system is the minimum bias system, where physics signal is integrated over $\sim 10 - 20$ ms. Minimum bias calibration is used to fill in the gaps between cesium calibration scans. The average response variation for one cell from the laser, cesium, and minimum bias systems can be seen in Figure A.2.

Calibration constants are extracted from each calibration system and stored in a central ATLAS conditions database. Bookkeeping is done with an Interval of Validity (IOV) that corresponds to specific LBs within a run. The energy reconstructed at the EM scale is

$$E = \frac{A[\text{ADC Counts}]}{C_{Cs} \cdot C_{Las} \cdot C_{CIS}[\text{ADC counts}/\mu\text{C}] \cdot C_{TB}[\mu\text{C}/\text{GeV}]} \quad (\text{A.1})$$

¹Due to historical issues with leaking hydraulic fluid, the frequency of cesium scans was drastically reduced during Run-2.

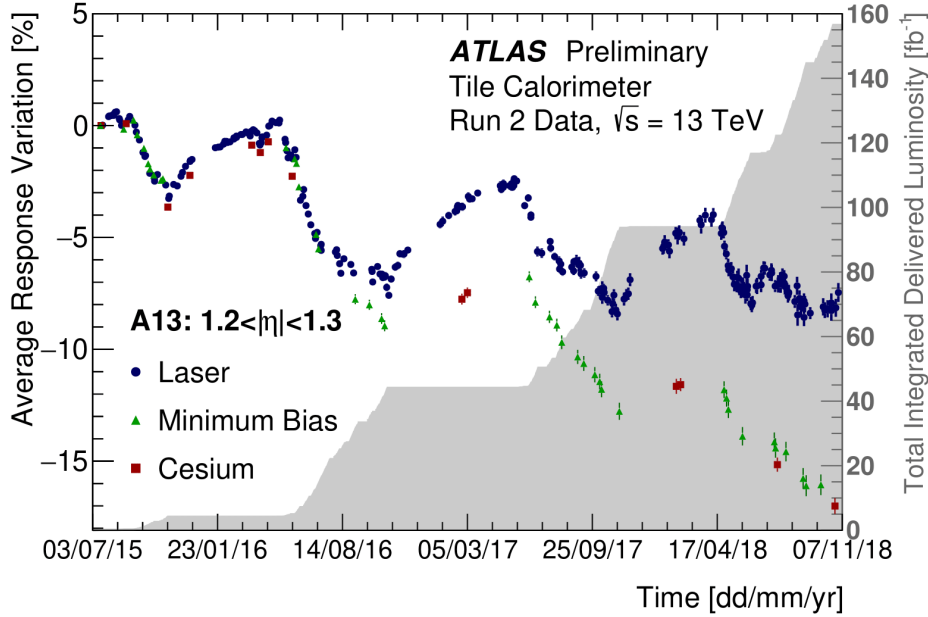


Figure A.2: Average response variation from the beginning of Run-2 of TileCal cell A13 is shown [73].

where A is the amplitude of the PMT signal after it has been shaped, amplified, and digitized at 40 MHz with 10-bit Analog to Digital Converters (ADCs) and C_{TB} is a calibration constant that was determined at dedicated test beams.

A.3 TileCal Data Quality

Quality of data is monitored both online and offline; a schematic of the path of data can be seen in Figure A.3. Online monitoring offers real time feedback on the data being collected, whereas offline monitoring is delayed but more detailed. Approximately 10% of collision events are quickly reconstructed in an express data stream. The data in this express stream is reviewed within 48 hours to allow subsystems an opportunity to change calibration constants and/or mask channels deemed bad. Figure A.4 shows the evolution of TileCal

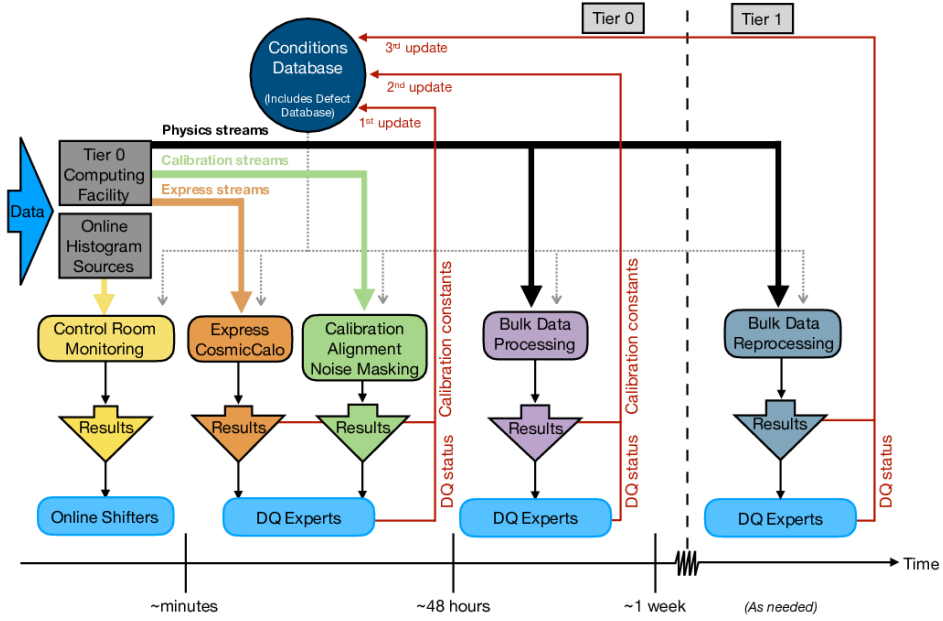


Figure A.3: Schematic diagram illustrating the nominal Run-2 operations workflow for the data quality assessment of ATLAS data. Online histogram sources include the high-level trigger farm, the data acquisition system, and full reconstruction of a fraction of events accepted by the trigger [74].

masked channels and cells throughout Run-2. After the 48 hour window, the full run is reconstructed using the updated conditions and once again reviewed by subsystem experts. The subsystem experts then approve the data or reject it based on a combination of automated test and human judgement. Figure A.5 shows the amount of collected luminosity throughout Run-2 and how much of it passes the “good for physics” requirements and Figure A.6 shows the overall efficiency of the whole ATLAS detector. Figure A.7 shows the inefficiencies by subsystem. For the whole of Run-2 TileCal was 99.65% efficient in terms of data quality.

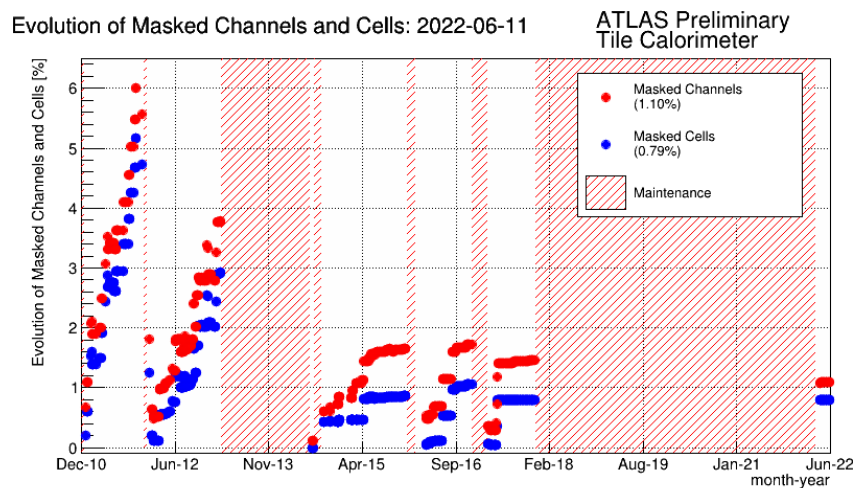


Figure A.4: Evolution of masked TileCal cells during Run-2 [73].

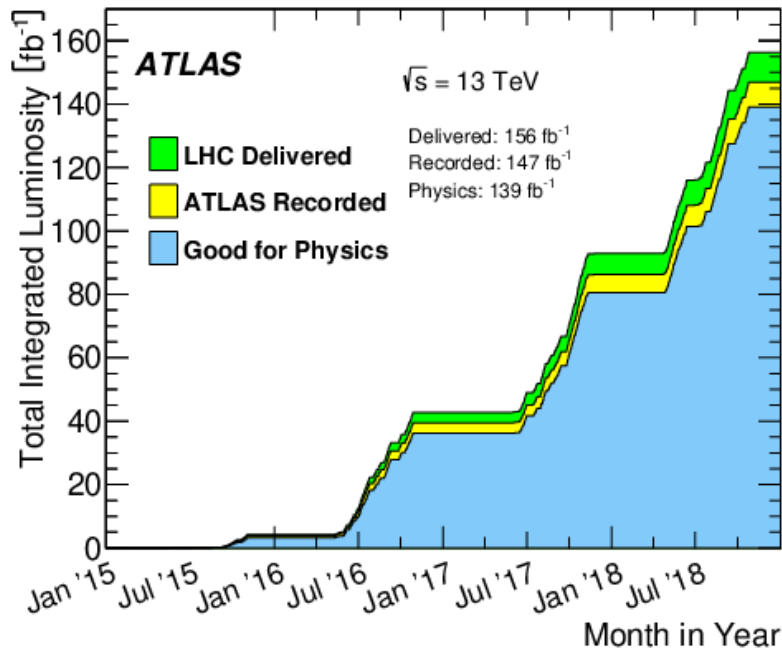


Figure A.5: Cumulative integrated luminosity delivered to and recorded by ATLAS between 2015 and 2018 during stable beam pp collision data-taking at $\sqrt{s} = 13$ TeV . This includes machine commissioning periods, special runs for detector calibration, and LHC fills with a low number of circulating bunches or bunch spacing greater than 25 ns. Also shown is the cumulative integrated luminosity certified for physics analysis usage for the ATLAS experiment between 2015 and 2018 during standard pp collision data-taking at $\sqrt{s} = 13$ TeV . The total integrated luminosity recorded for the standard $\sqrt{s} = 13$ TeV pp collision dataset corresponds to 145 fb^{-1} . It is this number that is used in the denominator when calculating the data quality efficiency of the standard $\sqrt{s} = 13$ TeV pp collision dataset [74].

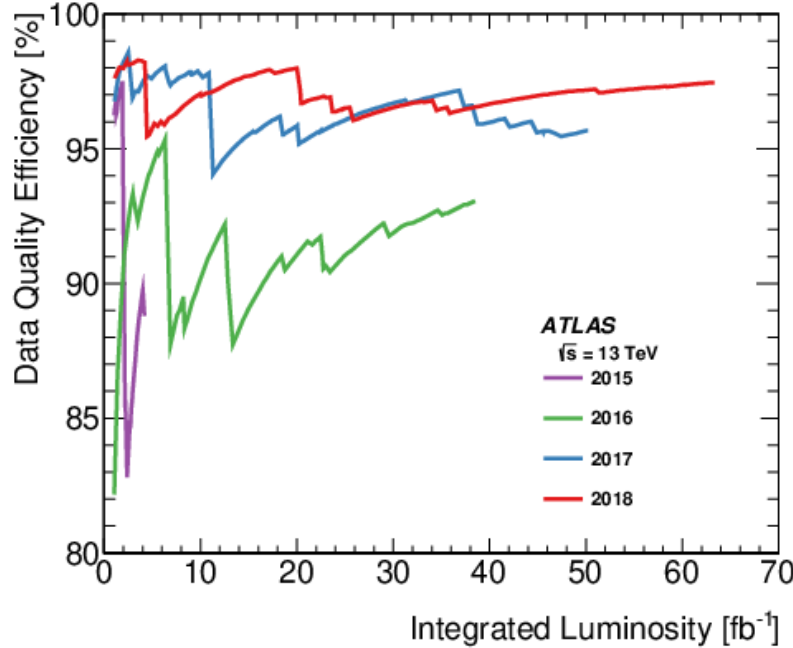


Figure A.6: Cumulative data quality efficiency versus total integrated luminosity delivered to the ATLAS experiment between 2015 and 2018 [74].

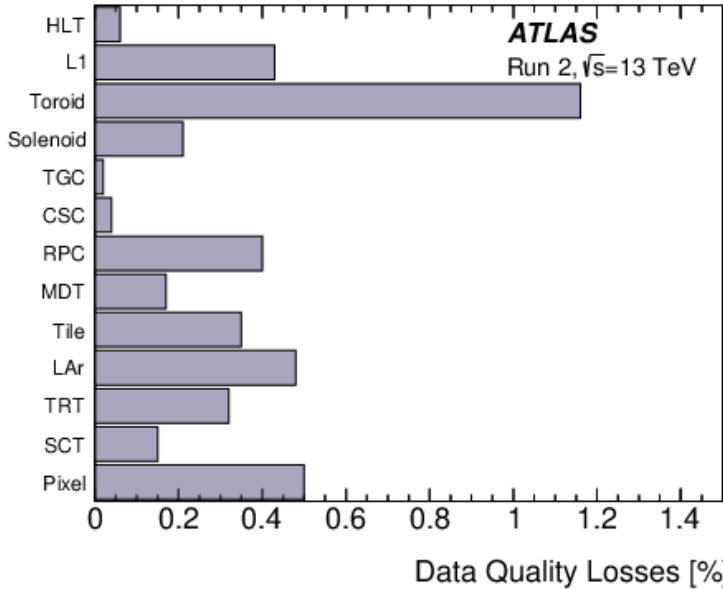


Figure A.7: Luminosity-weighted data quality inefficiencies (in %) during stable beams in standard pp collision physics runs at $\sqrt{s} = 13 \text{ TeV}$ between 2015 and 2018. [74].

APPENDIX B

FAKE FACTORS

This appendix contains supplementary material for the fake factor extraction procedure outlined in 6.3. Figures B.1 shows the fake factors for both multijet and W+jets CRs. Figure B.2 shows the extracted and corrected α values in the SRs and CRs. Figures B.3 through B.9 show the process of extracting the α values, including the fits.

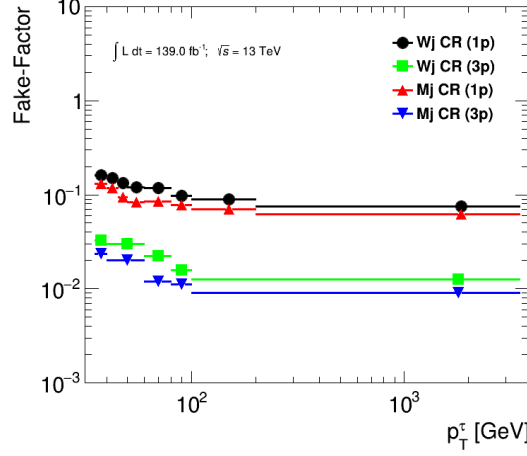


Figure B.1: Fake factors parameterized as a function of p_T^τ and the number of charged τ decay products (1-prong and 3-prong) obtained in the multi-jet and W+jets CRs. The errors shown represent the statistical uncertainty.

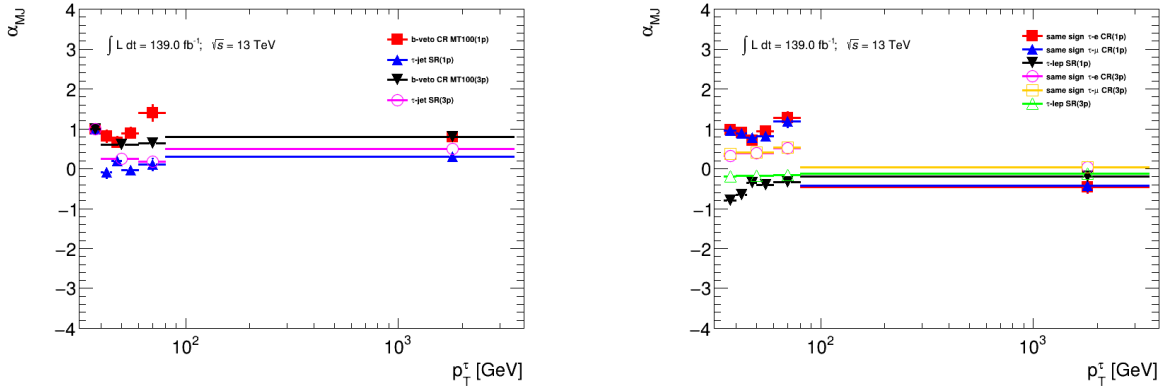


Figure B.2: Corrected α_{MJ} values for the $\tau_{had-vis} + \text{jets}$ b-veto $m_T > 100$ control region, $\tau_{had-vis} + \text{jets}$ signal region, $\tau_{had-vis} + \text{electron(muon)}$ with same-sign control region and the $\tau_{had-vis} + \text{lepton}$ signal region. Error bars represent uncertainties due to α_{MJ} fitting using template-fit method.

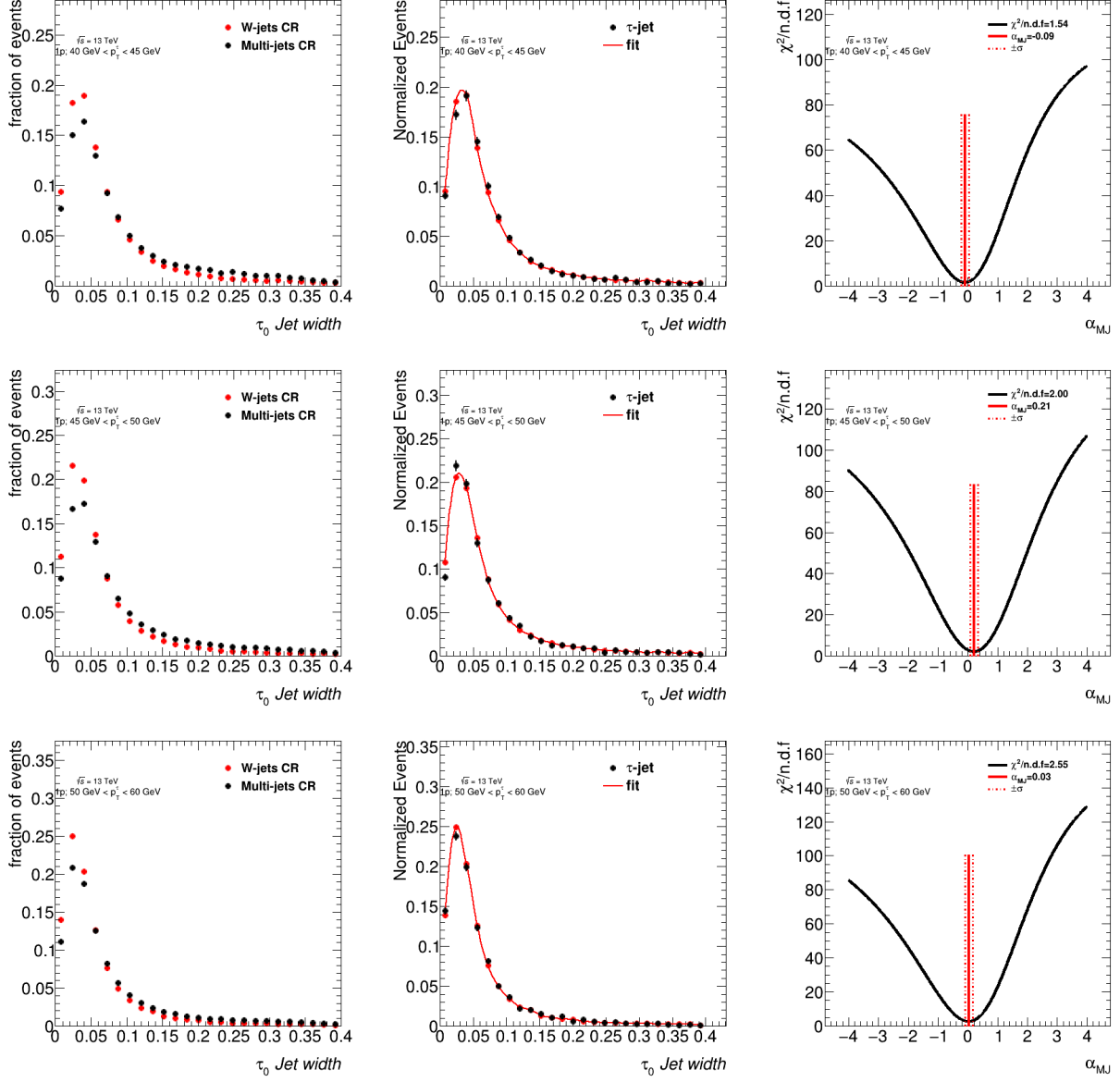


Figure B.3: Estimation of α_{MJ} in the $\tau_{had-vis} + \text{jets}$ signal region for $p_T \leq 60 \text{ GeV}$ 1-prong $\tau_{had-vis}$ candidates. Left: templates of discriminating variables for different $\tau_{had-vis}$ p_T and n-prong slices. Middle: shape of the discriminating variable obtained in the signal region and fitted shape using the templates measured in the control regions. Right: χ^2/ndf of the fit as a function of α_{MJ} , the error on α_{MJ} is defined by the band at $\chi^2_{\min}/\text{ndf} + \sqrt{\frac{2}{\text{ndf}}}$.

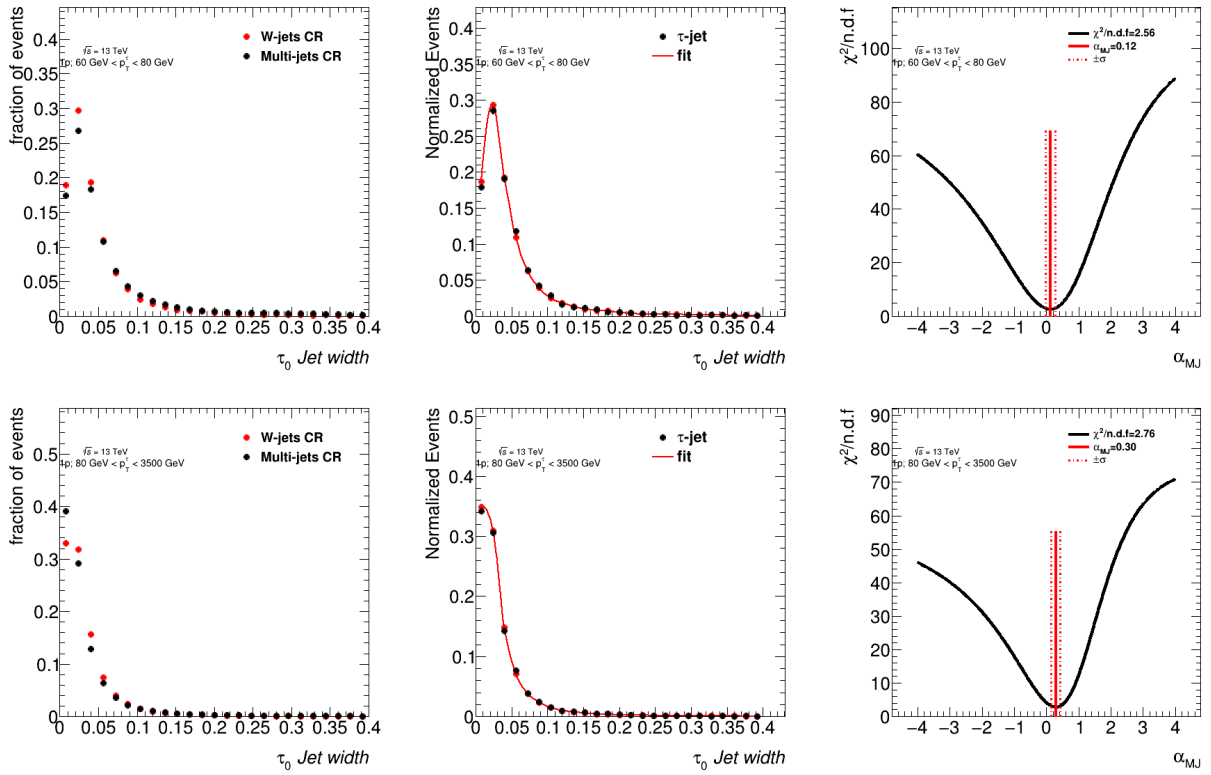


Figure B.4: Estimation of α_{MJ} in the $\tau_{had-vis} + \text{jets}$ signal region for $p_T \geq 60 \text{ GeV}$ 1-prong $\tau_{had-vis}$ candidates. Left: templates of discriminating variables for different $\tau_{had-vis}$ p_T and n-prong slices. Middle: shape of the discriminating variable obtained in the signal region and fitted shape using the templates measured in the control regions. Right: χ^2/ndf of the fit as a function of α_{MJ} , the error on α_{MJ} is defined by the band at $\chi^2_{\min}/\text{ndf} + \sqrt{\frac{2}{\text{ndf}}}$.

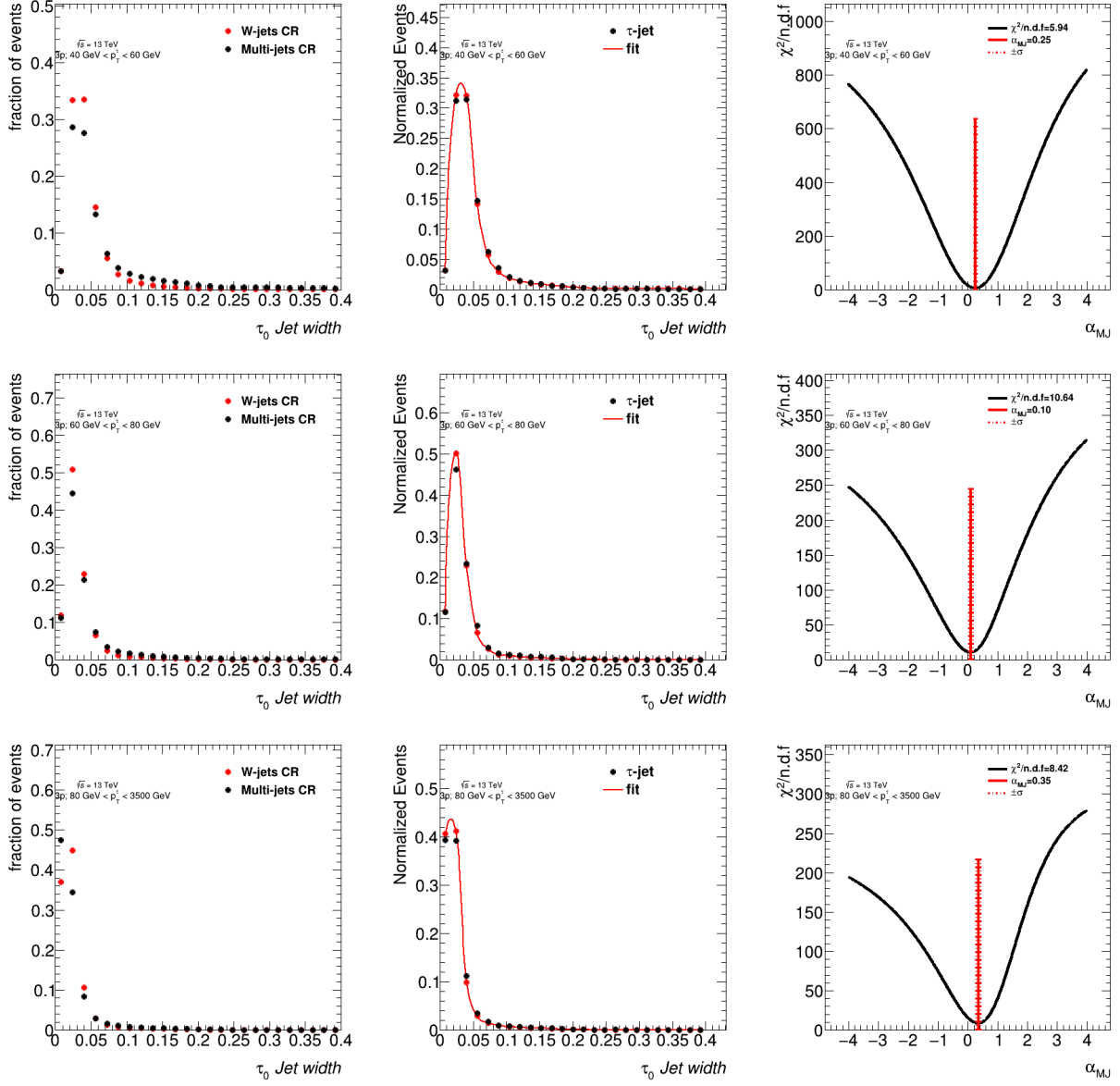


Figure B.5: Estimation of α_{MJ} in the $\tau_{\text{had-vis}} + \text{jets}$ signal region for 3-prong $\tau_{\text{had-vis}}$ candidates. Left: templates of discriminating variables for different $\tau_{\text{had-vis}}$ p_T and n-prong slices. Middle: shape of the discriminating variable obtained in the signal region and fitted shape using the templates measured in the control regions. Right: χ^2/ndf of the fit as a function of α_{MJ} , the error on α_{MJ} is defined by the band at $\chi^2_{\min}/\text{ndf} + \sqrt{\frac{2}{\text{ndf}}}$.

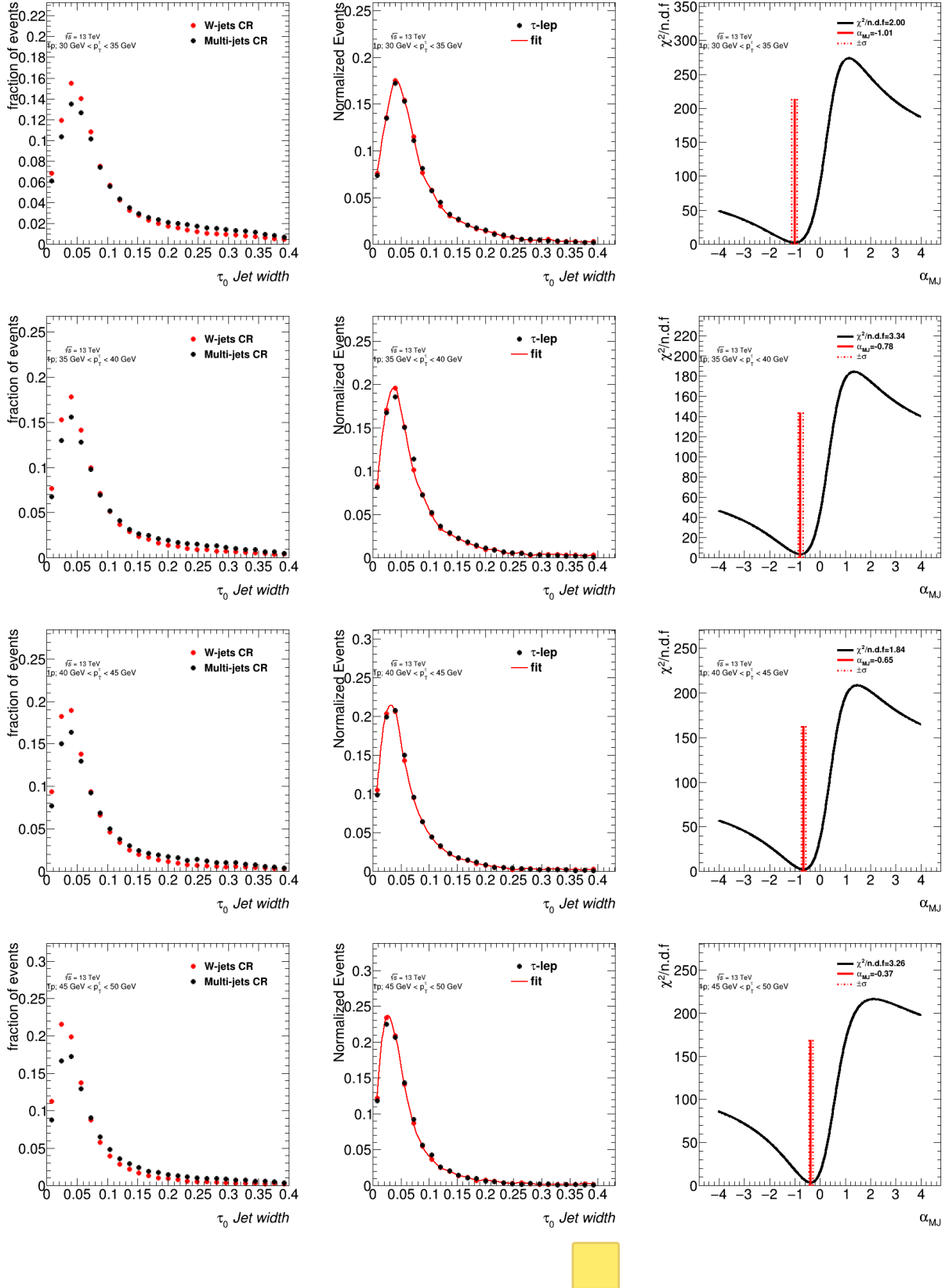


Figure B.6: Estimation of α_{MJ} in the $\tau_{\text{had-vis}} + \text{lepton}$ signal region for $p_T \leq 50 \text{ GeV}$ 1-prong $\tau_{\text{had-vis}}$ candidates. Left: templates of discriminating variables for different $\tau_{\text{had-vis}}$ p_T and n-prong slices. Middle: shape of the discriminating variable obtained in the signal region and fitted shape using the templates measured in the control regions. Right: χ^2/ndf of the fit as

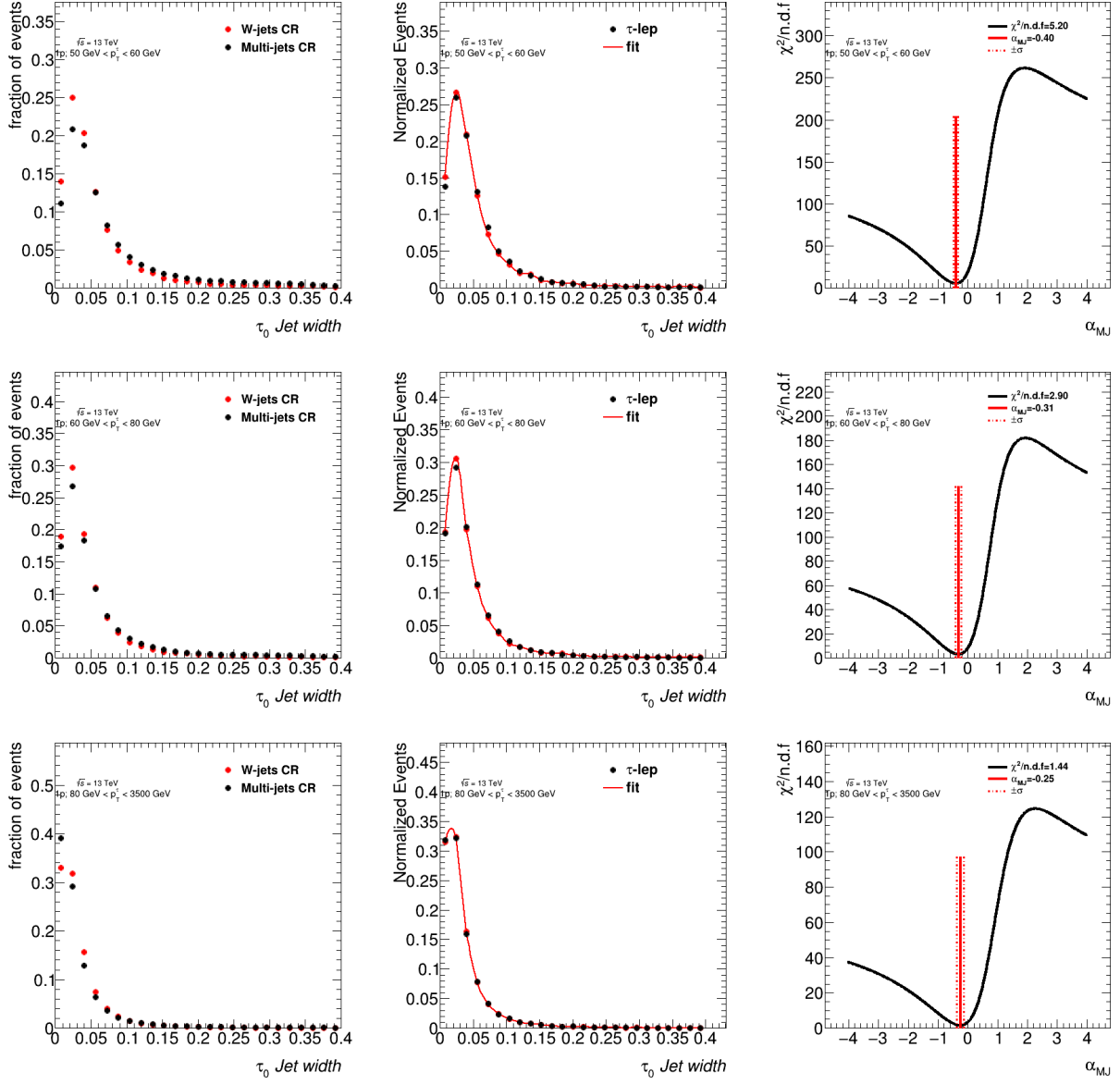


Figure B.7: Estimation of α_{MJ} in the $\tau_{had-vis}$ + lepton signal region for $p_T \geq 50 \text{ GeV}$ 1-prong $\tau_{had-vis}$ candidates. Left: templates of discriminating variables for different $\tau_{had-vis}$ p_T and n-prong slices. Middle: shape of the discriminating variable obtained in the signal region and fitted shape using the templates measured in the control regions. Right: χ^2/ndf of the fit as a function of α_{MJ} , the error on α_{MJ} is defined by the band at $\chi^2_{\min}/\text{ndf} + \sqrt{\frac{2}{\text{ndf}}}$.

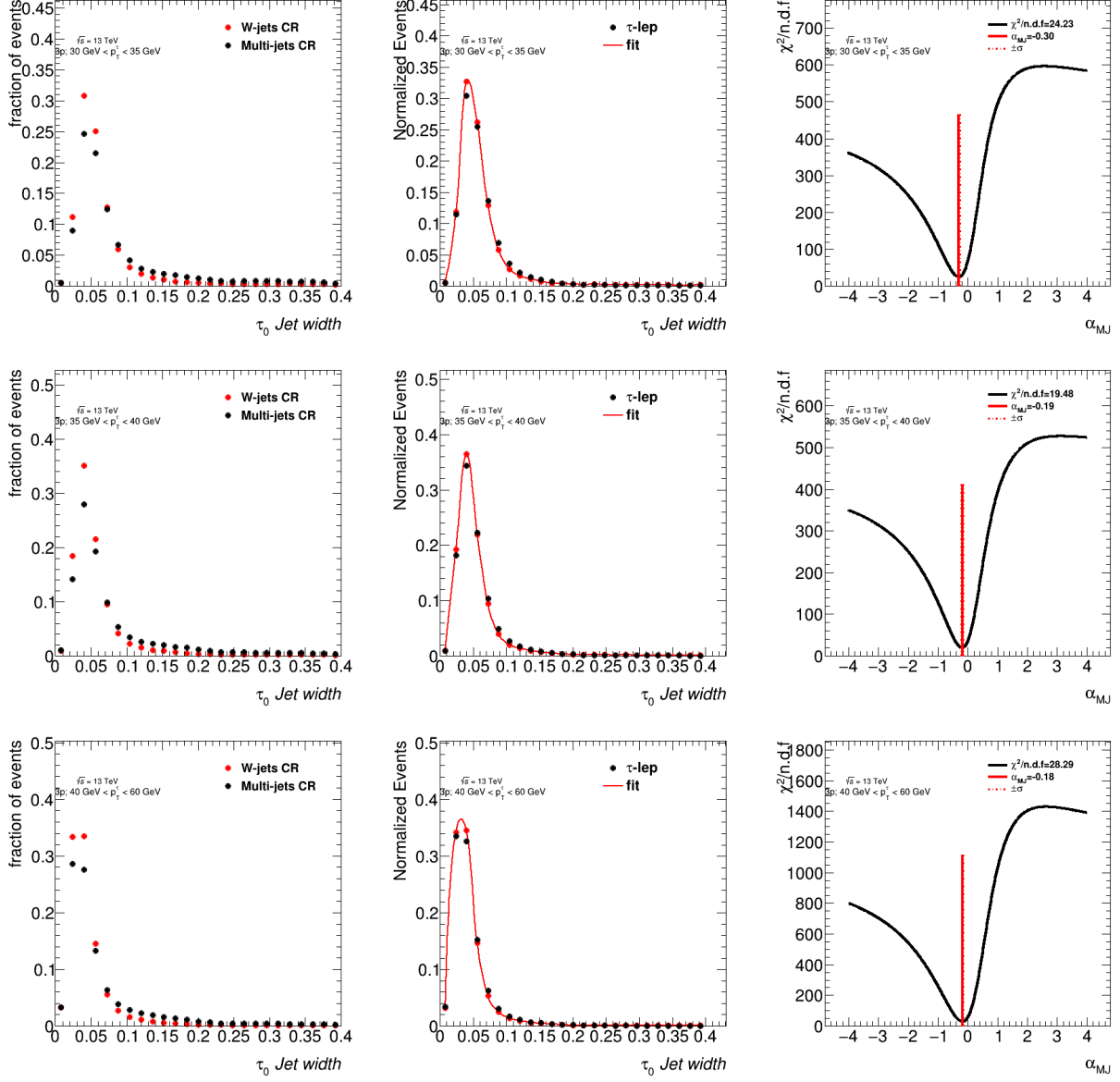


Figure B.8: Estimation of α_{MJ} in the $\tau_{had-vis}$ + lepton signal region for $p_T \leq 60 \text{ GeV}$ 3-prong $\tau_{had-vis}$ candidates. Left: templates of discriminating variables for different $\tau_{had-vis}$ p_T and n-prong slices. Middle: shape of the discriminating variable obtained in the signal region and fitted shape using the templates measured in the control regions. Right: χ^2/ndf of the fit as a function of α_{MJ} , the error on α_{MJ} is defined by the band at $\chi^2_{\min}/\text{ndf} + \sqrt{\frac{2}{\text{ndf}}}$.

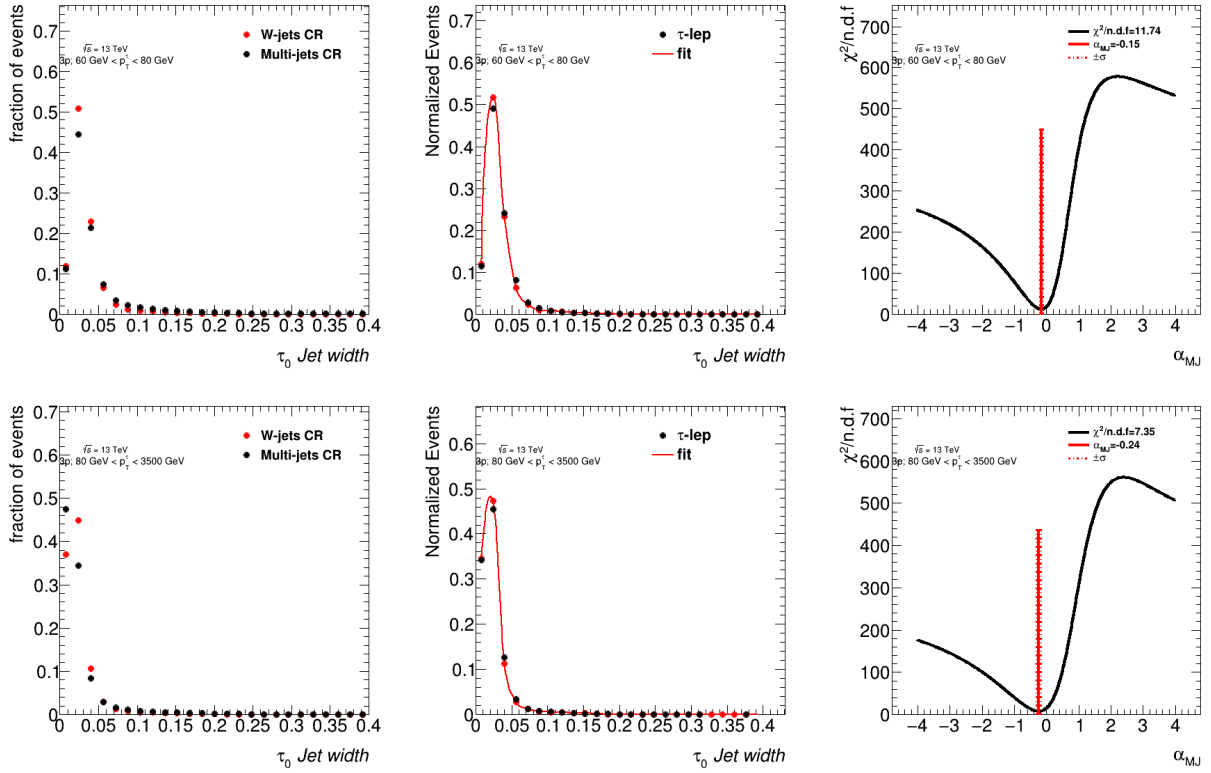


Figure B.9: Estimation of α_{MJ} in the $\tau_{\text{had-vis}} + \text{lepton}$ signal region for $p_T \geq 60 \text{ GeV}$ 3-prong $\tau_{\text{had-vis}}$ candidates. Left: templates of discriminating variables for different $\tau_{\text{had-vis}}$ p_T and n-prong slices. Middle: shape of the discriminating variable obtained in the signal region and fitted shape using the templates measured in the control regions. Right: χ^2/ndf of the fit as a function of α_{MJ} , the error on α_{MJ} is defined by the band at $\chi^2_{\min}/\text{ndf} + \sqrt{\frac{2}{\text{ndf}}}$.

APPENDIX C

ADDITIONAL VALIDATION PLOTS

C.1 $\tau + \text{jets}$ Background Validation Plots

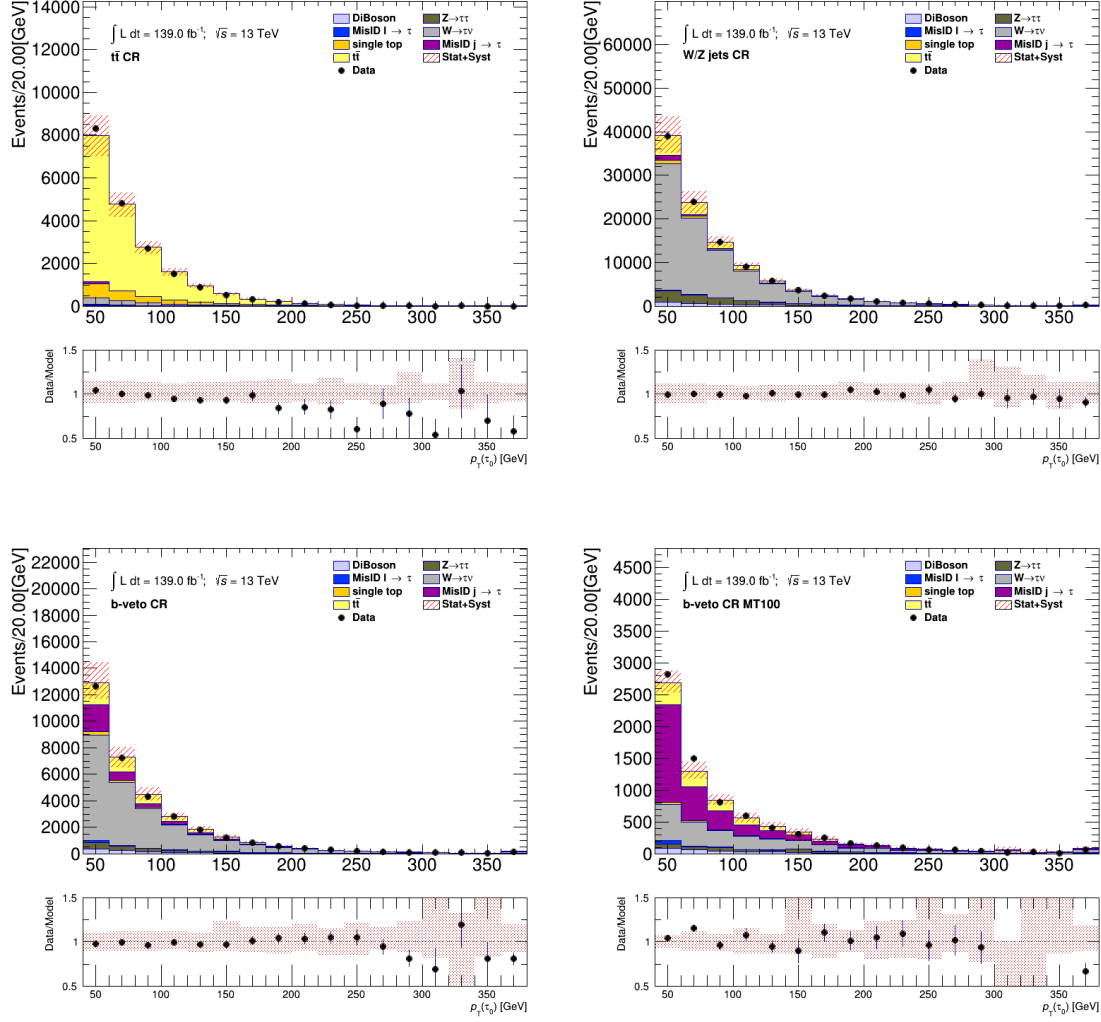


Figure C.1: Comparison between the predicted and the measured p_T^τ distributions in various control regions defined for the $\tau + \text{jets}$ channel. The uncertainty band includes both statistical and systematic uncertainties on the background prediction.

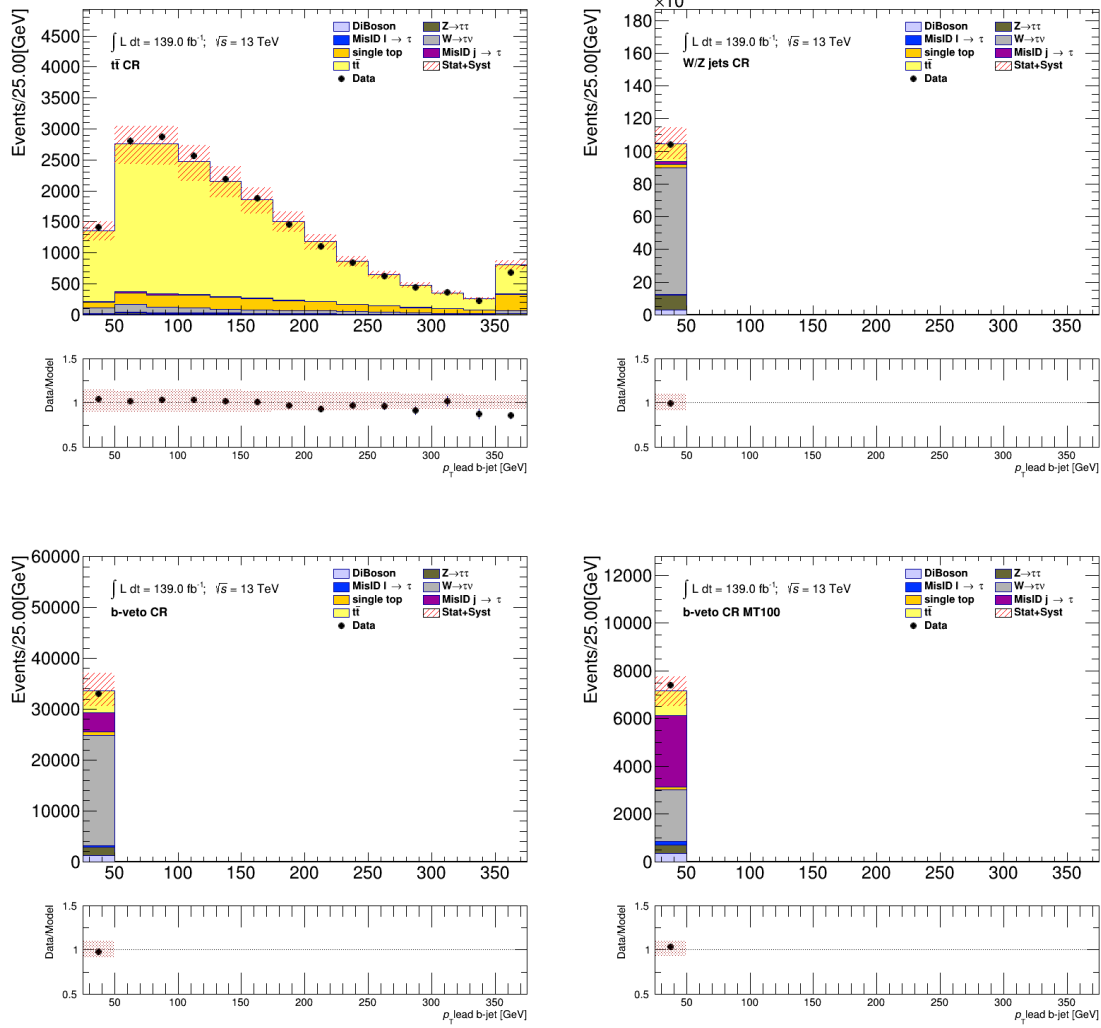


Figure C.2: Comparison between the predicted and the measured p_T^{b-jet} distributions in various control regions defined for the $\tau + \text{jets}$ channel. The uncertainty band includes both statistical and systematic uncertainties on the background prediction.

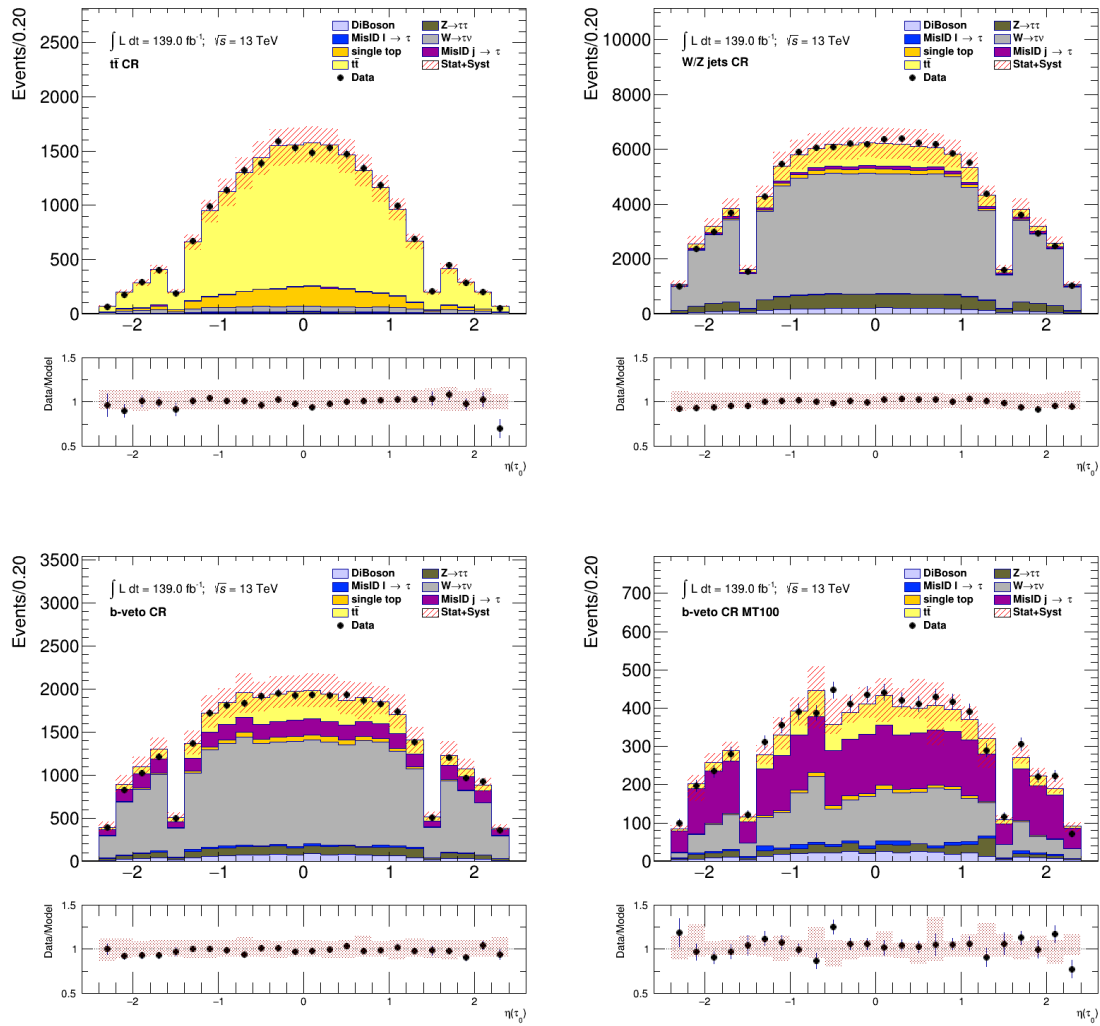


Figure C.3: Comparison between the predicted and the measured η^τ distributions in various control regions defined for the $\tau+\text{jets}$ channel. The uncertainty band includes both statistical and systematic uncertainties on the background prediction.

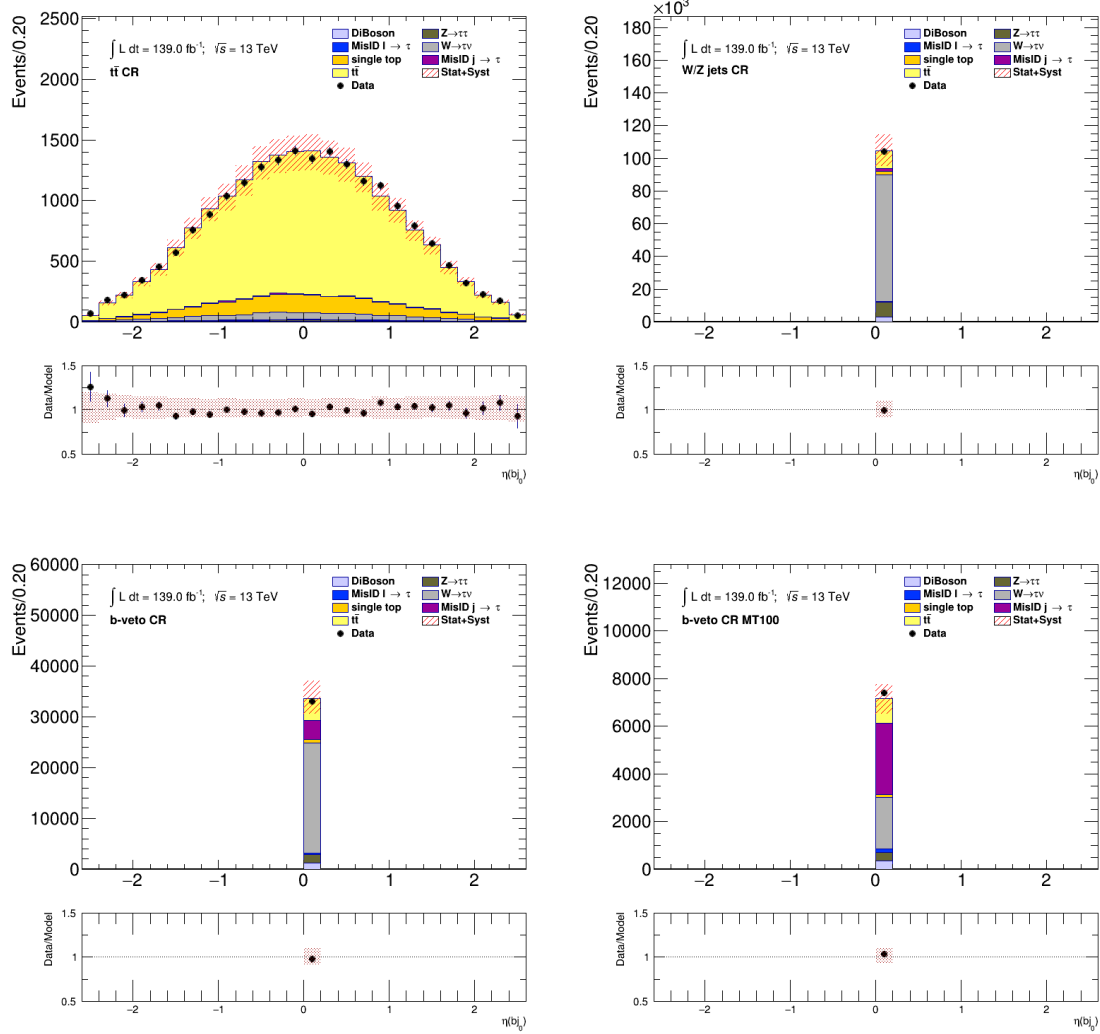


Figure C.4: Comparison between the predicted and the measured η^{b-jet} distributions in various control regions defined for the $\tau+jets$ channel. The uncertainty band includes both statistical and systematic uncertainties on the background prediction.

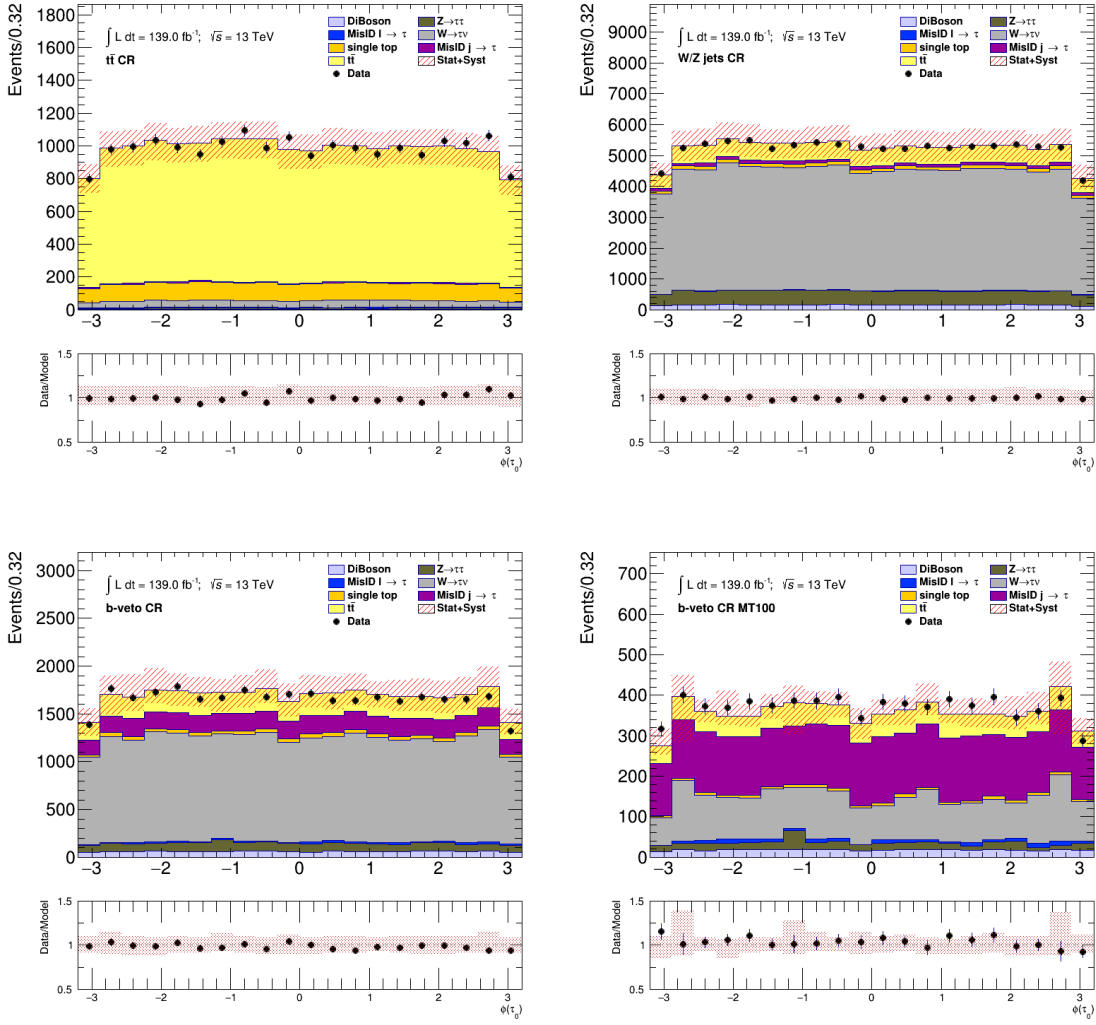


Figure C.5: Comparison between the predicted and the measured ϕ^τ distributions in various control regions defined for the $\tau+\text{jets}$ channel. The uncertainty band includes both statistical and systematic uncertainties on the background prediction.

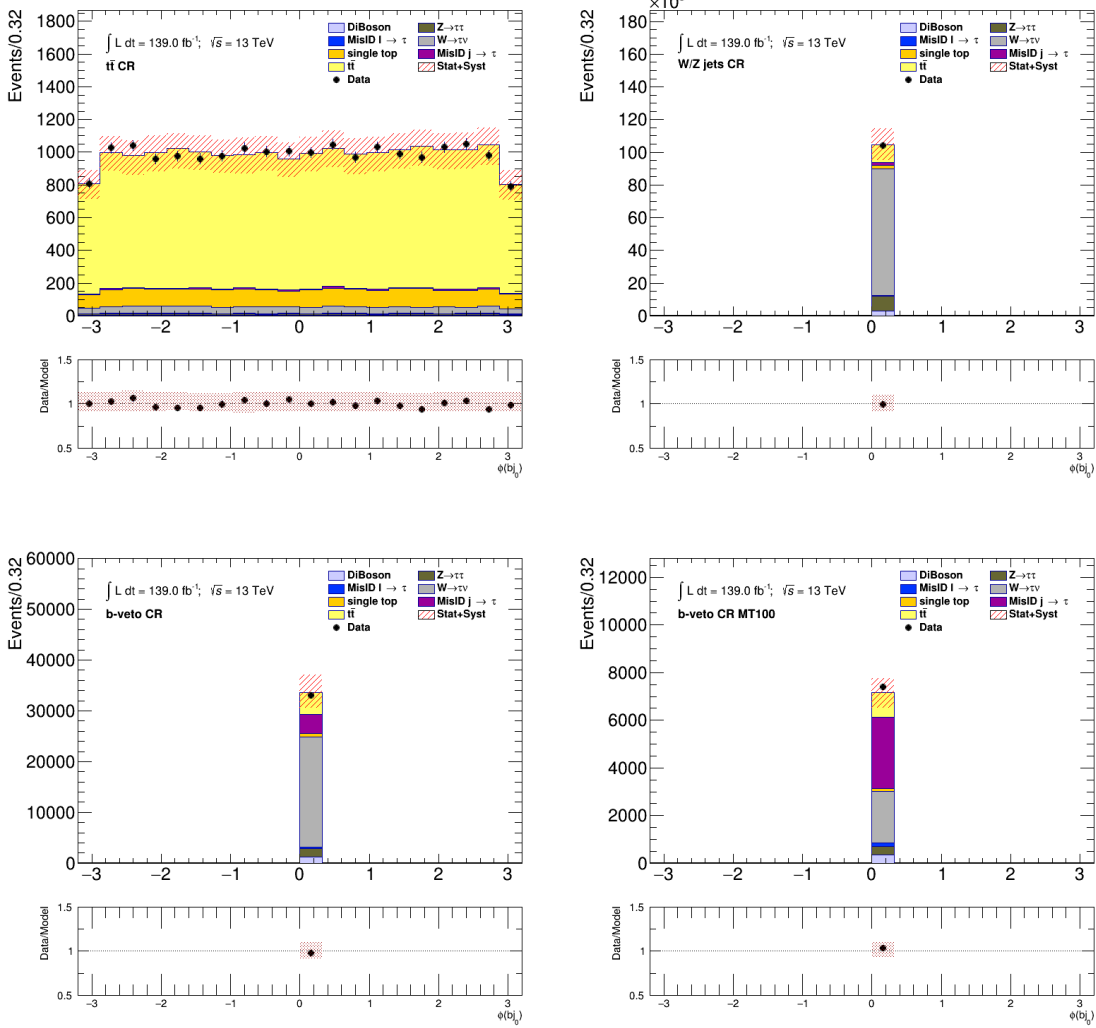


Figure C.6: Comparison between the predicted and the measured $\phi^{b\text{-jet}}$ distributions in various control regions defined for the $\tau+\text{jets}$ channel. The uncertainty band includes both statistical and systematic uncertainties on the background prediction.

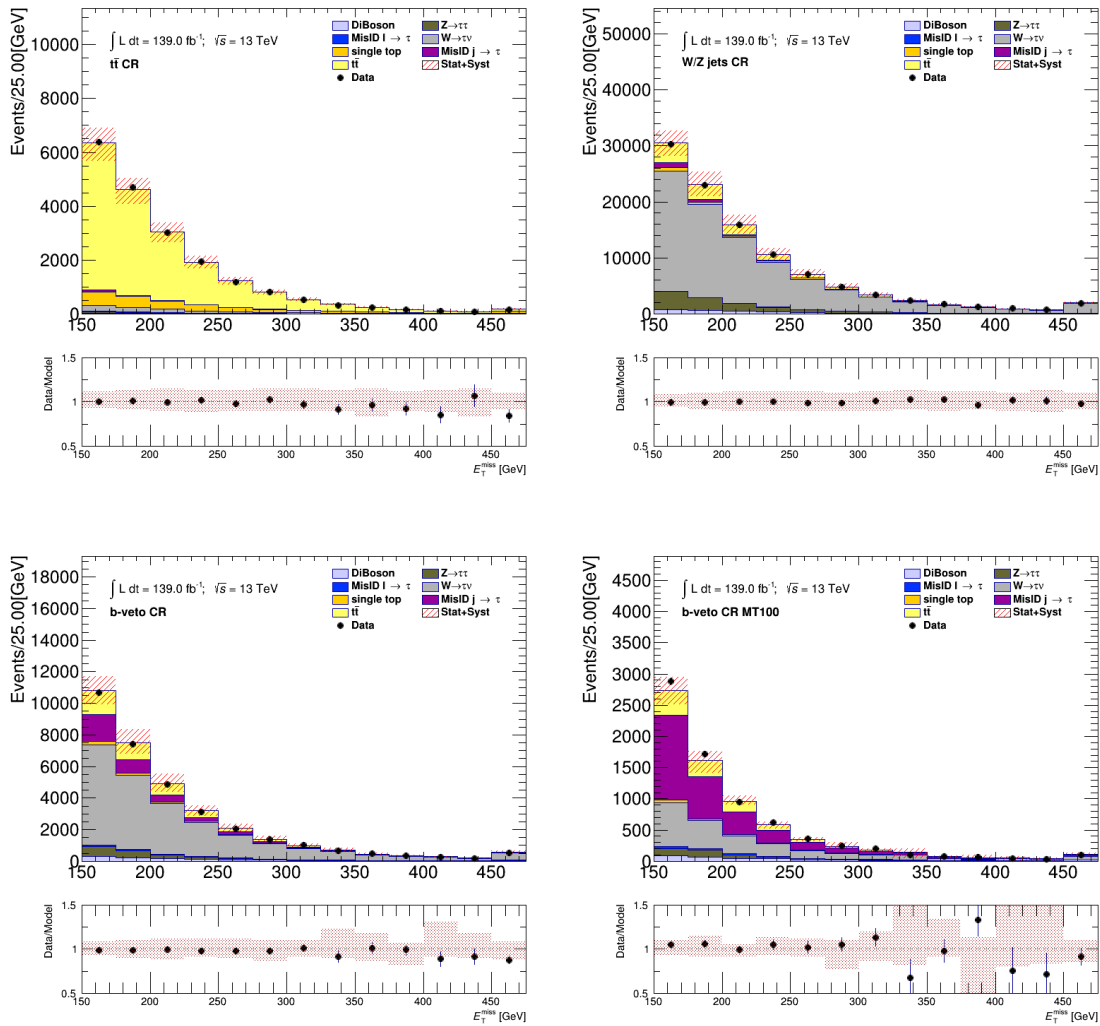


Figure C.7: Comparison between the predicted and the measured E_T^{miss} distributions in various control regions defined for the $\tau + \text{jets}$ channel. The uncertainty band includes both statistical and systematic uncertainties on the background prediction.

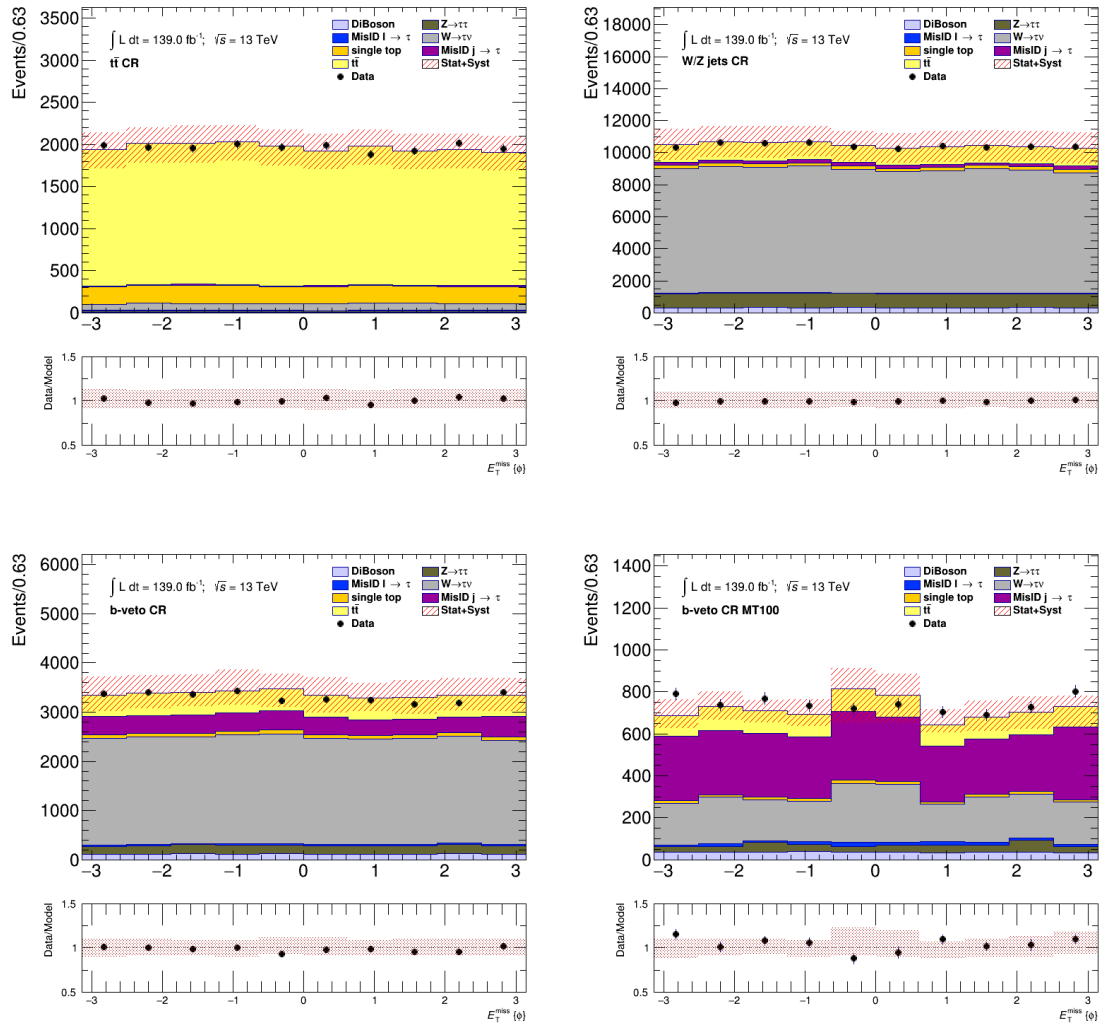


Figure C.8: Comparison between the predicted and the measured $\phi_{\text{T}}^{E_{\text{miss}}}$ distributions in various control regions defined for the $\tau + \text{jets}$ channel. The uncertainty band includes both statistical and systematic uncertainties on the background prediction.

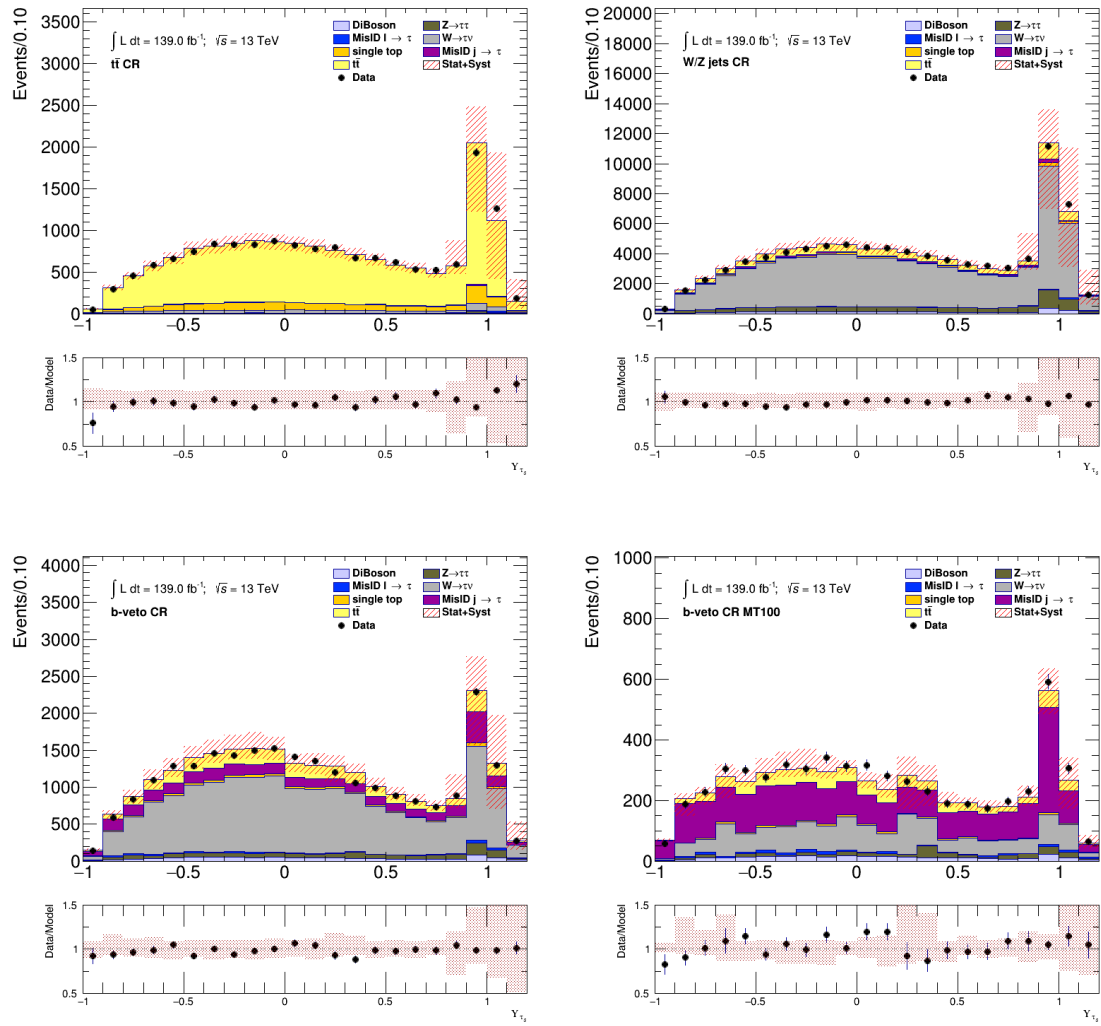


Figure C.9: Comparison between the predicted and the measured Υ_τ distributions in various control regions defined for the $\tau+\text{jets}$ channel. The uncertainty band includes both statistical and systematic uncertainties on the background prediction.

C.2 $\tau + \ell$ Background Validation Plots

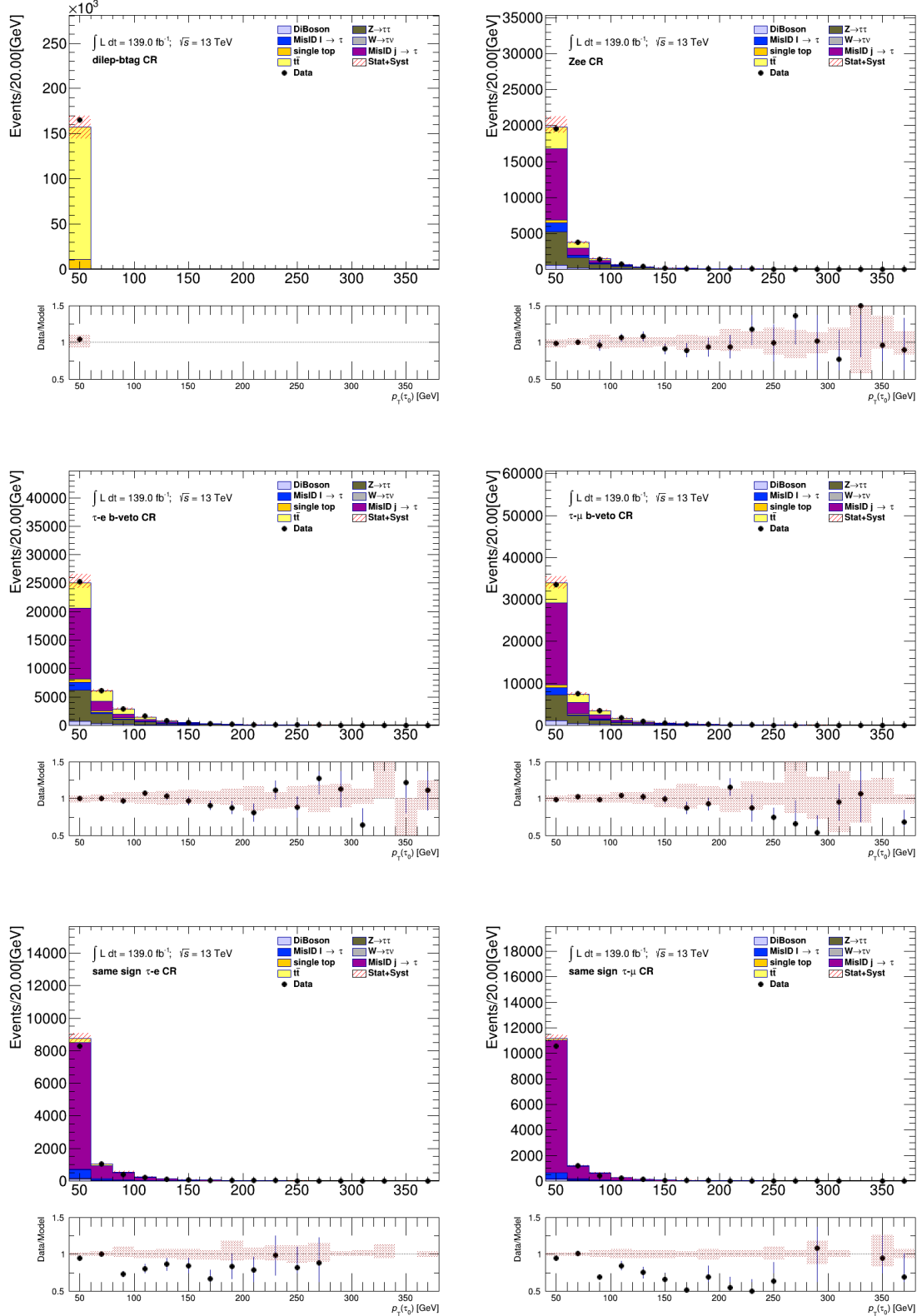


Figure C.10: Comparison between the predicted and the measured p_T^τ distributions in various control regions defined for the $\tau + \ell$ channel. The uncertainty band includes both statistical and systematic uncertainties on the background prediction.

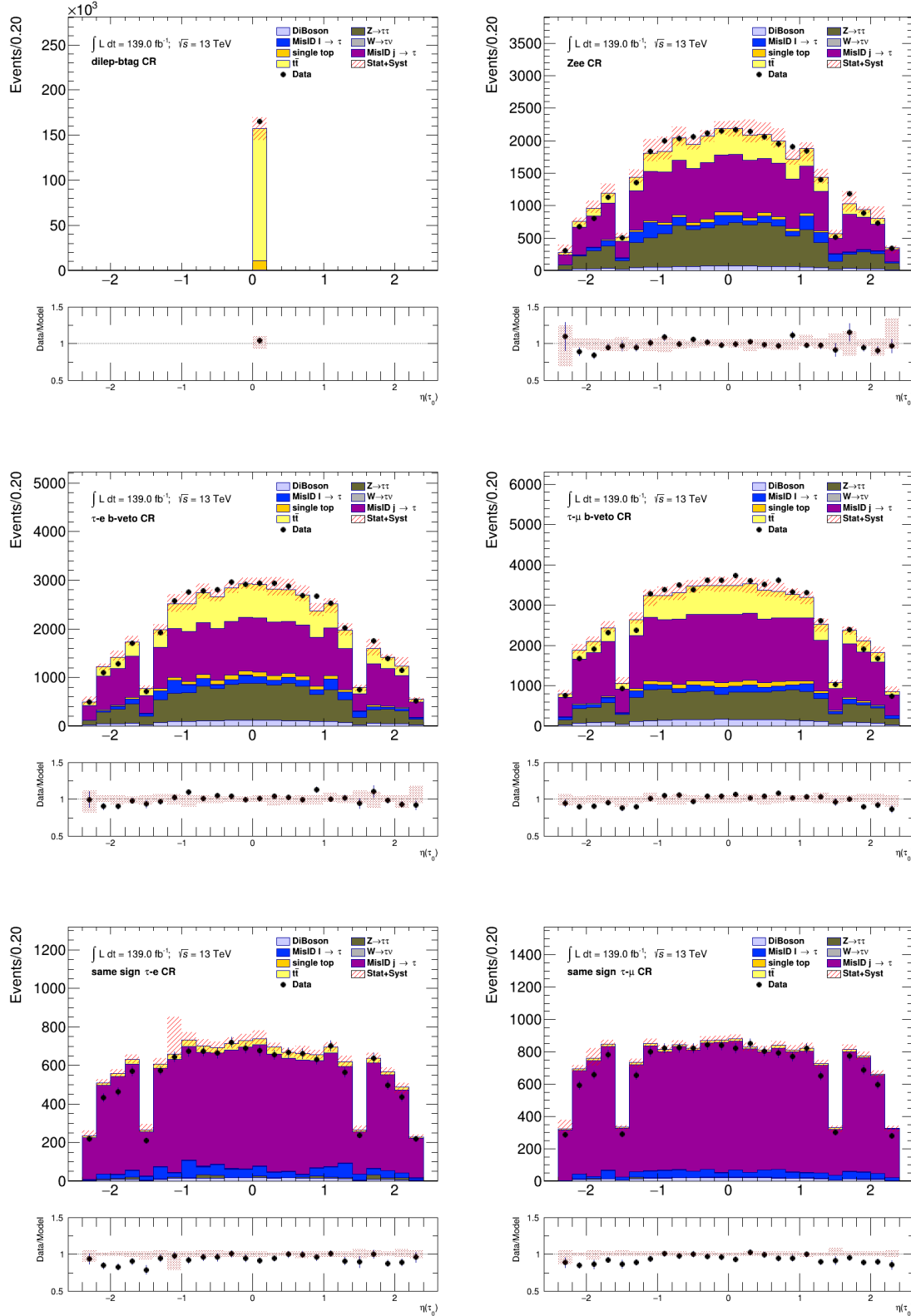


Figure C.11: Comparison between the predicted and the measured η^τ distributions in various control regions defined for the $\tau + \ell$ channel. The uncertainty band includes both statistical and systematic uncertainties on the background prediction.

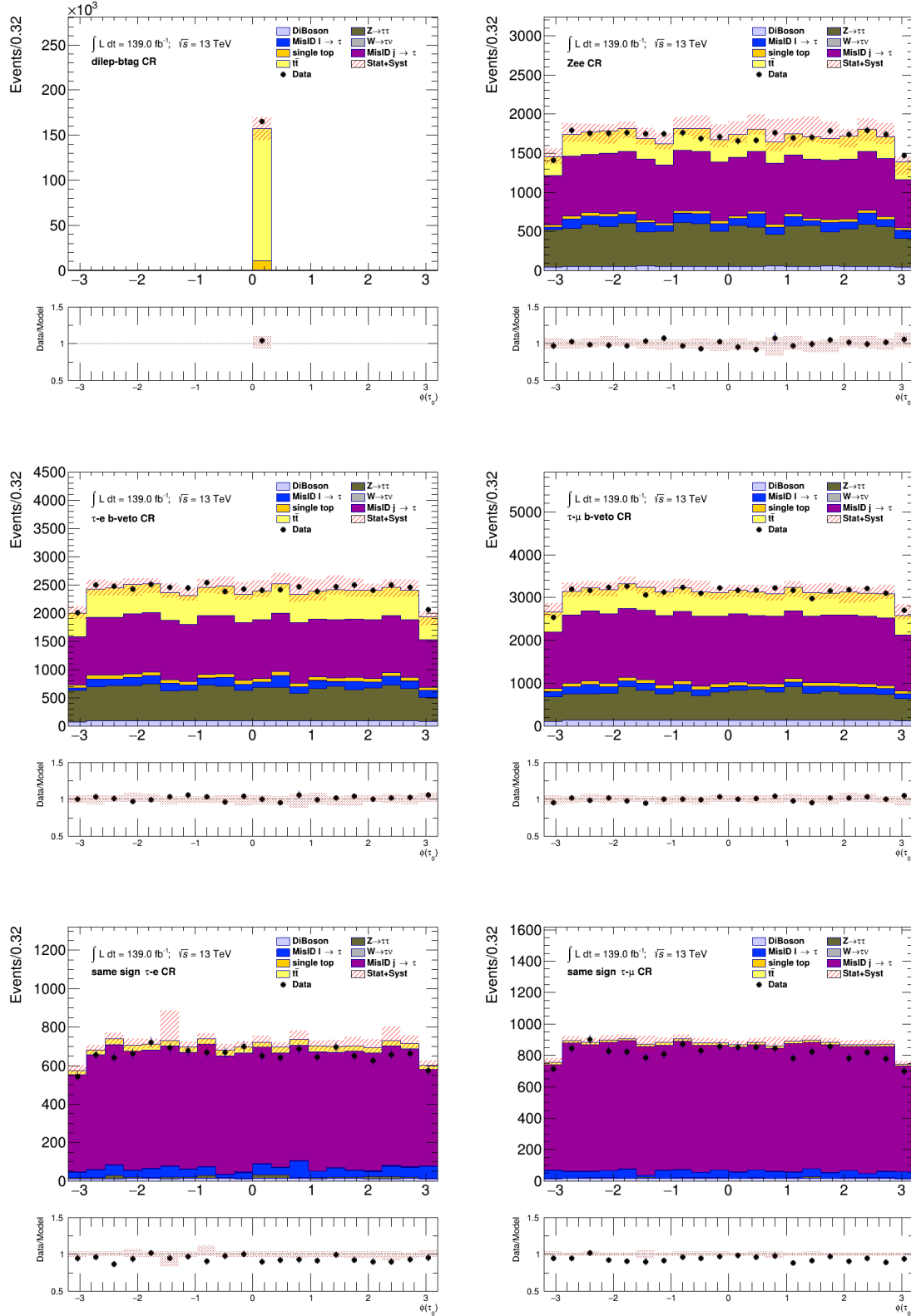


Figure C.12: Comparison between the predicted and the measured ϕ^τ distributions in various control regions defined for the $\tau + \ell$ channel. The uncertainty band includes both statistical and systematic uncertainties on the background prediction.

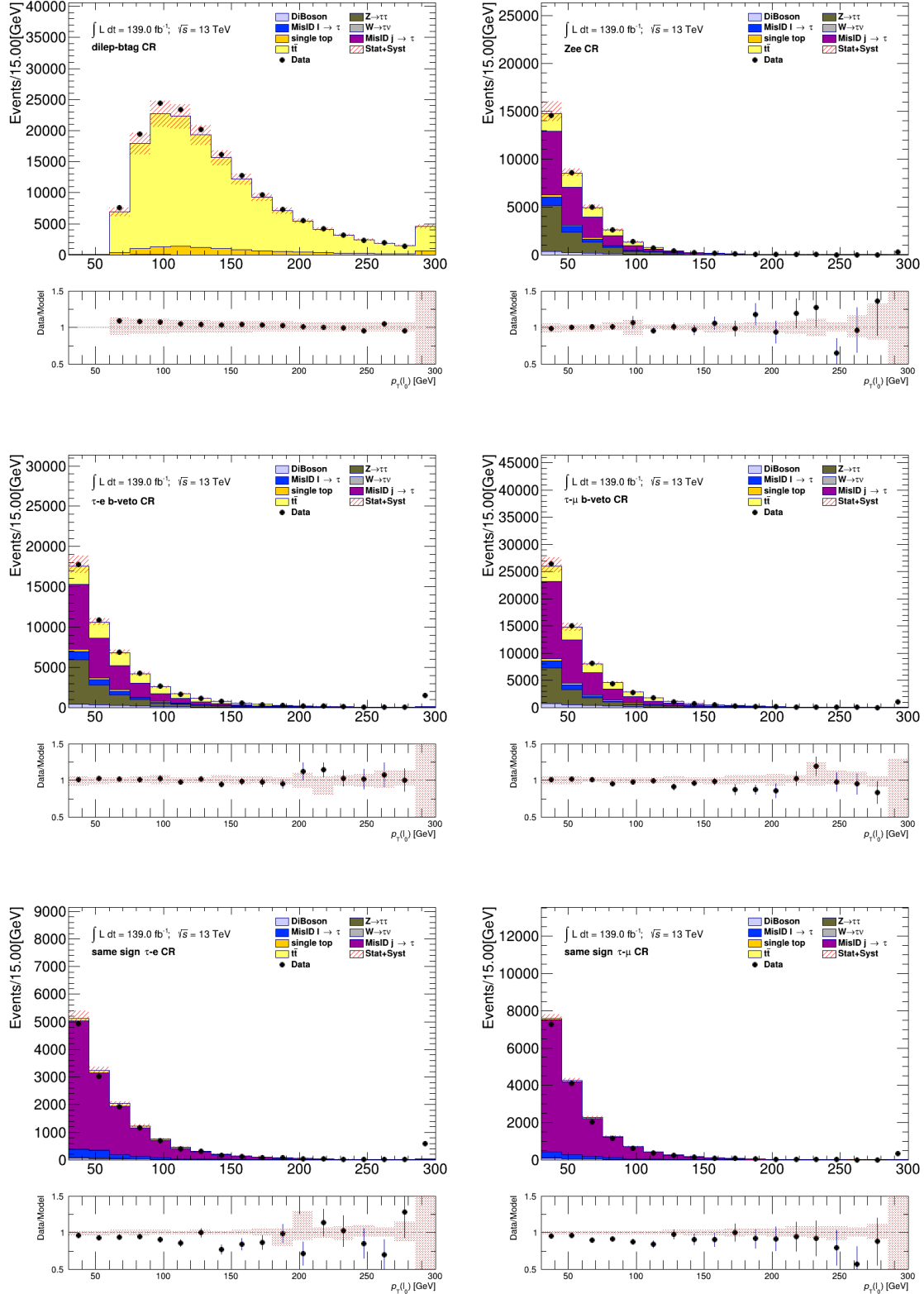


Figure C.13: Comparison between the predicted and the measured p_T^ℓ distributions in various control regions defined for the $\tau + \ell$ channel. The uncertainty band includes both statistical and systematic uncertainties on the background prediction.

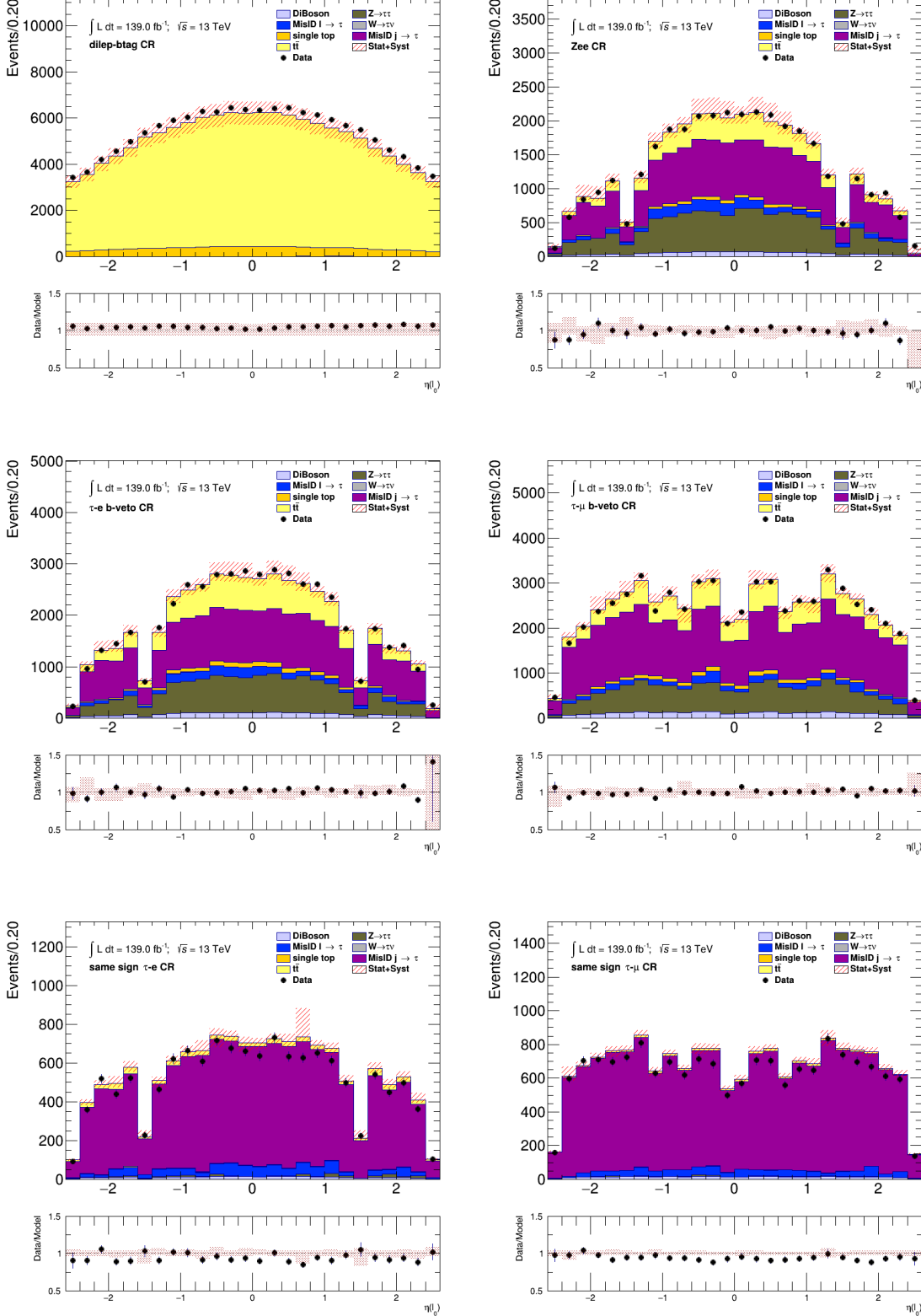


Figure C.14: Comparison between the predicted and the measured η^ℓ distributions in various control regions defined for the $\tau + \ell$ channel. The uncertainty band includes both statistical and systematic uncertainties on the background prediction.

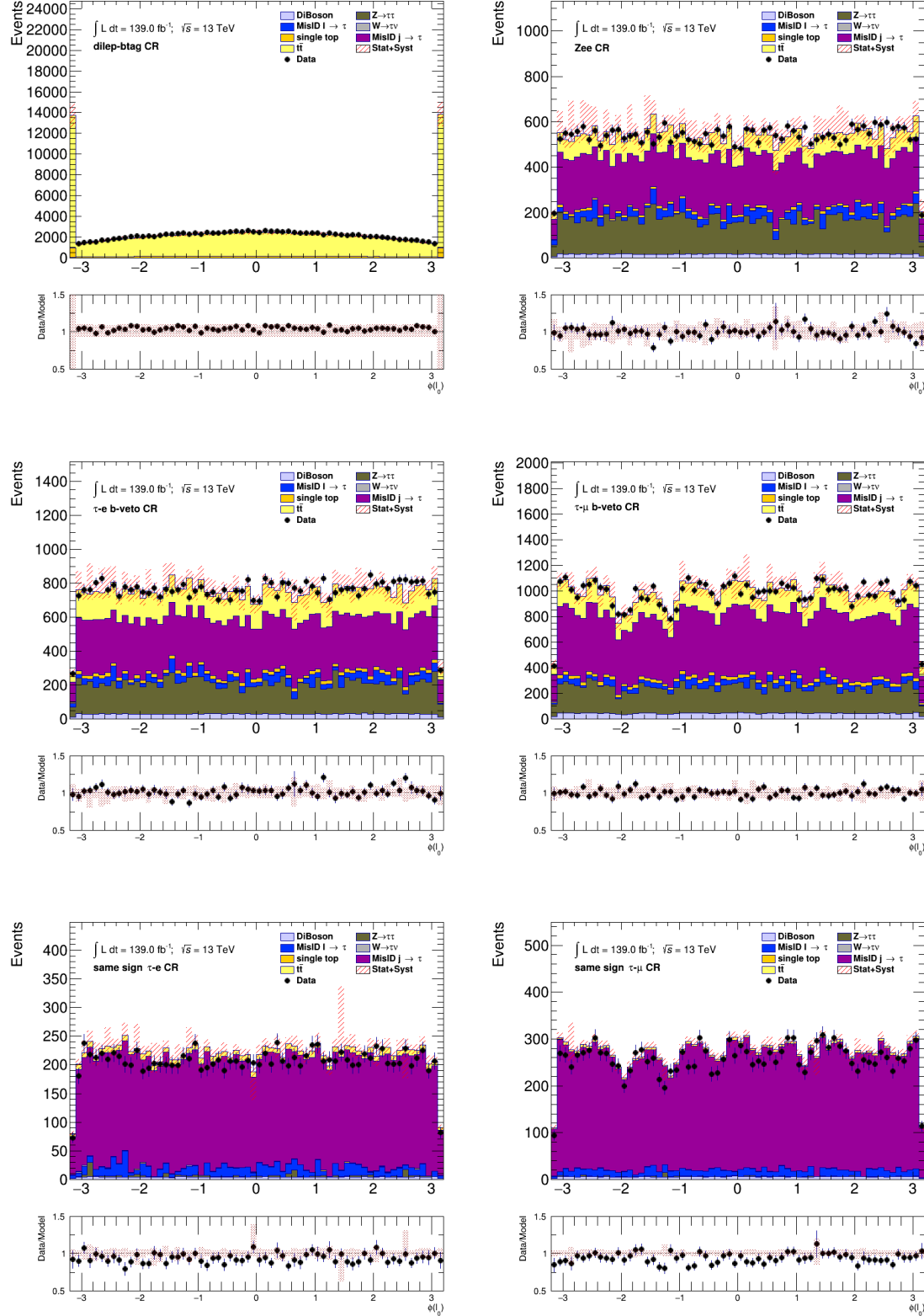


Figure C.15: Comparison between the predicted and the measured ϕ^ℓ distributions in various control regions defined for the $\tau + \ell$ channel. The uncertainty band includes both statistical and systematic uncertainties on the background prediction.

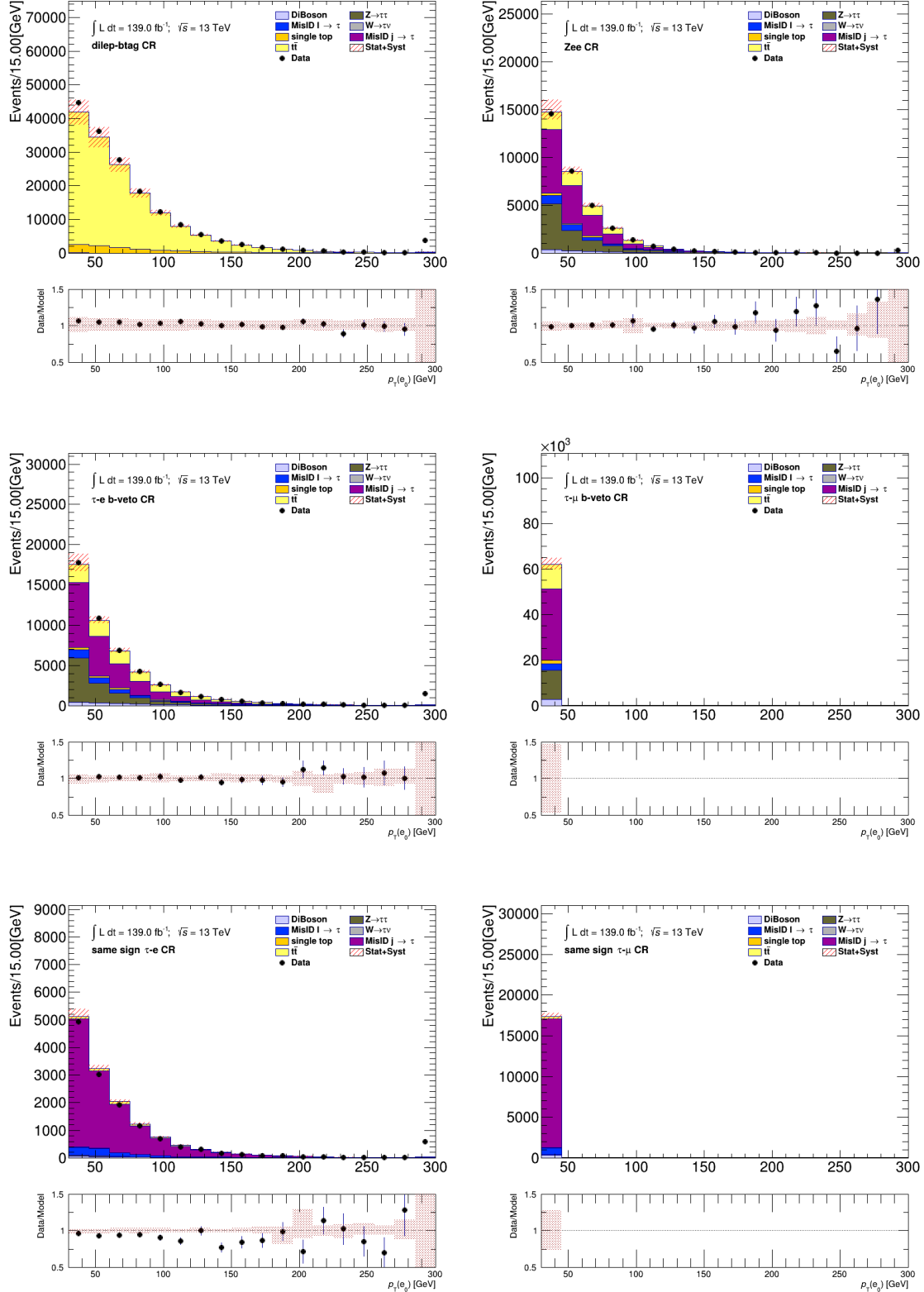


Figure C.16: Comparison between the predicted and the measured p_T^e distributions in various control regions defined for the $\tau + \ell$ channel. The uncertainty band includes both statistical and systematic uncertainties on the background prediction.

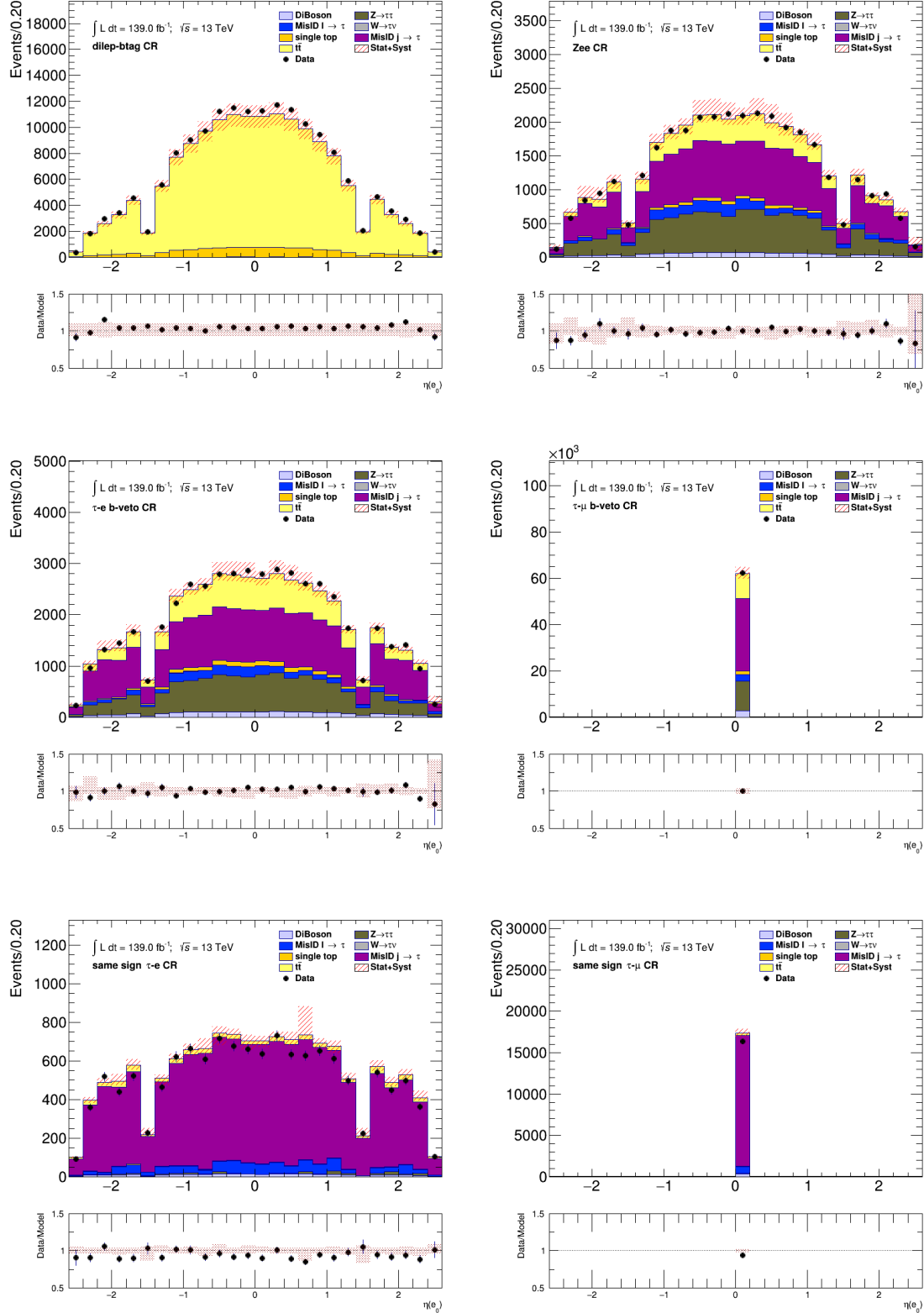


Figure C.17: Comparison between the predicted and the measured η^e distributions in various control regions defined for the $\tau + \ell$ channel. The uncertainty band includes both statistical and systematic uncertainties on the background prediction.

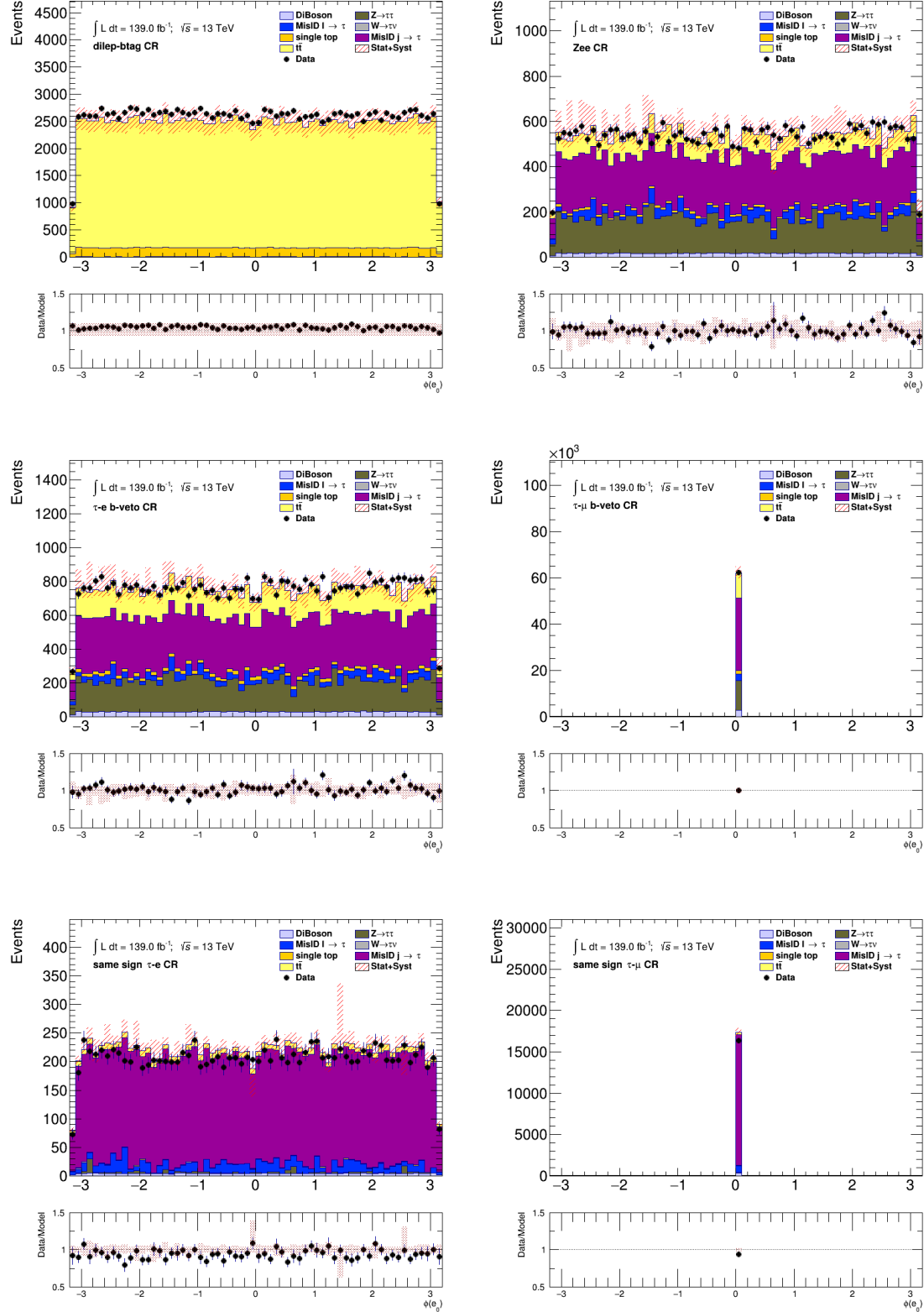


Figure C.18: Comparison between the predicted and the measured ϕ^e distributions in various control regions defined for the $\tau + \ell$ channel. The uncertainty band includes both statistical and systematic uncertainties on the background prediction.

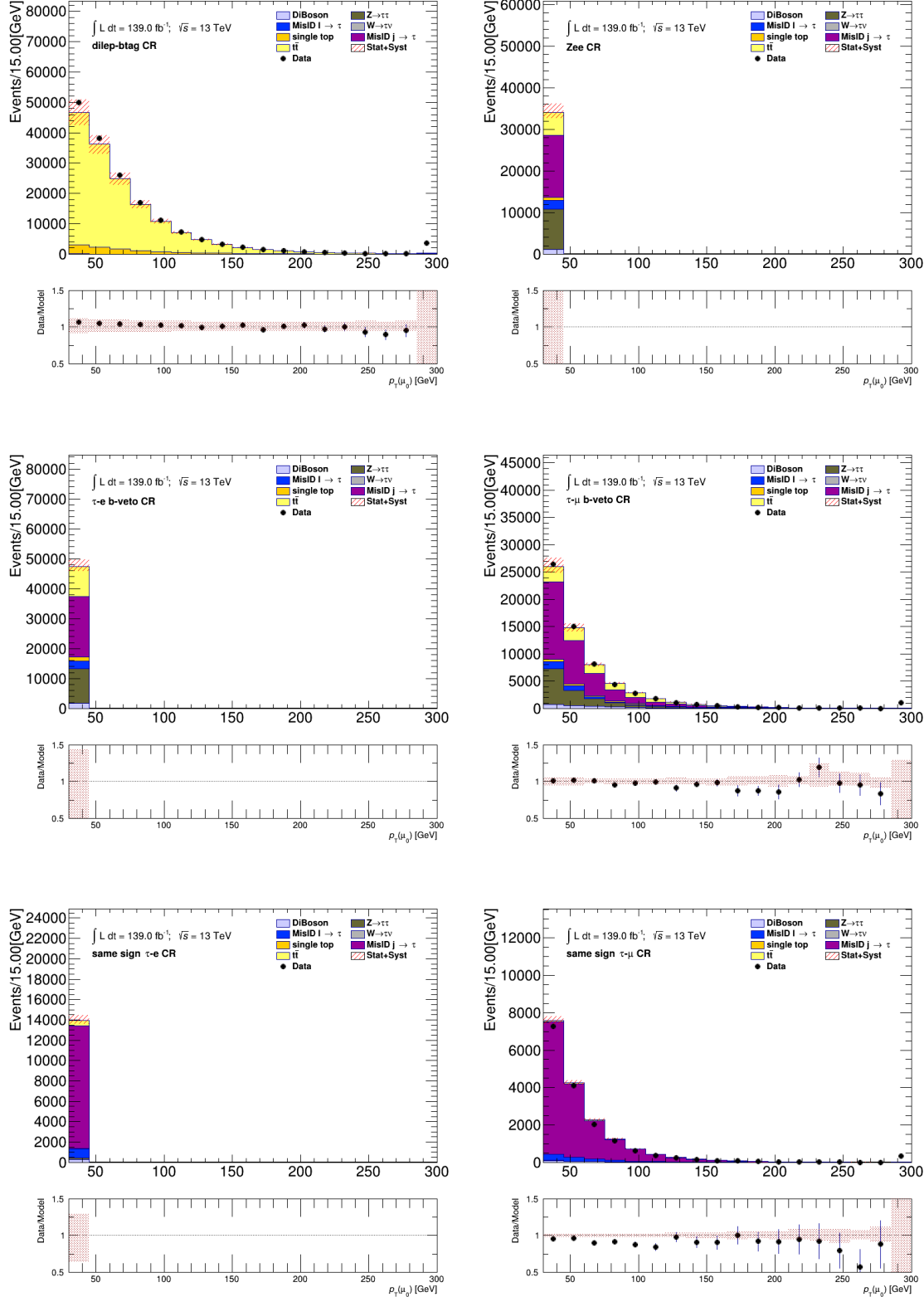


Figure C.19: Comparison between the predicted and the measured p_T^μ distributions in various control regions defined for the $\tau + \ell$ channel. The uncertainty band includes both statistical and systematic uncertainties on the background prediction.

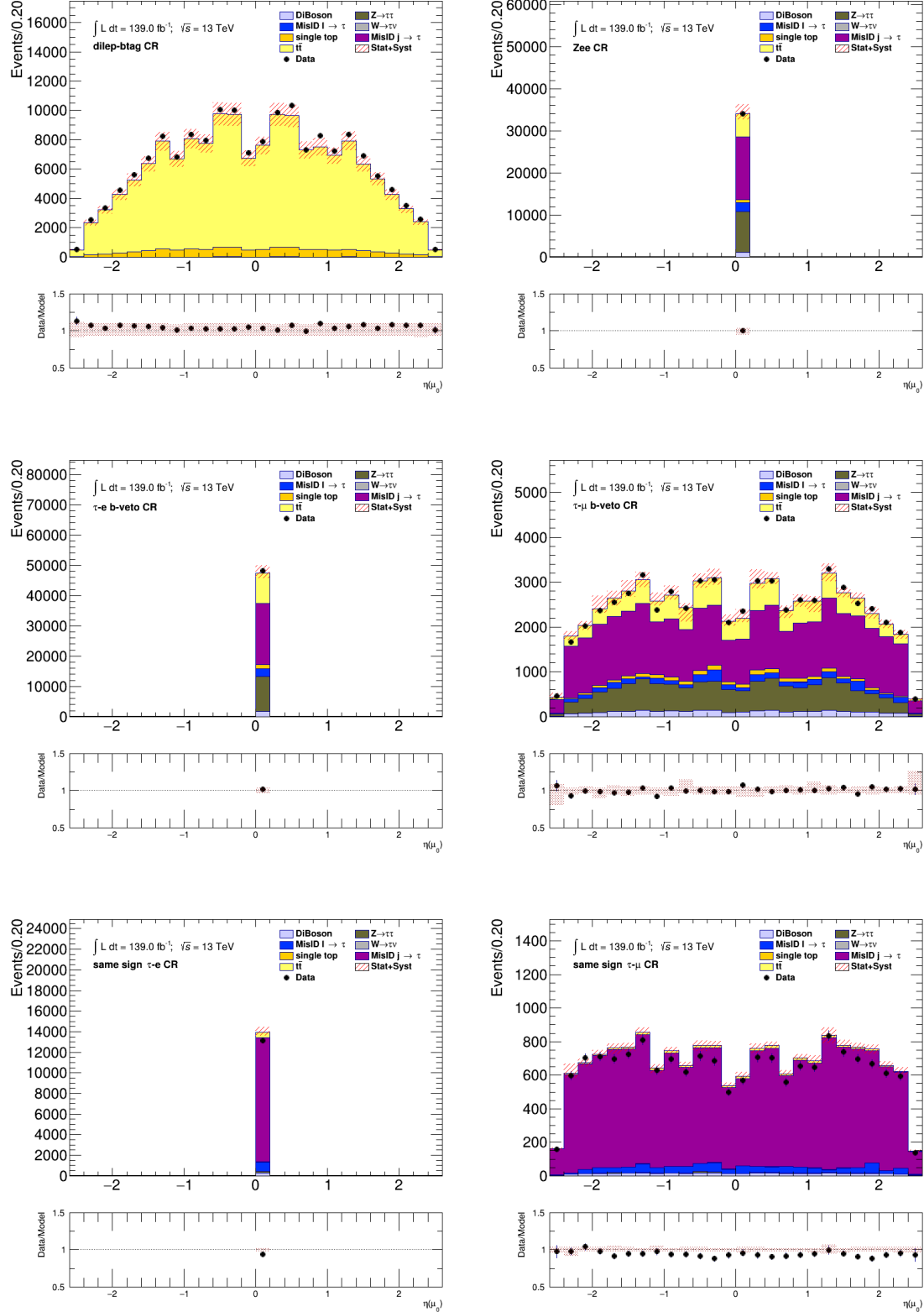


Figure C.20: Comparison between the predicted and the measured η^μ distributions in various control regions defined for the $\tau + \ell$ channel. The uncertainty band includes both statistical and systematic uncertainties on the background prediction.

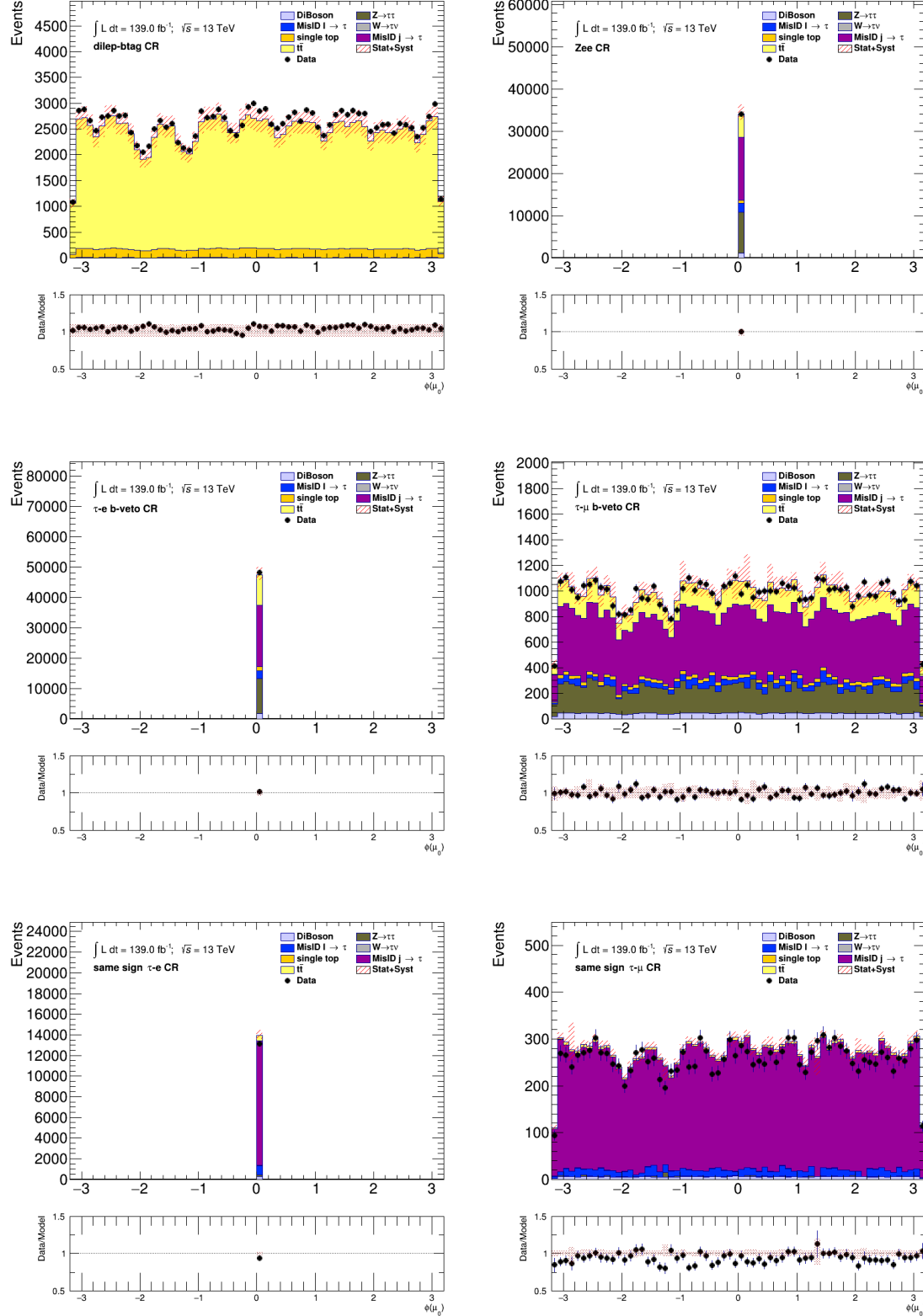


Figure C.21: Comparison between the predicted and the measured ϕ^μ distributions in various control regions defined for the $\tau + \ell$ channel. The uncertainty band includes both statistical and systematic uncertainties on the background prediction.

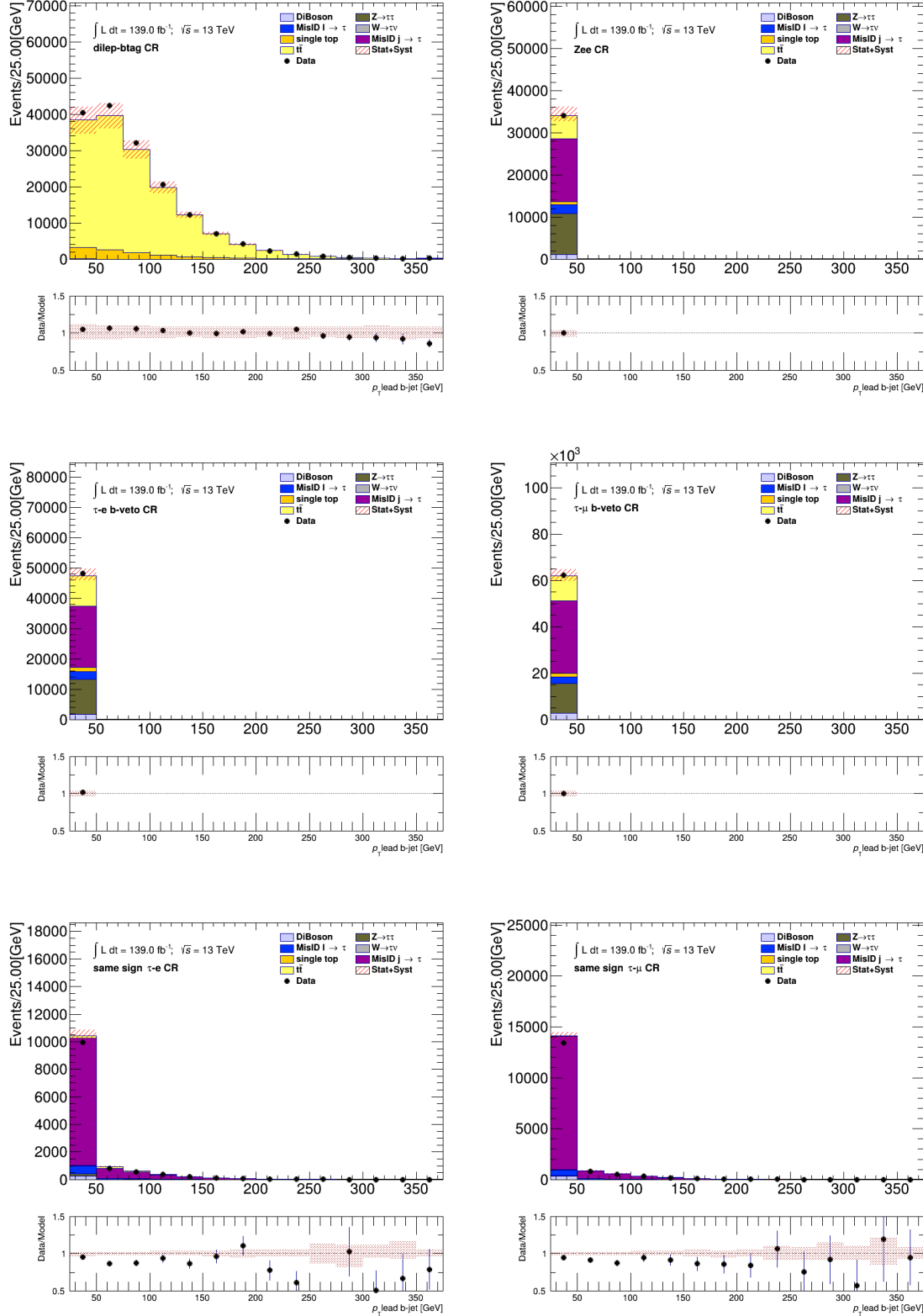


Figure C.22: Comparison between the predicted and the measured p_T^{b-jet} distributions in various control regions defined for the $\tau + \ell$ channel. The uncertainty band includes both statistical and systematic uncertainties on the background prediction.

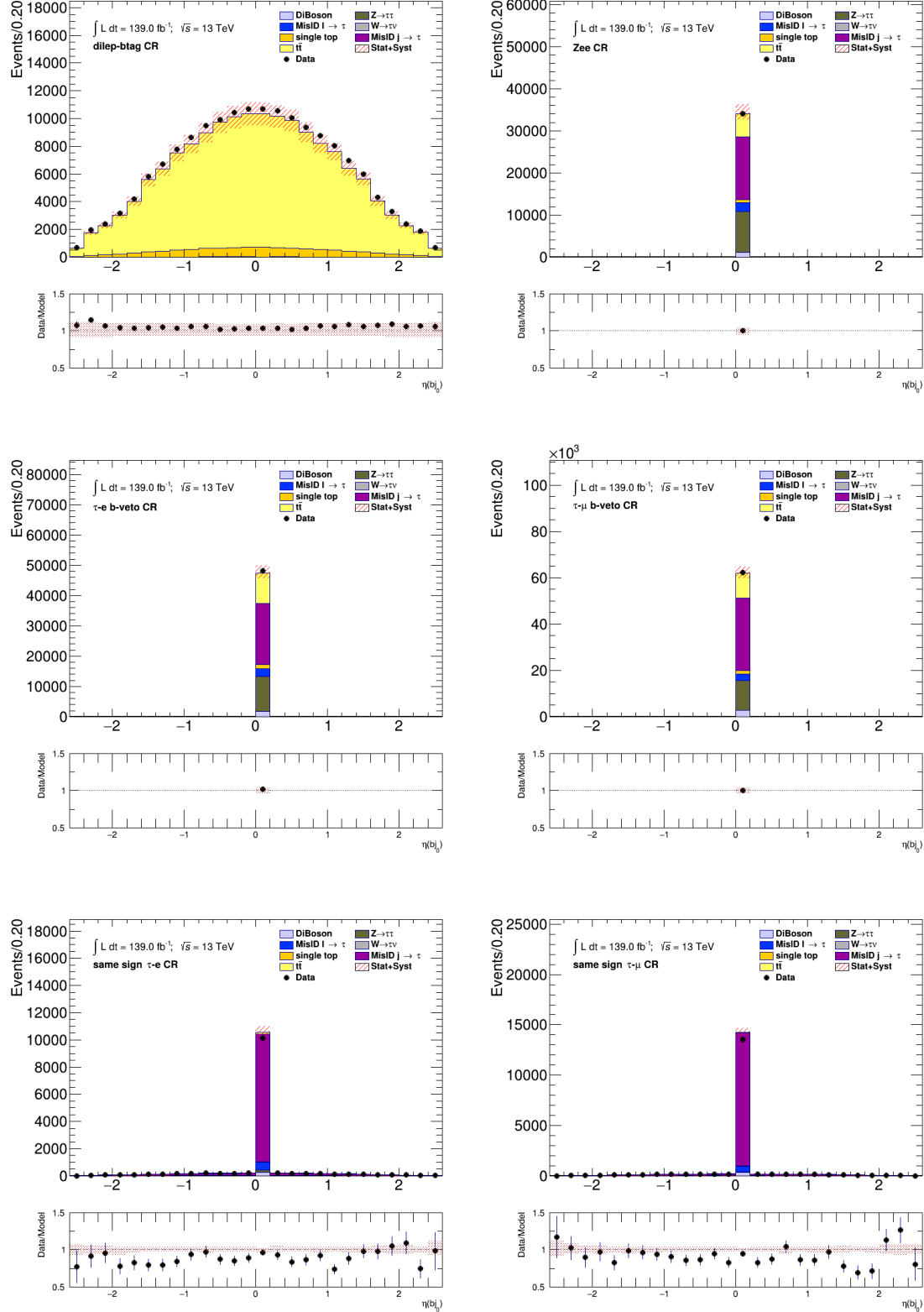


Figure C.23: Comparison between the predicted and the measured η^{b-jet} distributions in various control regions defined for the $\tau + \ell$ channel. The uncertainty band includes both statistical and systematic uncertainties on the background prediction.

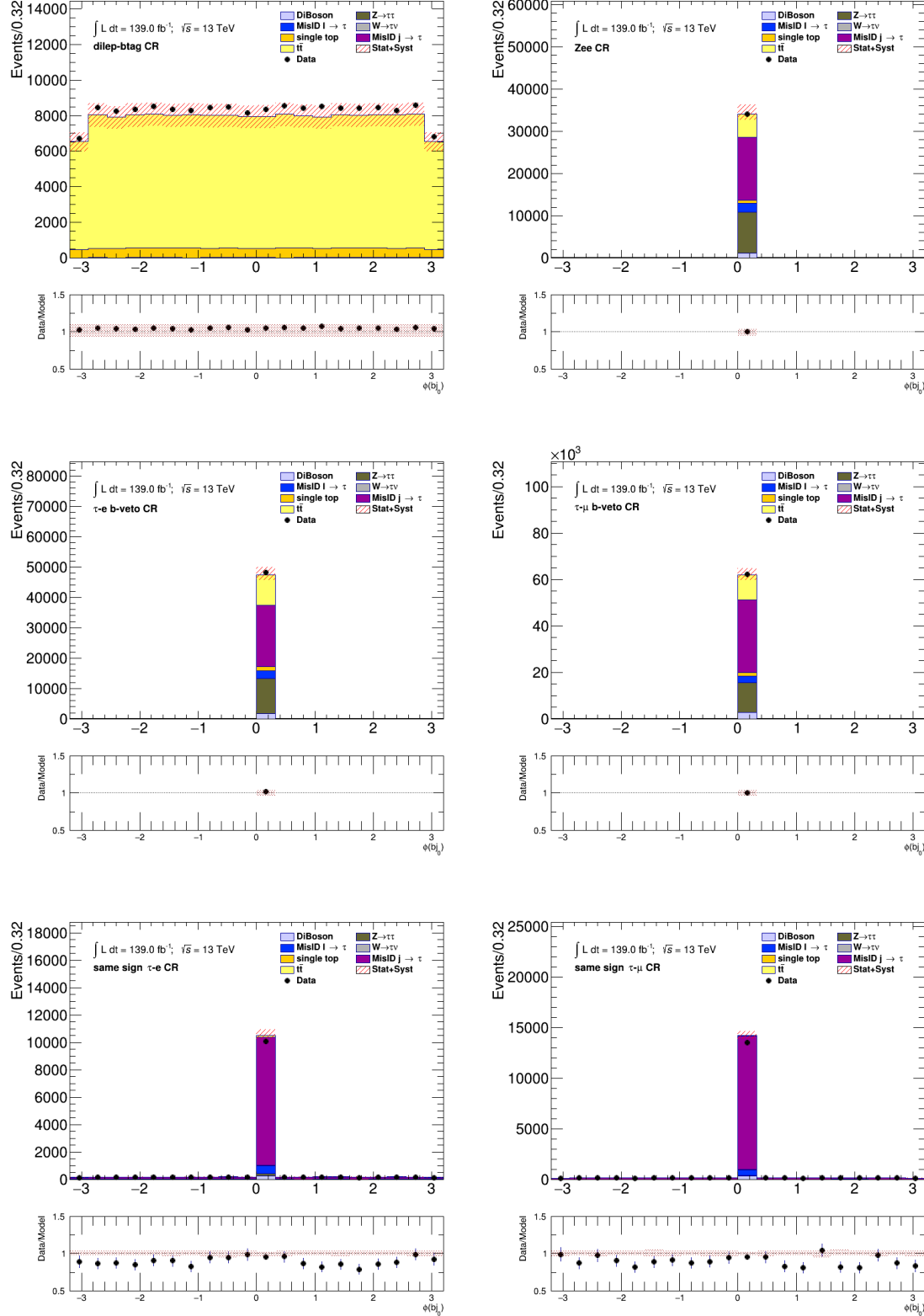


Figure C.24: Comparison between the predicted and the measured ϕ^{b-jet} distributions in various control regions defined for the $\tau + \ell$ channel. The uncertainty band includes both statistical and systematic uncertainties on the background prediction.

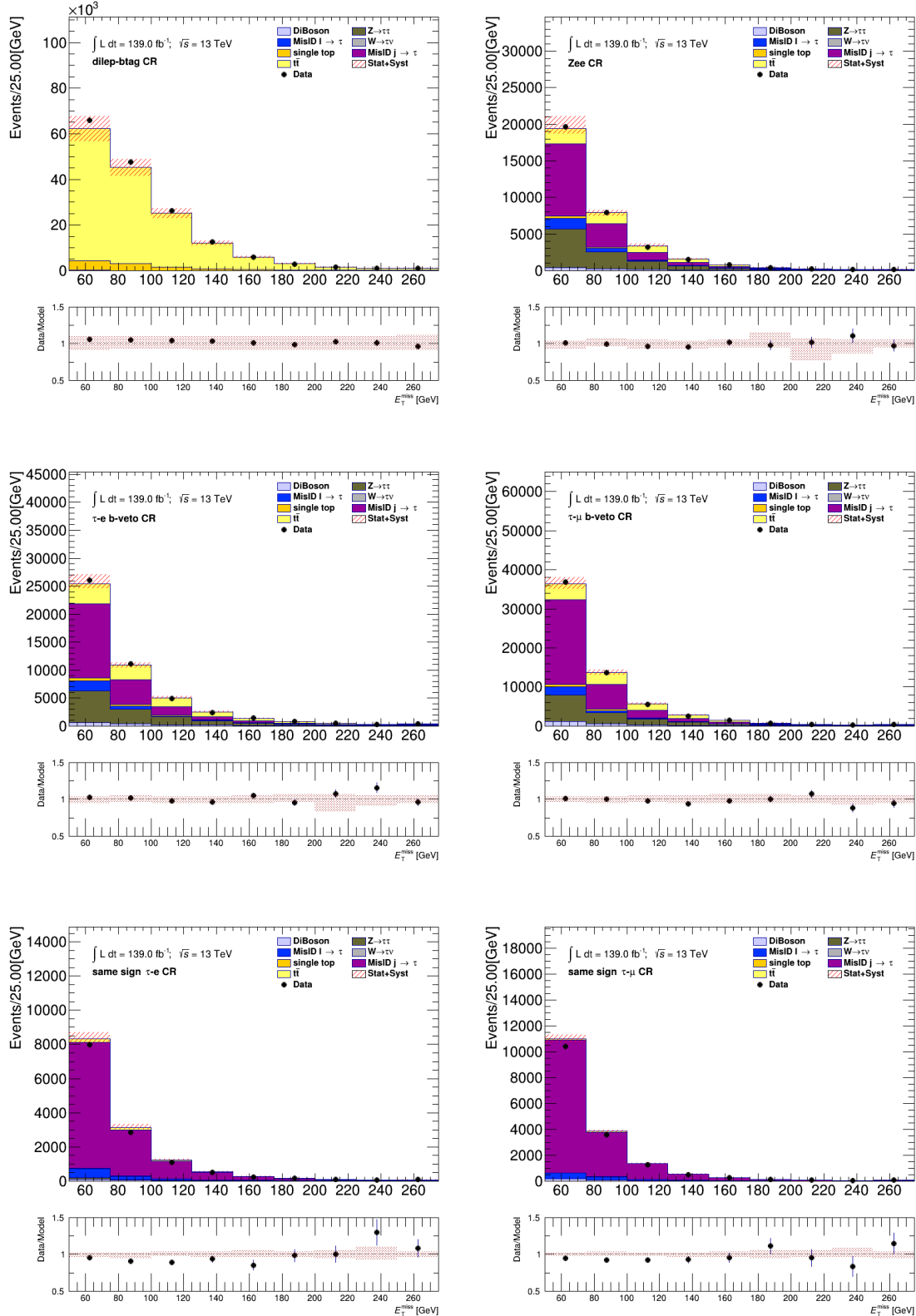


Figure C.25: Comparison between the predicted and the measured E_T^{miss} distributions in various control regions defined for the $\tau + \ell$ channel. The uncertainty band includes both statistical and systematic uncertainties on the background prediction.

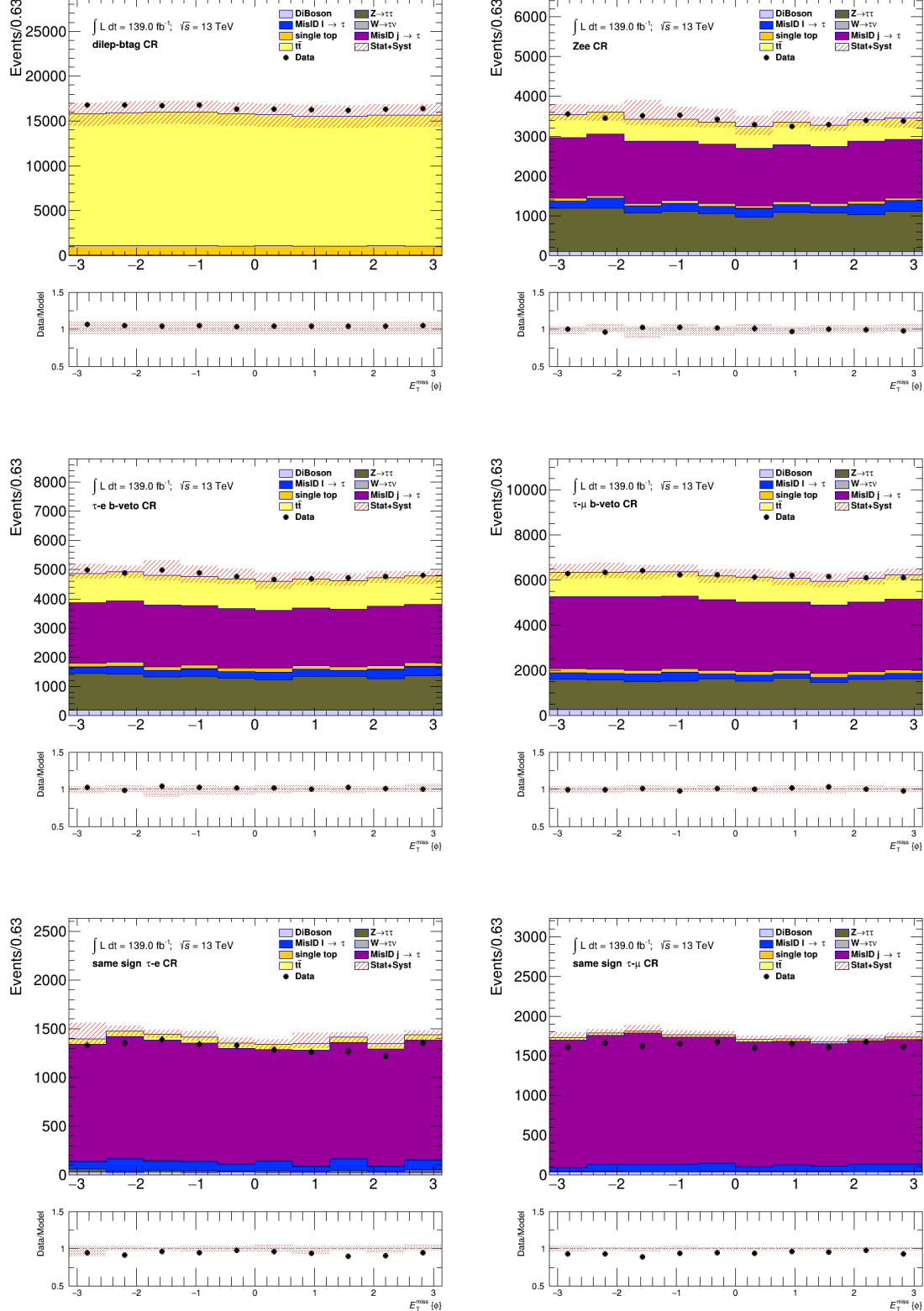


Figure C.26: Comparison between the predicted and the measured $\phi_{E_T}^{\text{miss}}$ distributions in various control regions defined for the $\tau + \ell$ channel. The uncertainty band includes both statistical and systematic uncertainties on the background prediction.

C.3 $\tau + \text{jets}$ Signal Region Plots

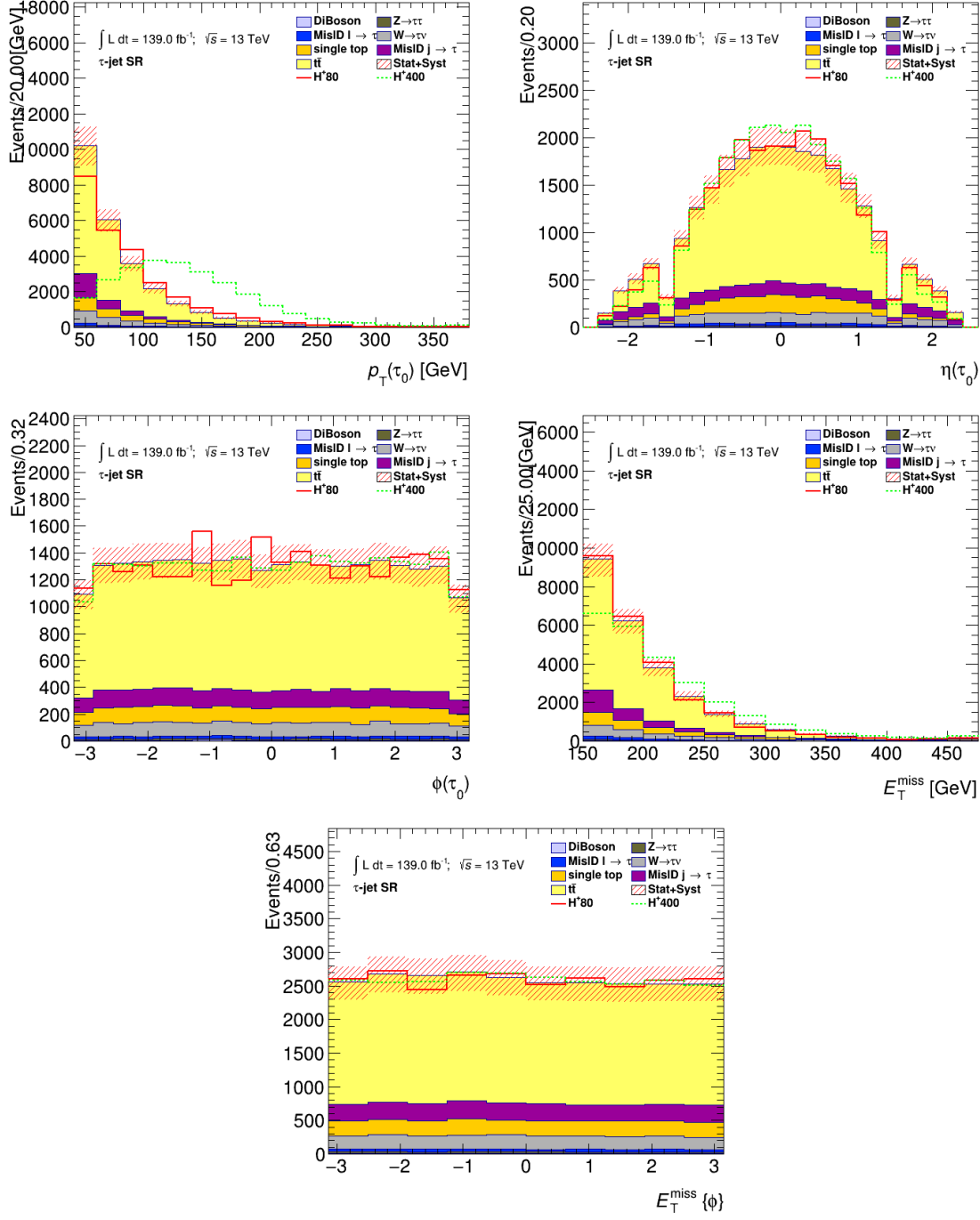


Figure C.27: PNN input variable distributions in $\tau + \text{jets}$ signal region. The uncertainty band includes both statistical and systematic uncertainties on the background prediction.

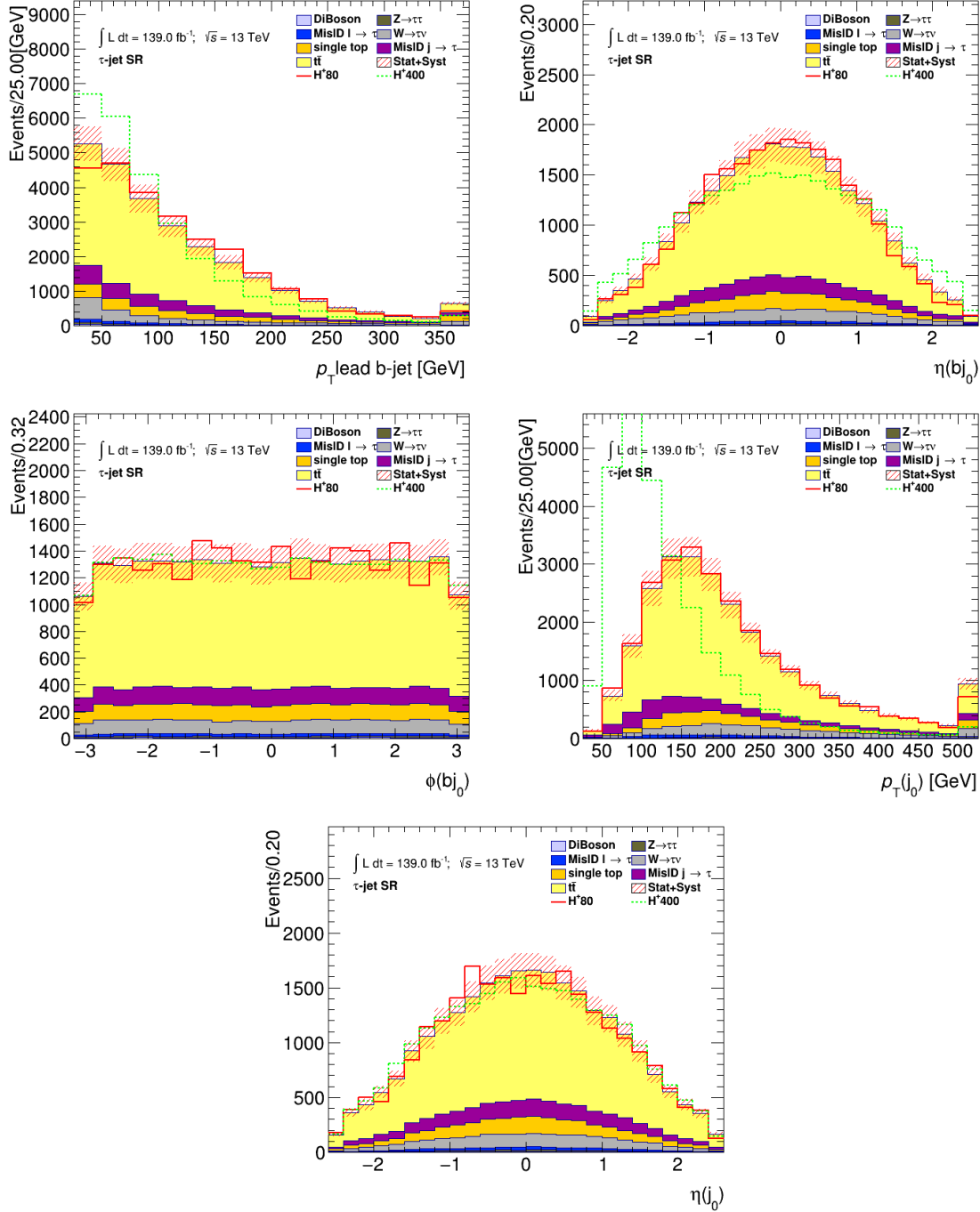


Figure C.28: PNN input variable distributions in $\tau + \text{jets}$ signal region. The uncertainty band includes both statistical and systematic uncertainties on the background prediction.

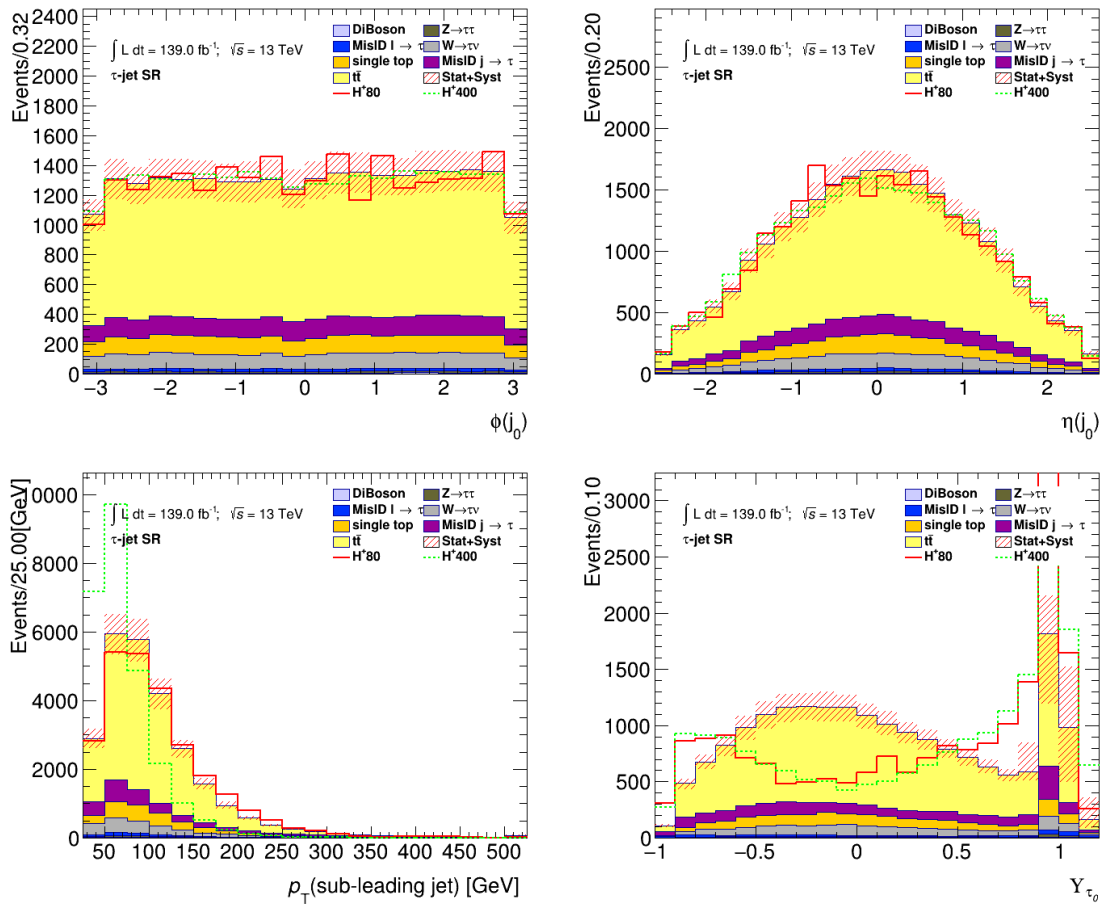


Figure C.29: PNN input variable distributions in $\tau + \text{jets}$ signal region. The uncertainty band includes both statistical and systematic uncertainties on the background prediction.

C.4 $\tau + \ell$ Signal Region Plots

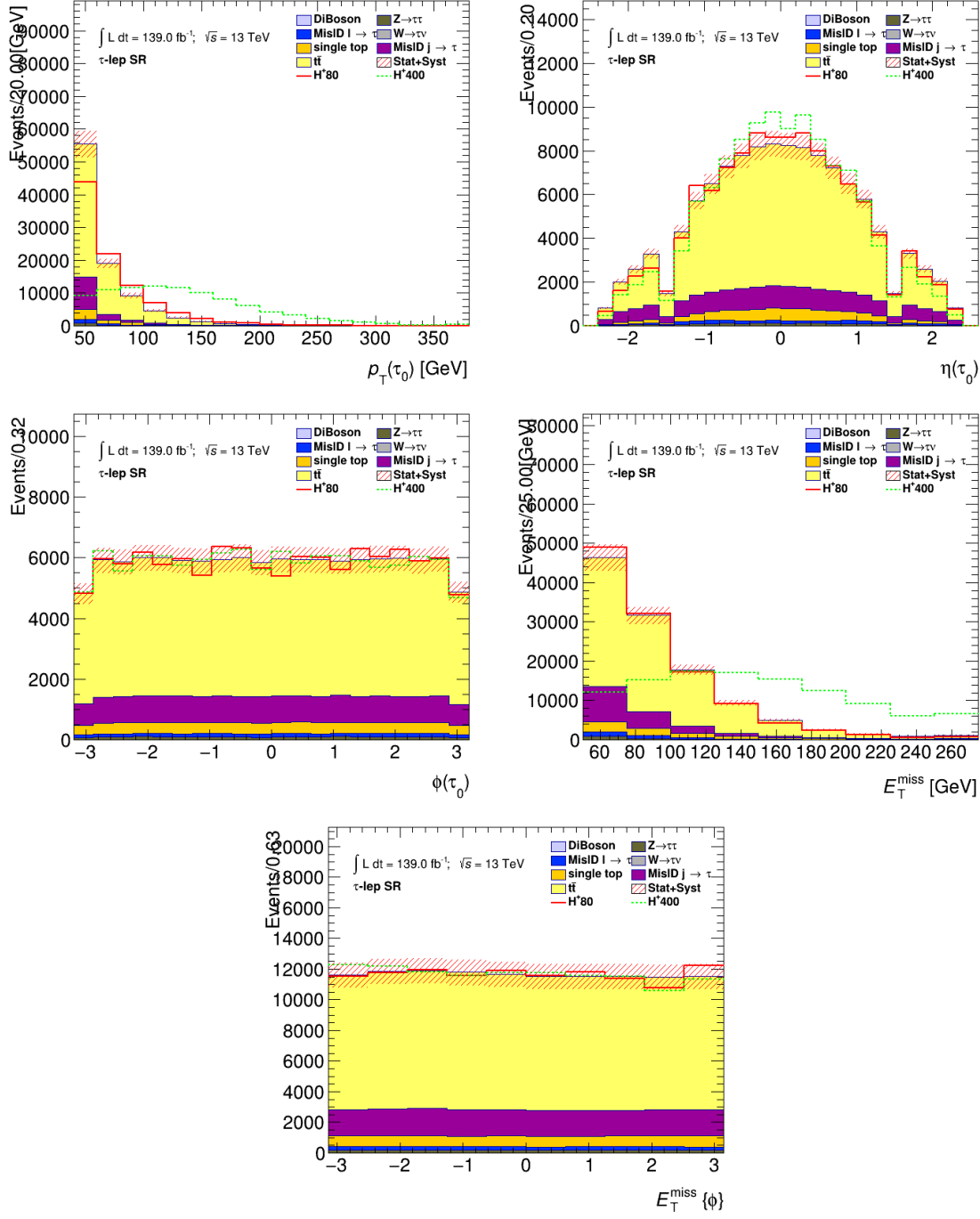


Figure C.30: PNN input variable distributions in $\tau + \ell$ signal region. The uncertainty band includes both statistical and systematic uncertainties on the background prediction.

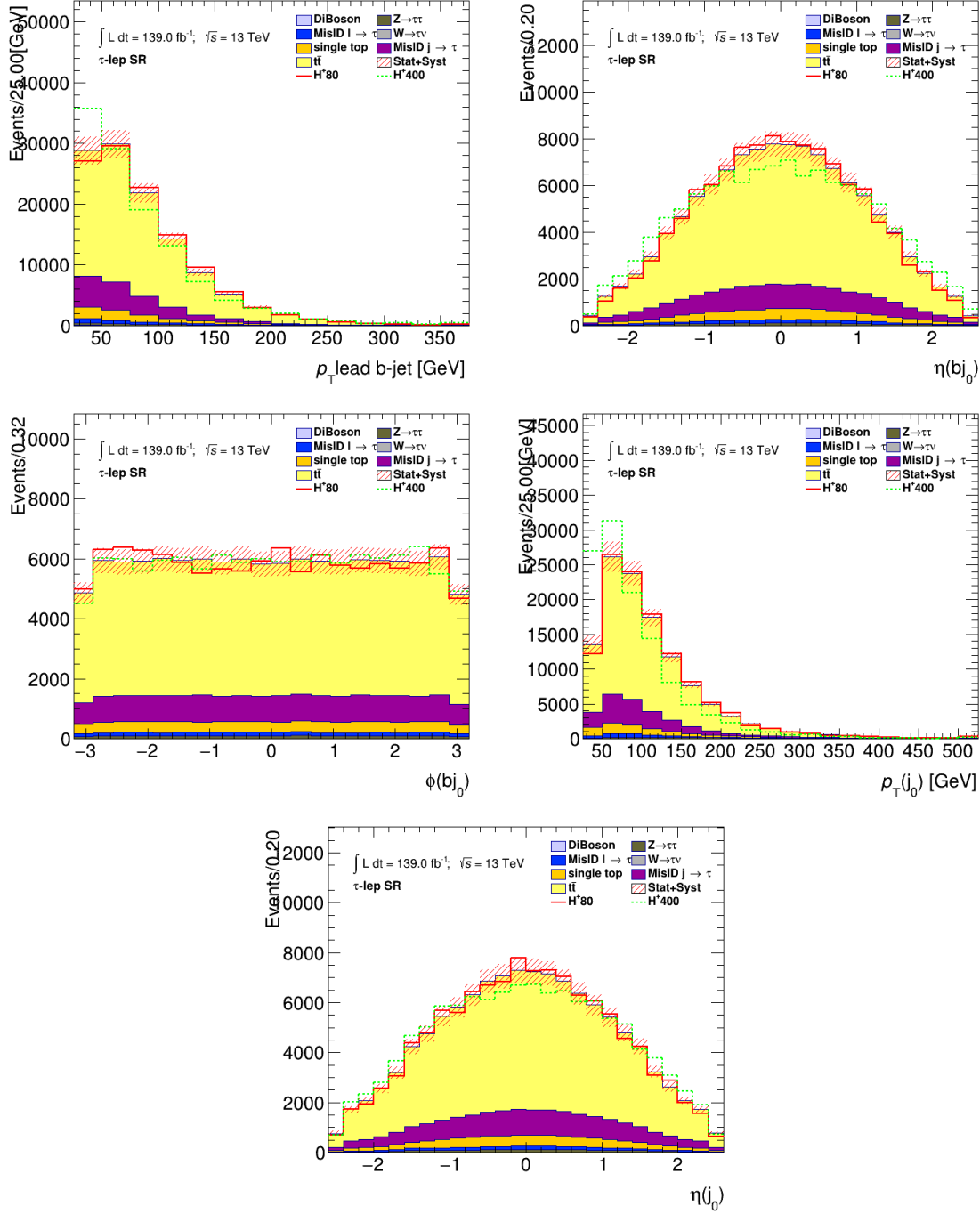


Figure C.31: PNN input variable distributions in $\tau + \ell$ signal region. The uncertainty band includes both statistical and systematic uncertainties on the background prediction.

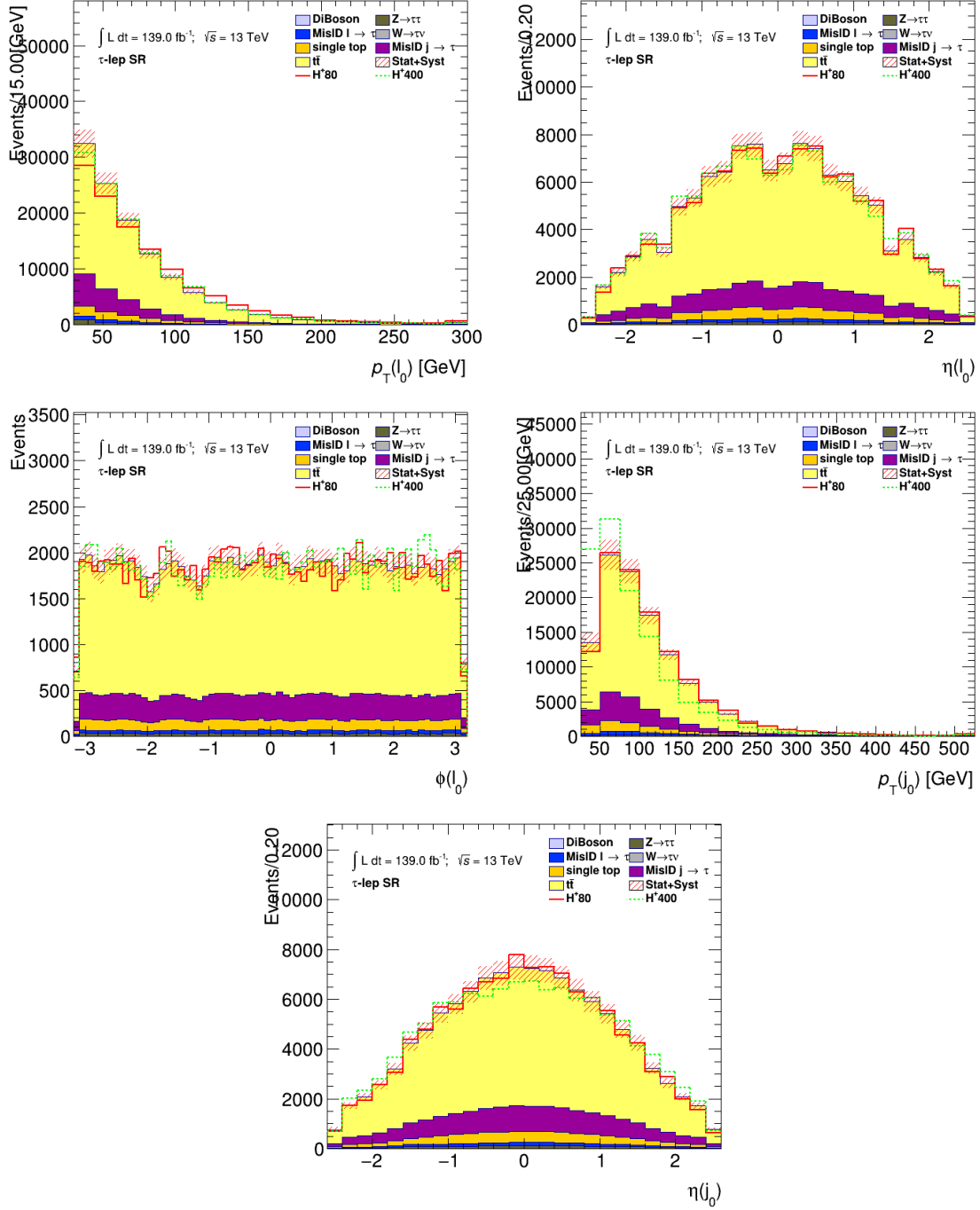


Figure C.32: PNN input variable distributions in $\tau + \ell$ signal region. The uncertainty band includes both statistical and systematic uncertainties on the background prediction.

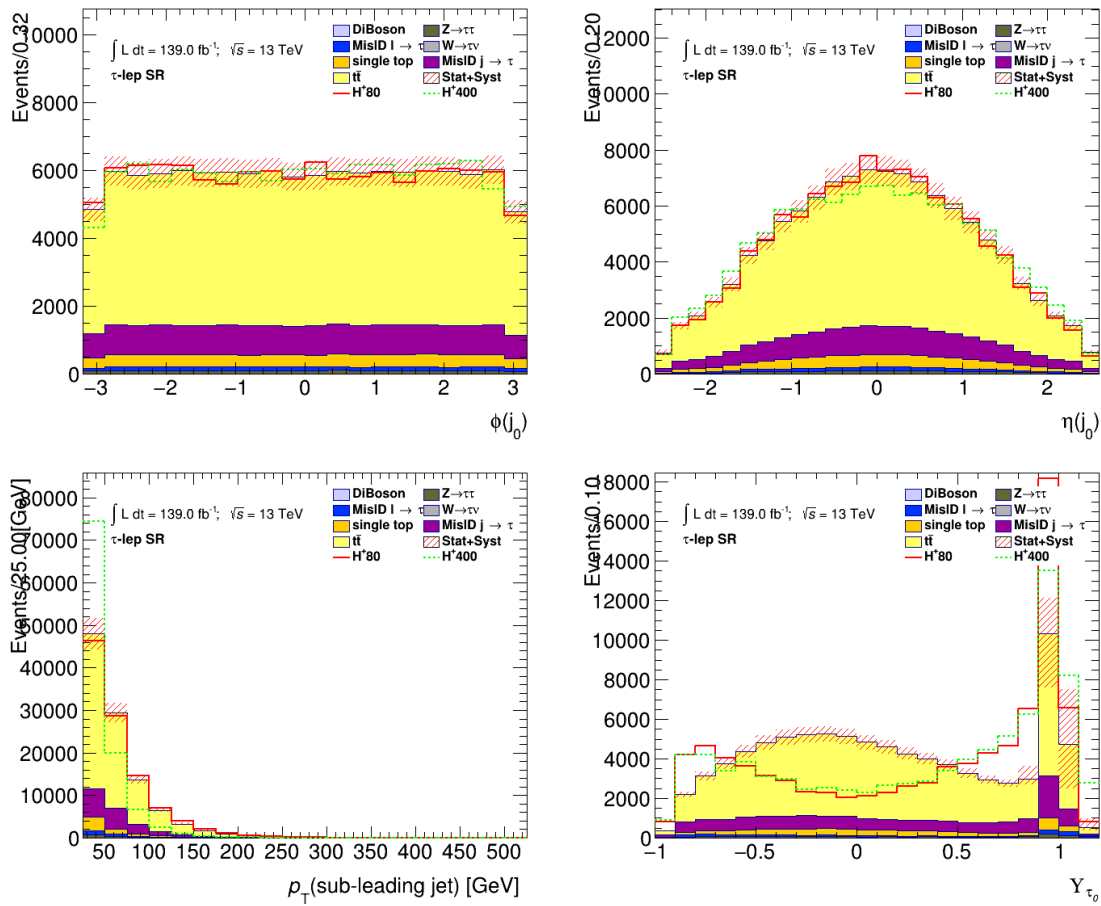


Figure C.33: PNN input variable distributions in $\tau + \ell$ signal region. The uncertainty band includes both statistical and systematic uncertainties on the background prediction.

APPENDIX D

ADDITIONAL PNN SCORE PLOTS

D.1 $\tau + \text{jets}$ PNN Scores

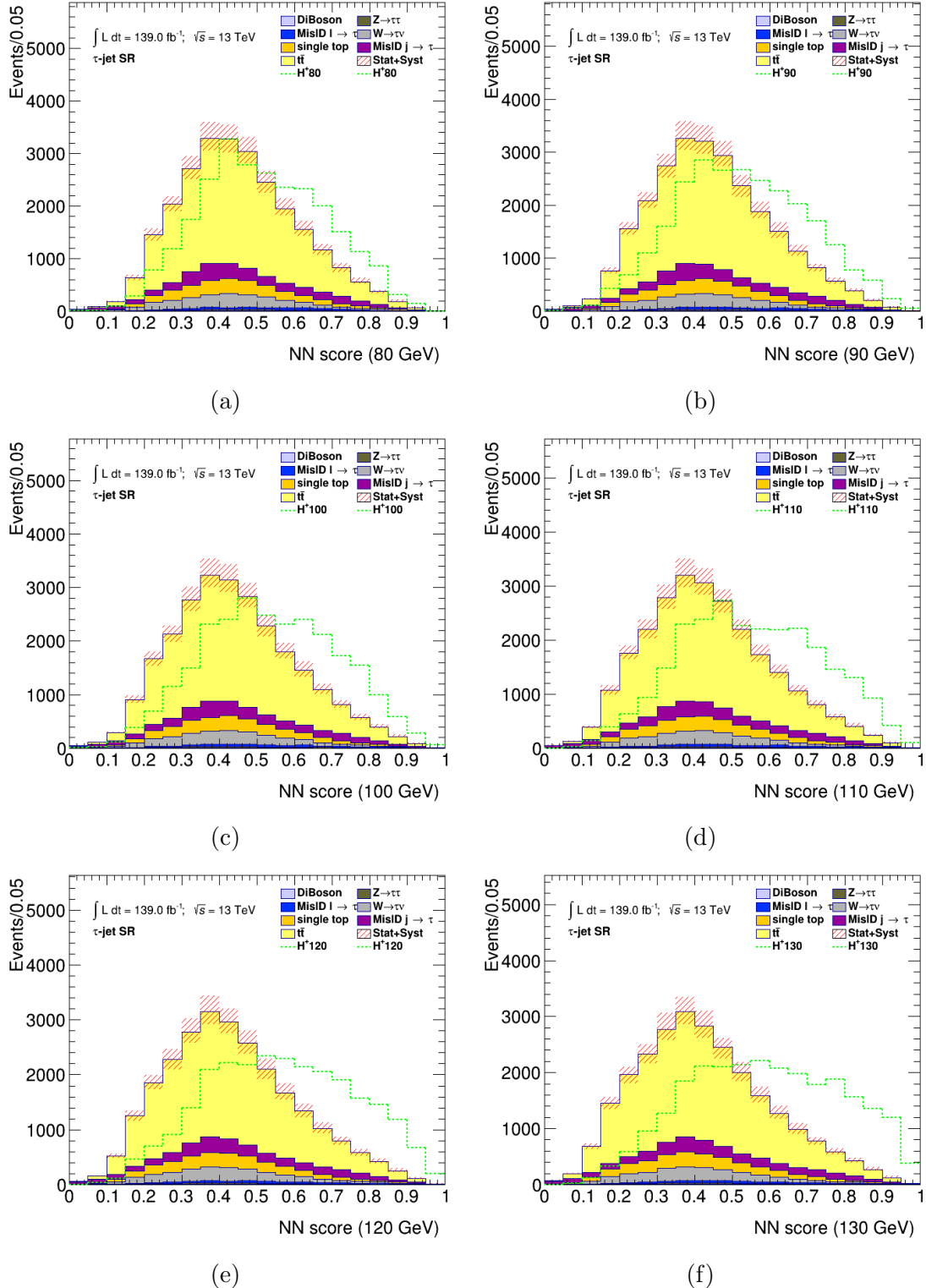


Figure D.1: PNN score distributions in the signal region of the τ +jets channel, for the six charged Higgs boson mass parameters. The uncertainty bands include all statistical and systematic uncertainties. The normalization of the signal (shown for illustration) corresponds to the integral of the background.

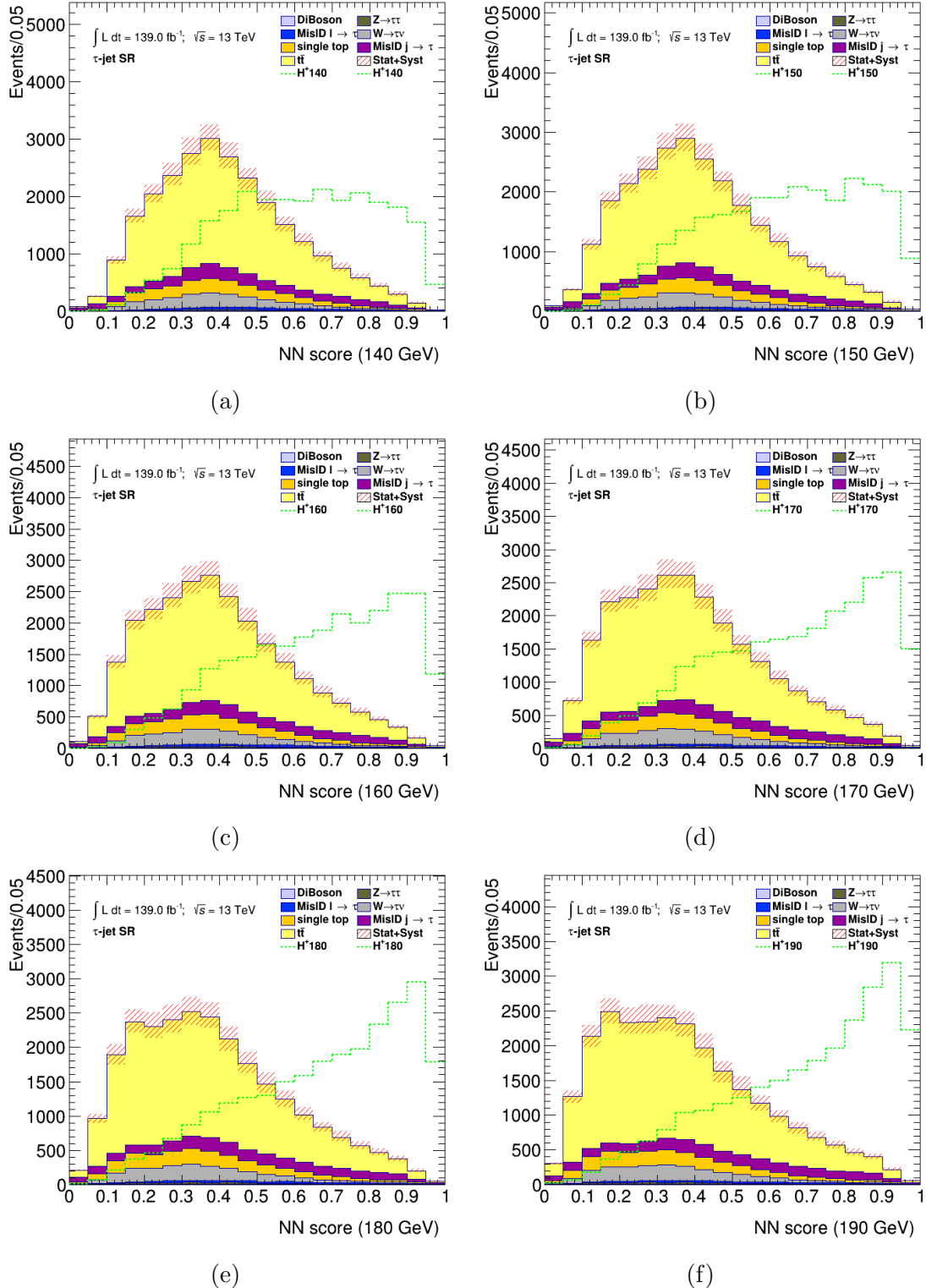


Figure D.2: PNN score distributions in the signal region of the $\tau+\text{jets}$ channel, for the six charged Higgs boson mass parameters. The uncertainty bands include all statistical and systematic uncertainties. The normalization of the signal (shown for illustration) corresponds to the integral of the background.

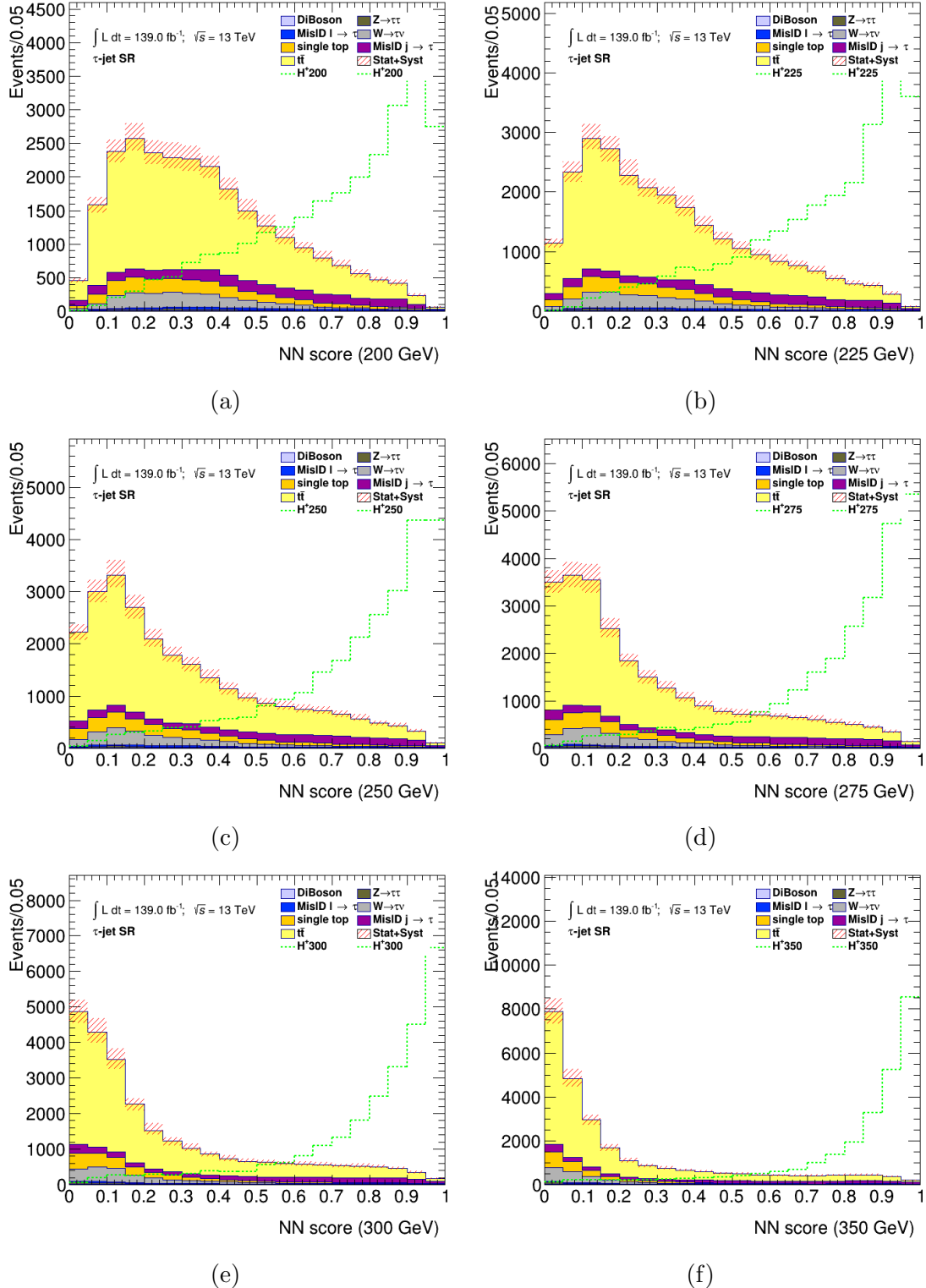


Figure D.3: PNN score distributions in the signal region of the $\tau+\text{jets}$ channel, for the six charged Higgs boson mass parameters. The uncertainty bands include all statistical and systematic uncertainties. The normalization of the signal (shown for illustration) corresponds to the integral of the background.

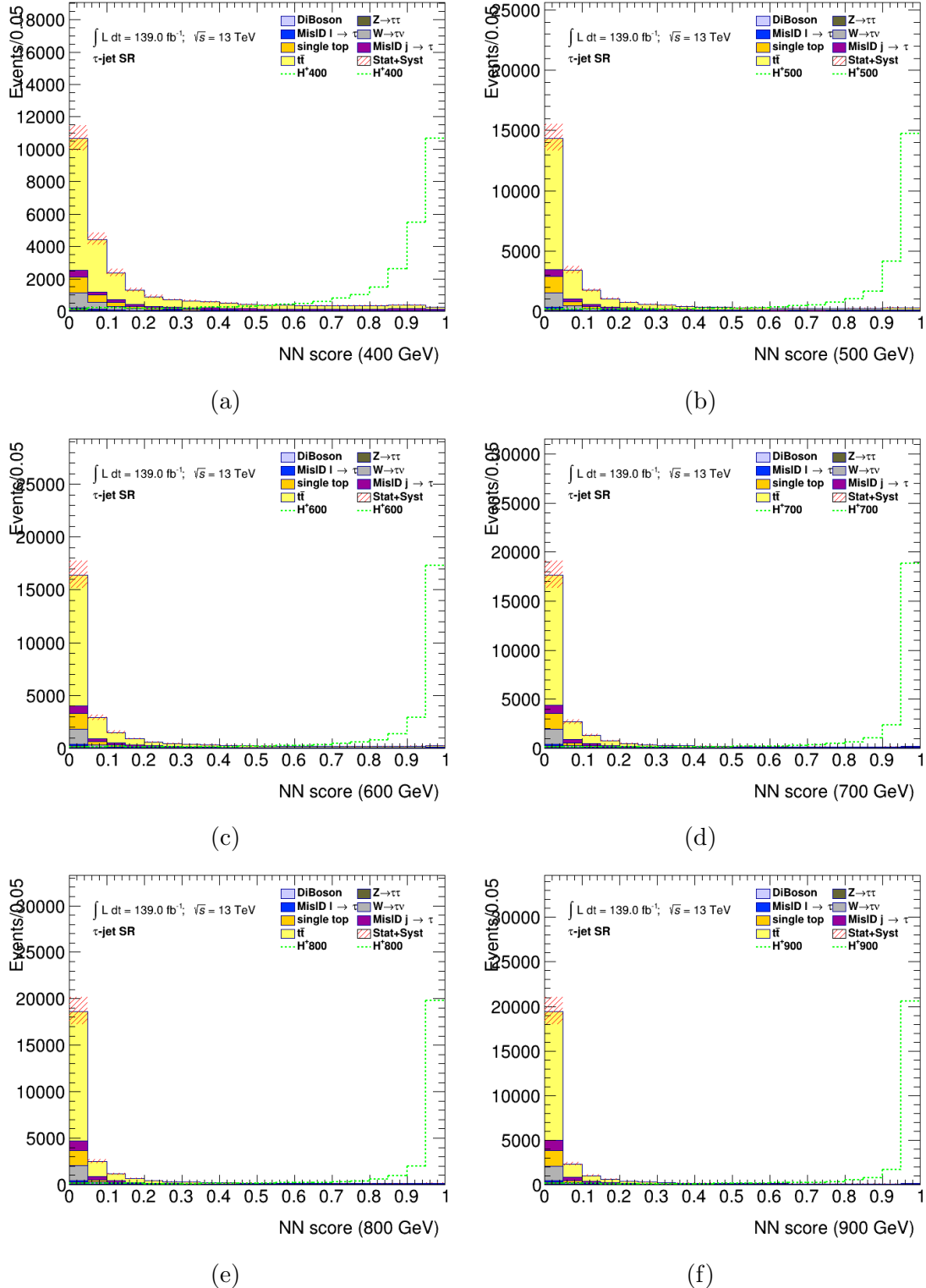


Figure D.4: PNN score distributions in the signal region of the $\tau+\text{jets}$ channel, for the six charged Higgs boson mass parameters. The uncertainty bands include all statistical and systematic uncertainties. The normalization of the signal (shown for illustration) corresponds to the integral of the background.

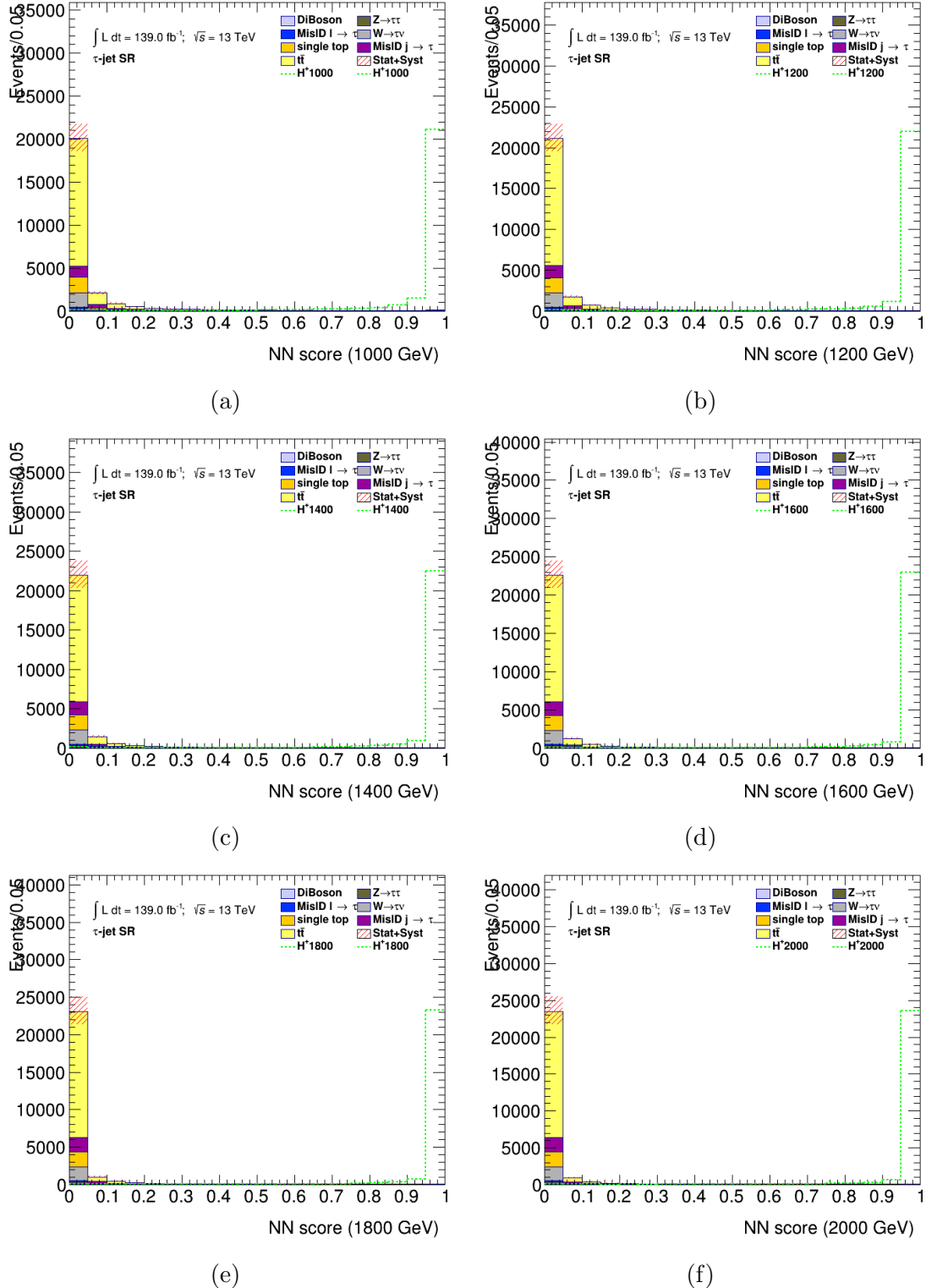


Figure D.5: PNN score distributions in the signal region of the τ +jets channel, for the six charged Higgs boson mass parameters. The uncertainty bands include all statistical and systematic uncertainties. The normalization of the signal (shown for illustration) corresponds to the integral of the background.

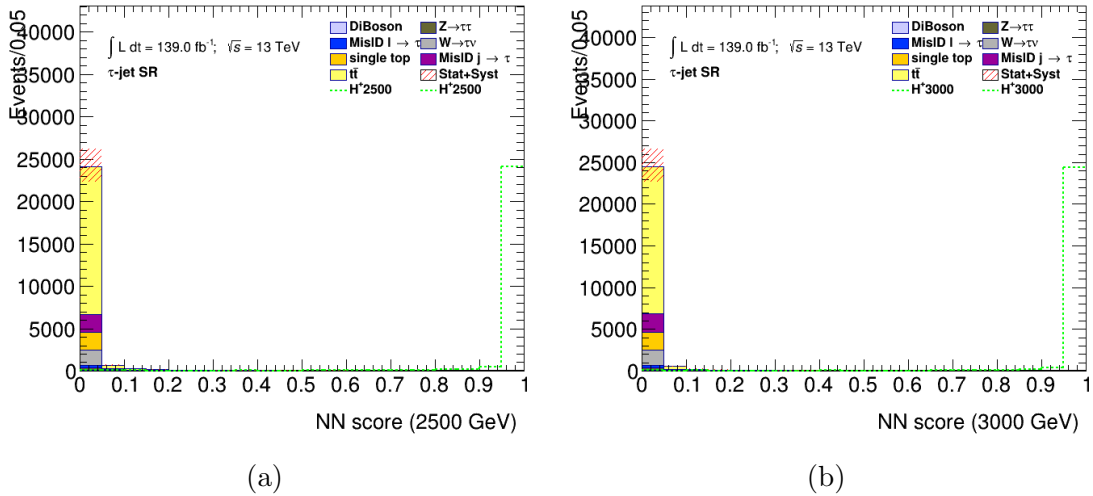


Figure D.6: PNN score distributions in the signal region of the $\tau+jets$ channel, for the six charged Higgs boson mass parameters. The uncertainty bands include all statistical and systematic uncertainties. The normalization of the signal (shown for illustration) corresponds to the integral of the background.

D.2 $\tau + \ell$ PNN Scores

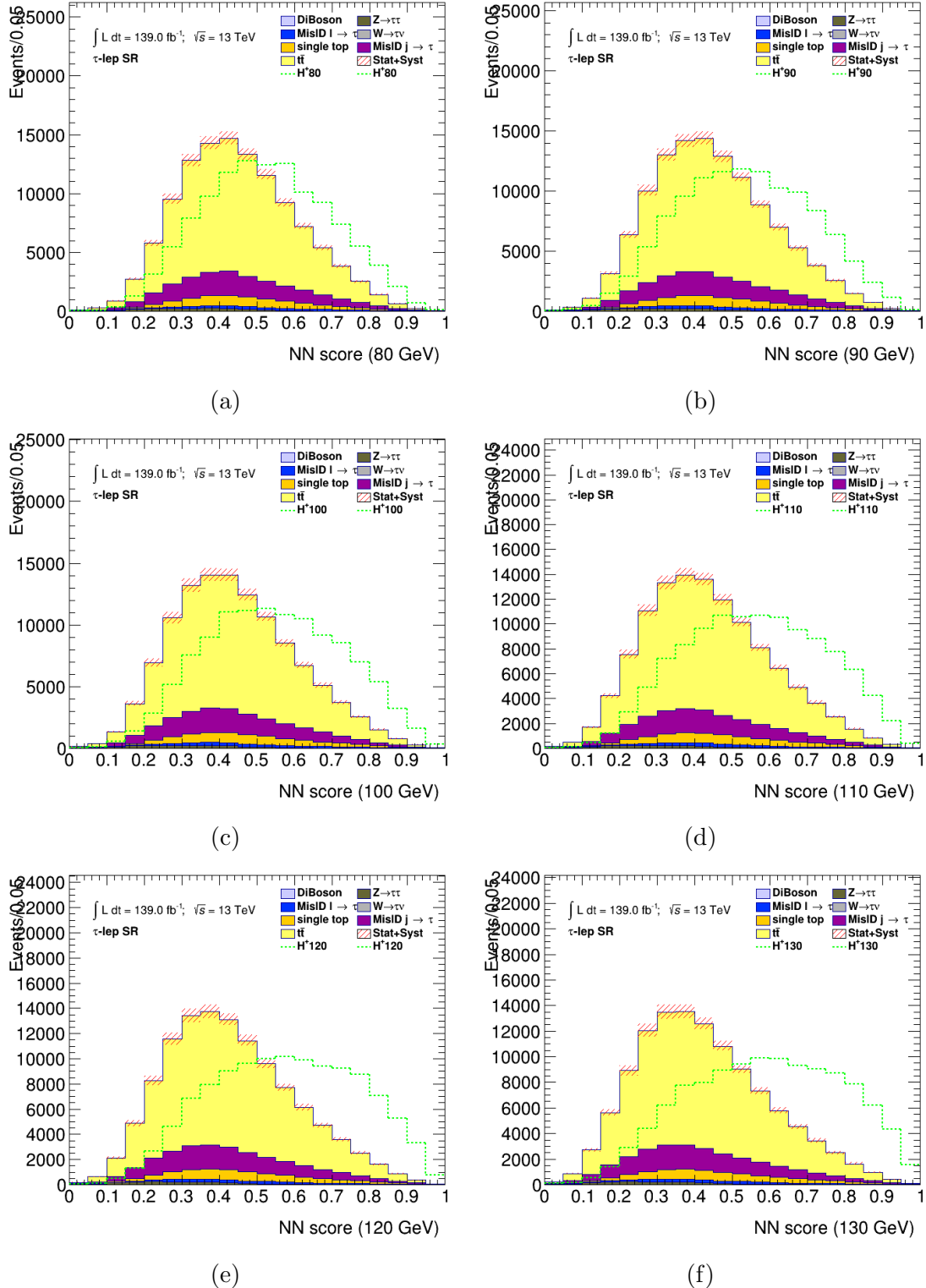


Figure D.7: PNN score distributions in the signal region of the $\tau + \ell$ channel, for the six charged Higgs boson mass parameters. The uncertainty bands include all statistical and systematic uncertainties. The normalization of the signal (shown for illustration) corresponds to the integral of the background.

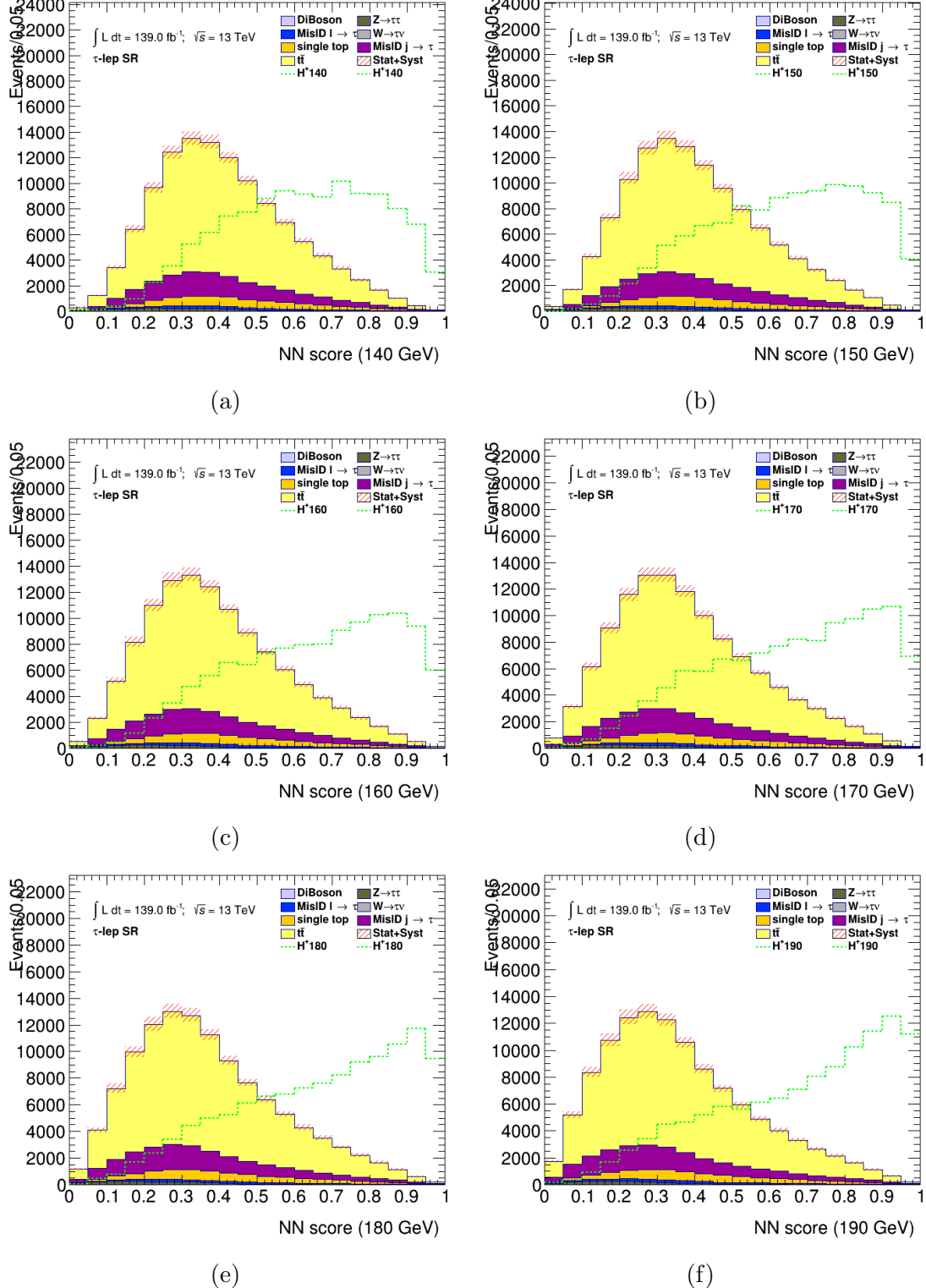


Figure D.8: PNN score distributions in the signal region of the $\tau + \ell$ channel, for the six charged Higgs boson mass parameters. The uncertainty bands include all statistical and systematic uncertainties. The normalization of the signal (shown for illustration) corresponds to the integral of the background.

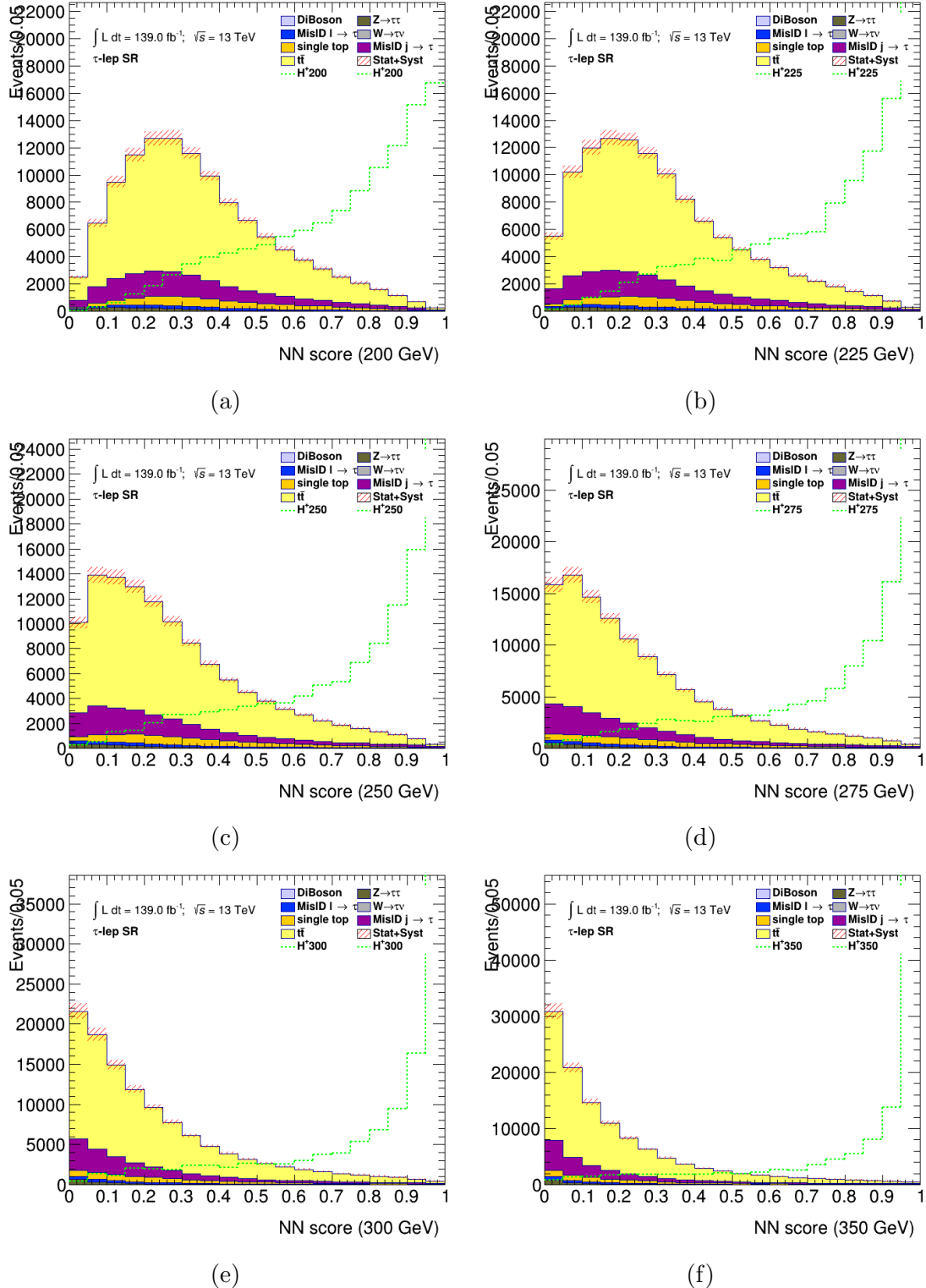


Figure D.9: PNN score distributions in the signal region of the $\tau + \ell$ channel, for the six charged Higgs boson mass parameters. The uncertainty bands include all statistical and systematic uncertainties. The normalization of the signal (shown for illustration) corresponds to the integral of the background.

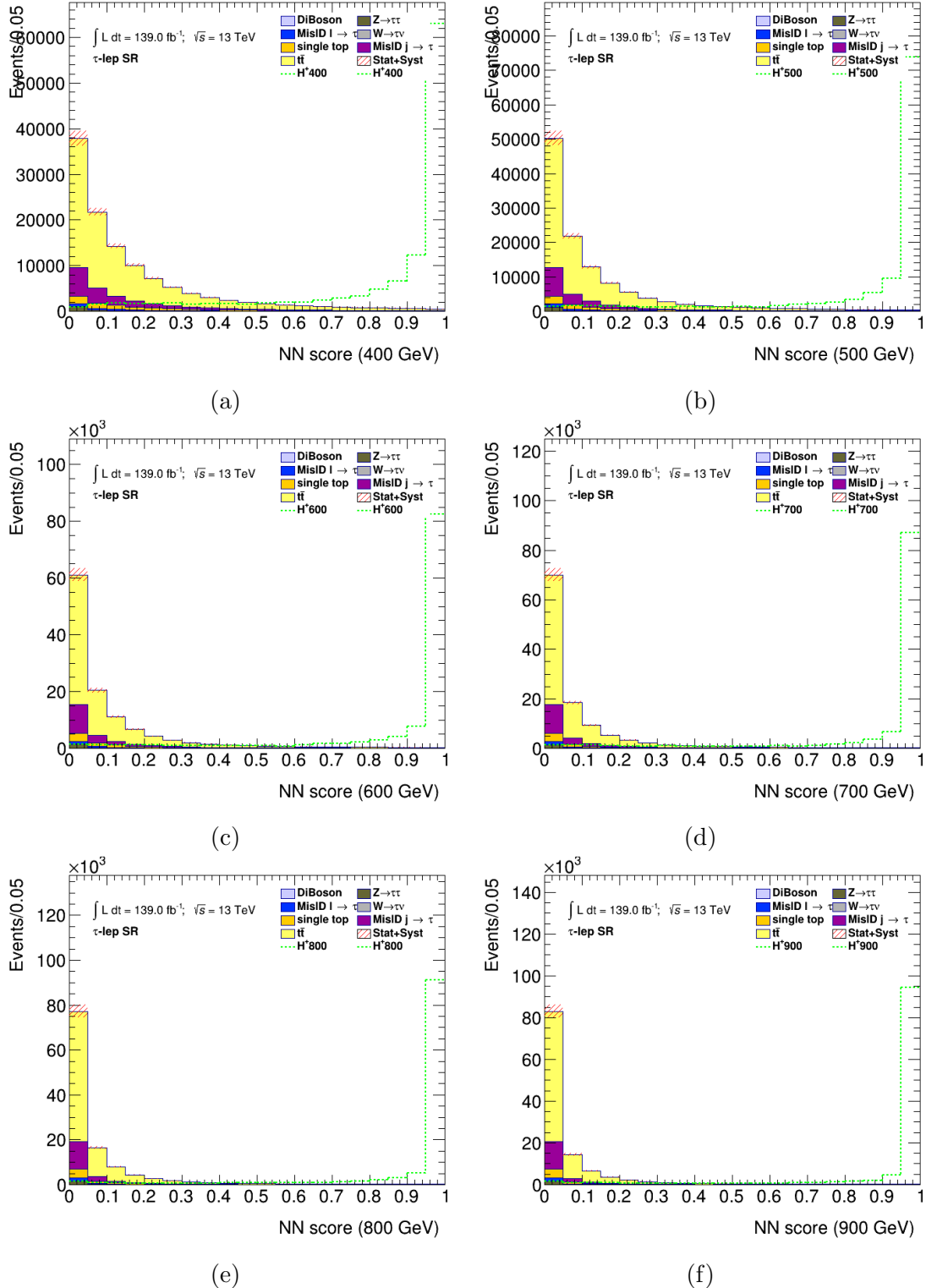


Figure D.10: PNN score distributions in the signal region of the $\tau + \ell$ channel, for the six charged Higgs boson mass parameters. The uncertainty bands include all statistical and systematic uncertainties. The normalization of the signal (shown for illustration) corresponds to the integral of the background.

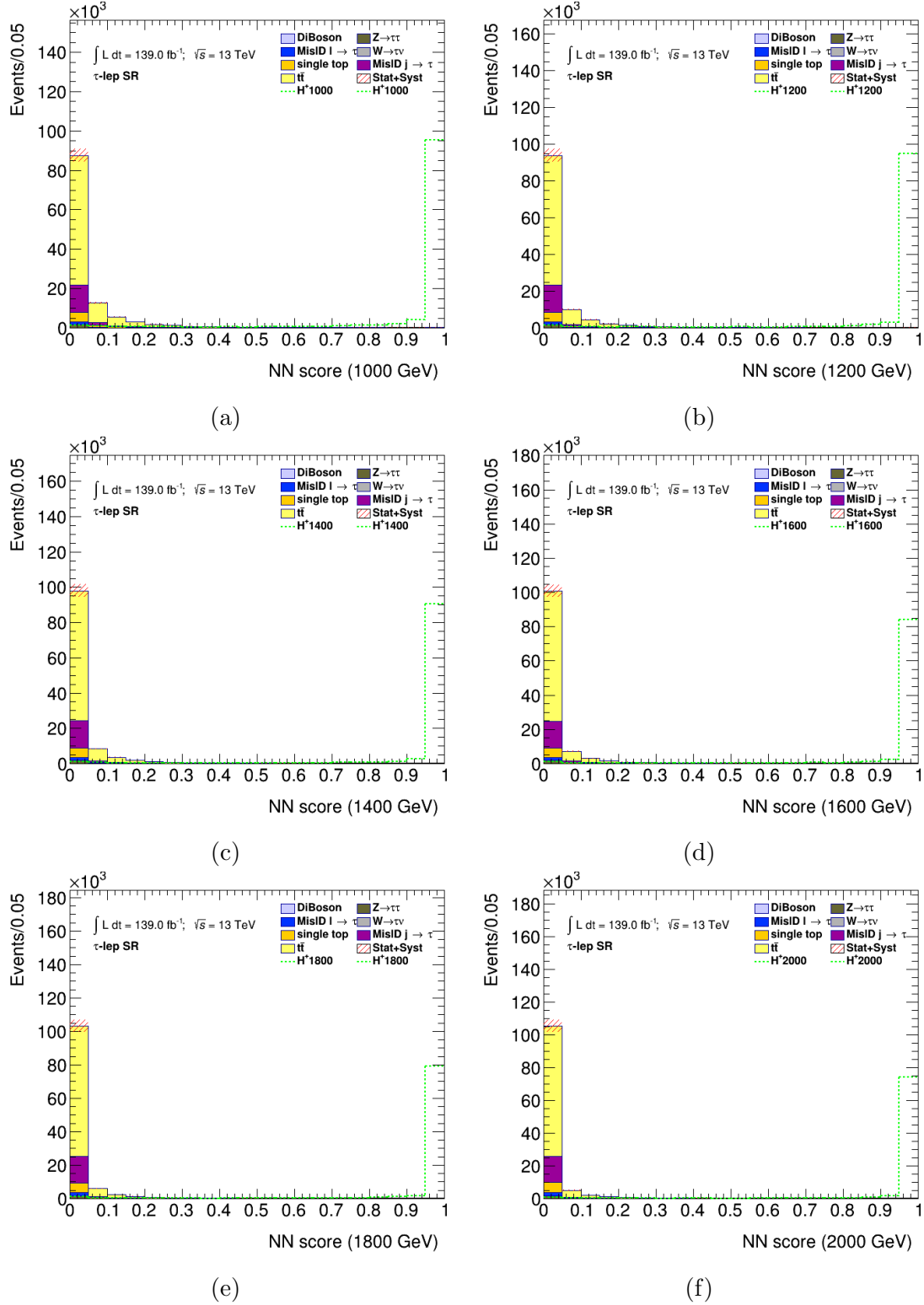


Figure D.11: PNN score distributions in the signal region of the $\tau + \ell$ channel, for the six charged Higgs boson mass parameters. The uncertainty bands include all statistical and systematic uncertainties. The normalization of the signal (shown for illustration) corresponds to the integral of the background.

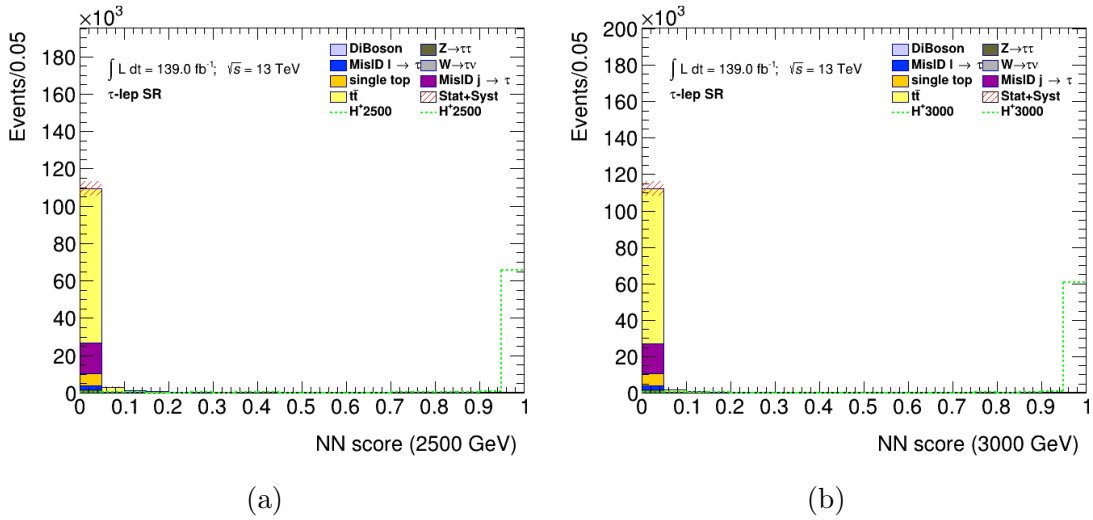


Figure D.12: PNN score distributions in the signal region of the $\tau + \ell$ channel, for the six charged Higgs boson mass parameters. The uncertainty bands include all statistical and systematic uncertainties. The normalization of the signal (shown for illustration) corresponds to the integral of the background.

D.3 $\tau + e$ PNN Scores

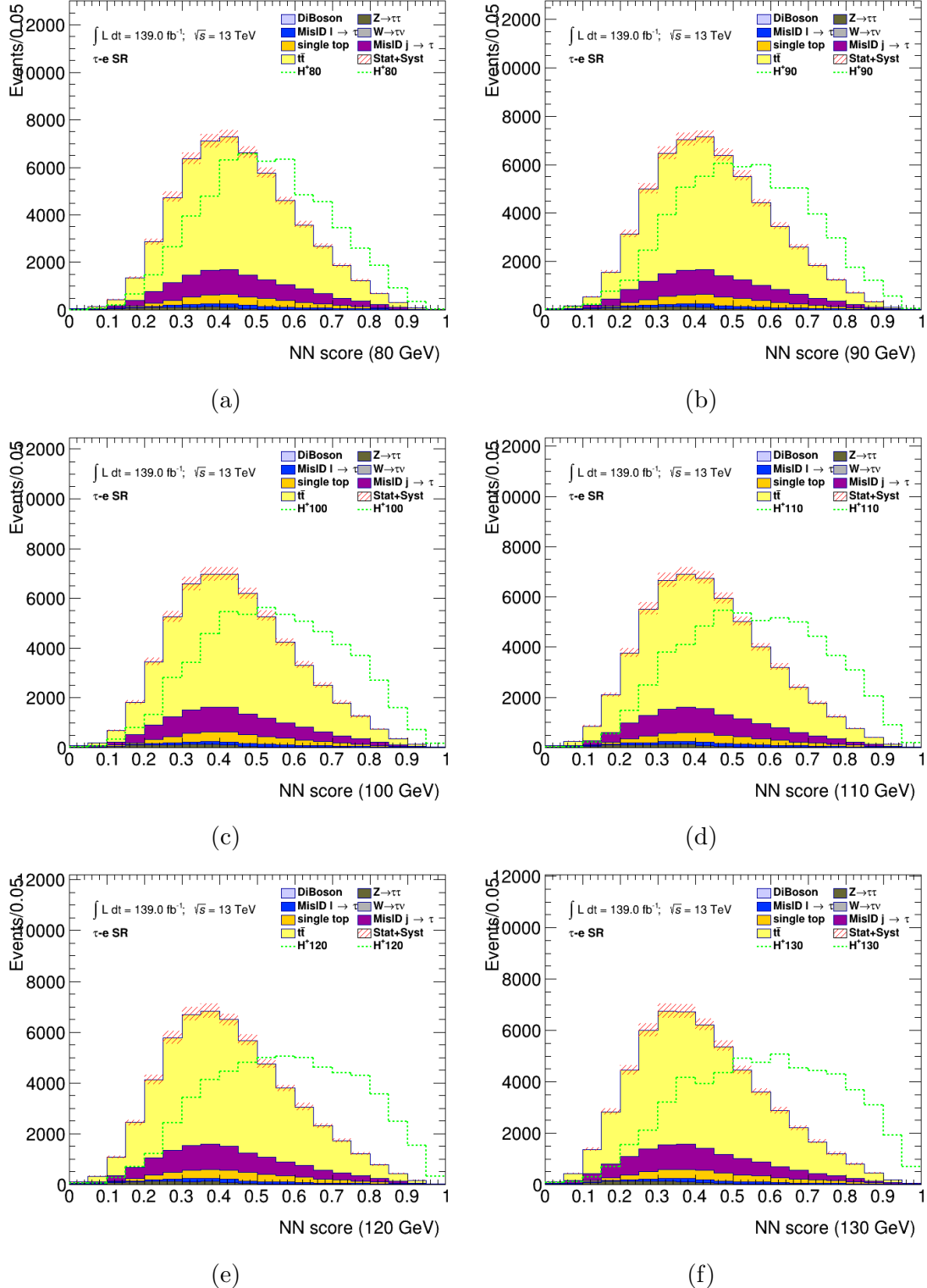


Figure D.13: PNN score distributions in the signal region of the $\tau + e$ channel, for the six charged Higgs boson mass parameters. The uncertainty bands include all statistical and systematic uncertainties. The normalization of the signal (shown for illustration) corresponds to the integral of the background.

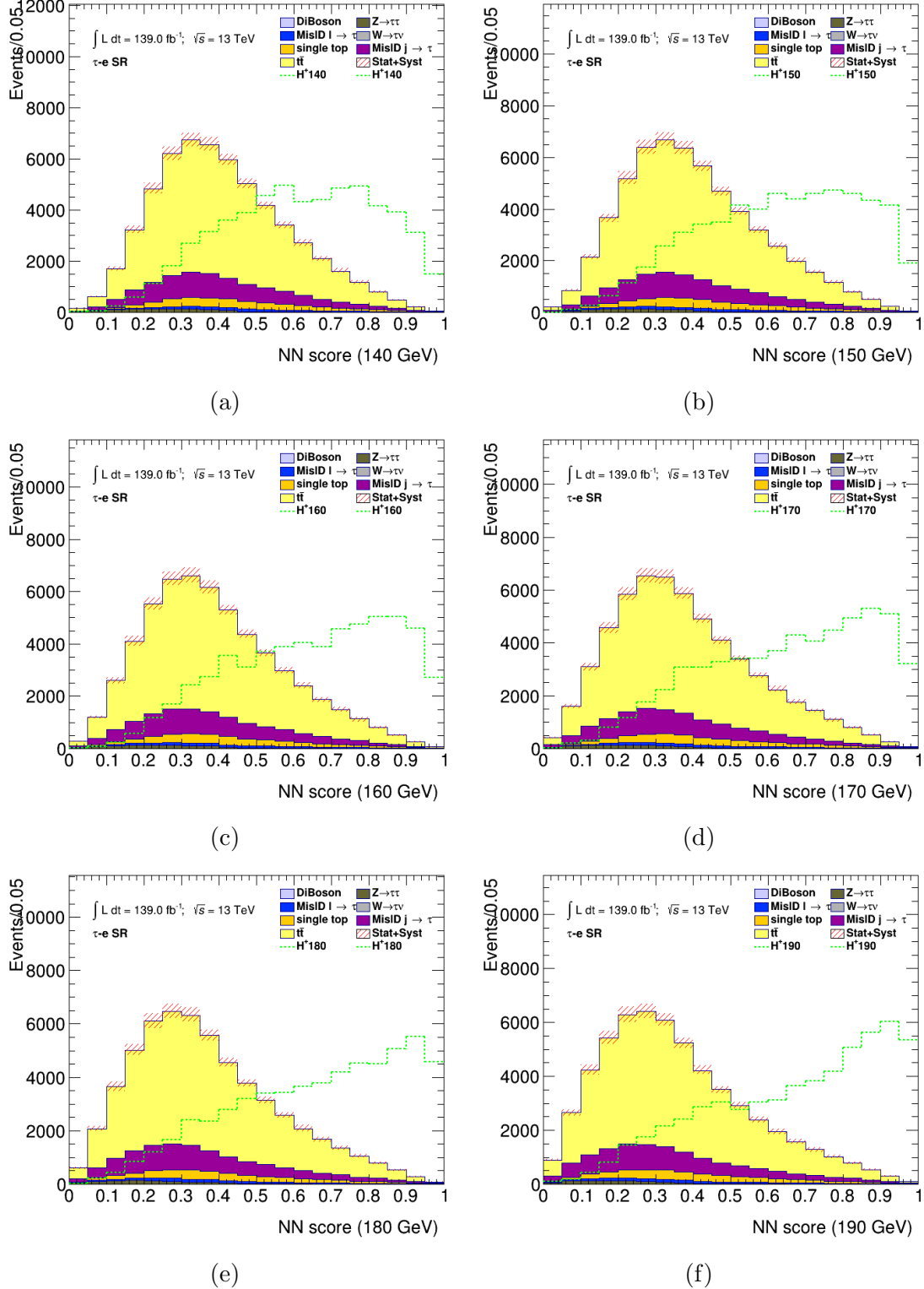


Figure D.14: PNN score distributions in the signal region of the $\tau + e$ channel, for the six charged Higgs boson mass parameters. The uncertainty bands include all statistical and systematic uncertainties. The normalization of the signal (shown for illustration) corresponds to the integral of the background.

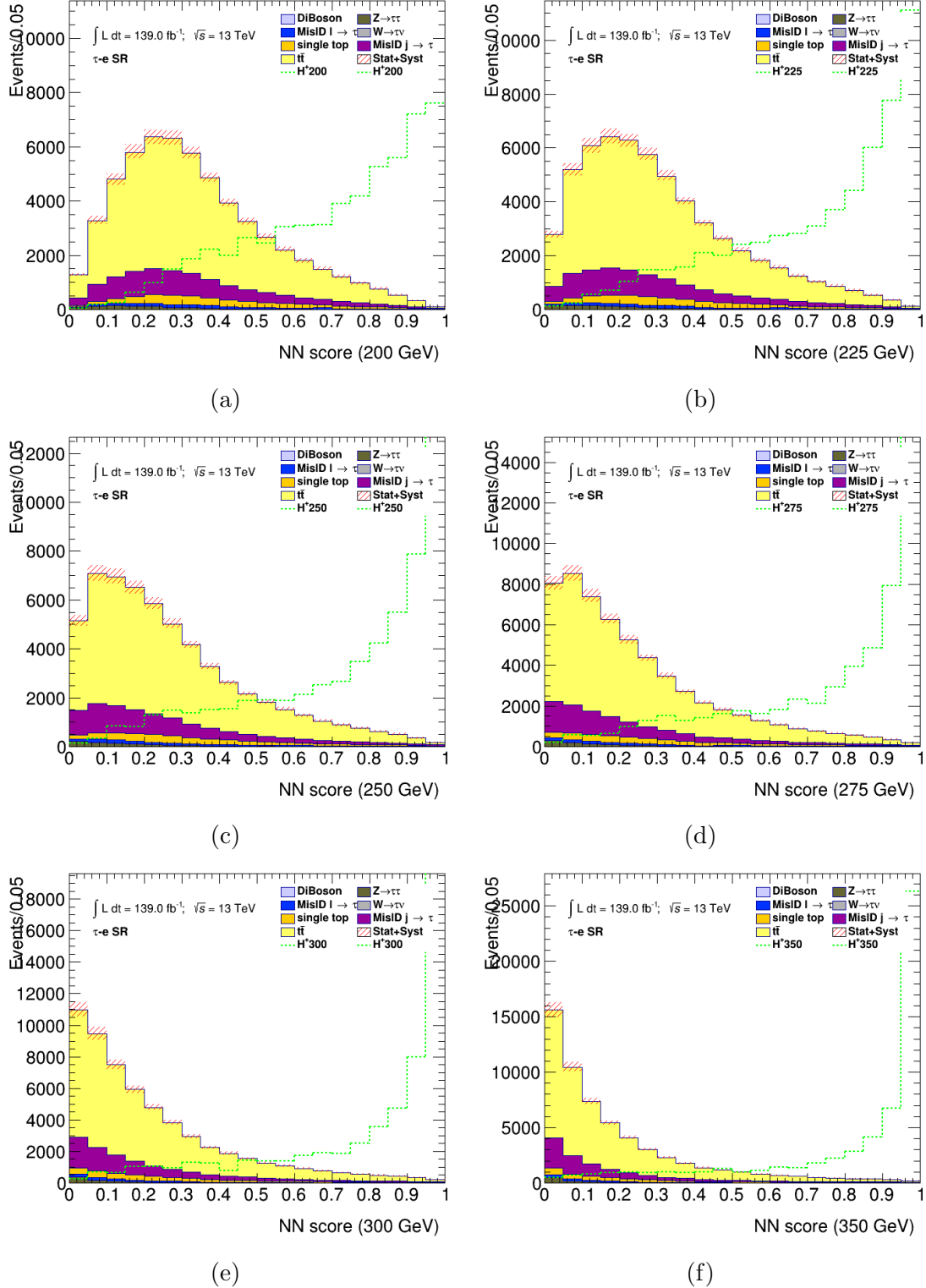


Figure D.15: PNN score distributions in the signal region of the $\tau + e$ channel, for the six charged Higgs boson mass parameters. The uncertainty bands include all statistical and systematic uncertainties. The normalization of the signal (shown for illustration) corresponds to the integral of the background.

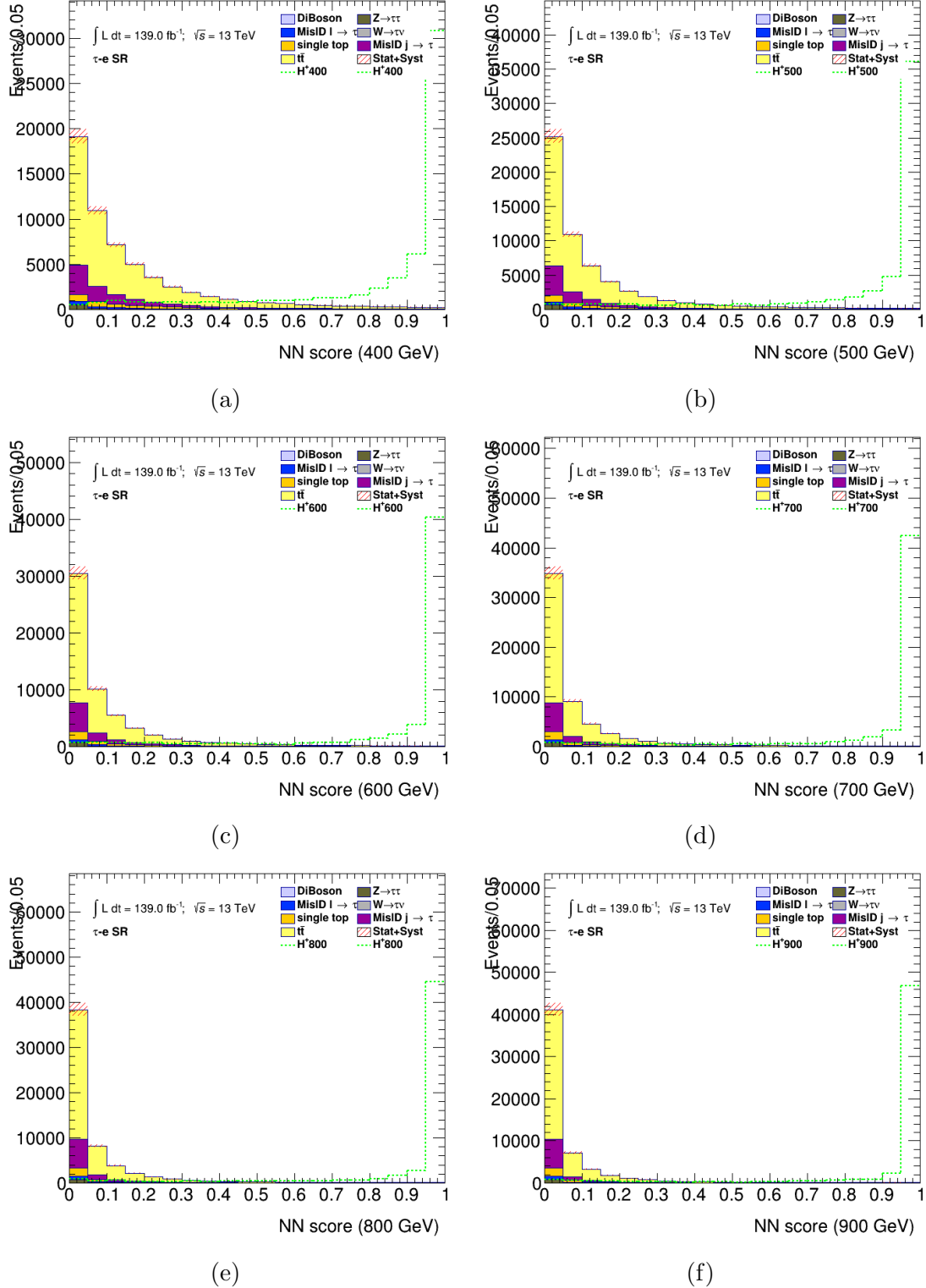


Figure D.16: PNN score distributions in the signal region of the $\tau+e$ channel, for the six charged Higgs boson mass parameters. The uncertainty bands include all statistical and systematic uncertainties. The normalization of the signal (shown for illustration) corresponds to the integral of the background.

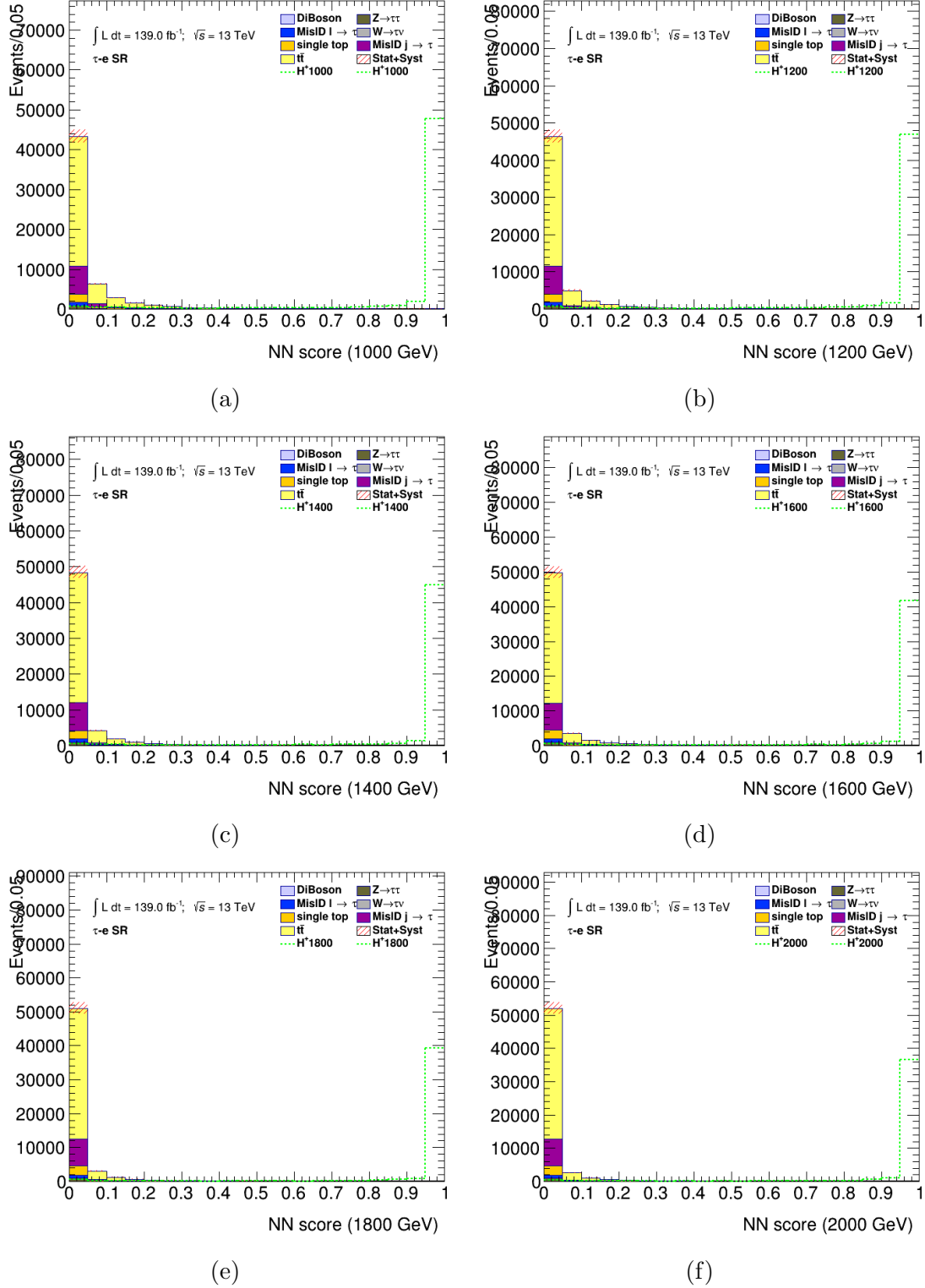


Figure D.17: PNN score distributions in the signal region of the $\tau + e$ channel, for the six charged Higgs boson mass parameters. The uncertainty bands include all statistical and systematic uncertainties. The normalization of the signal (shown for illustration) corresponds to the integral of the background.

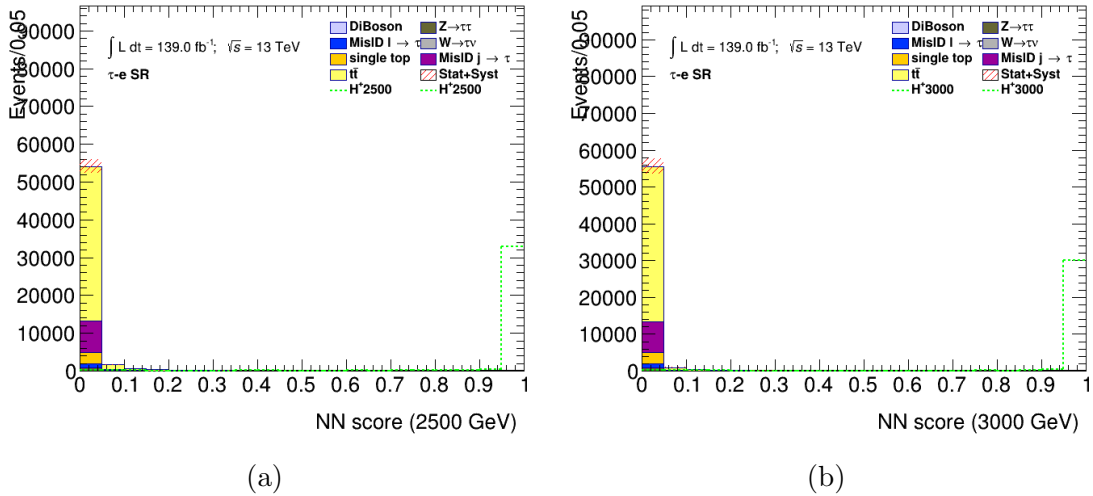


Figure D.18: PNN score distributions in the signal region of the $\tau+e$ channel, for the six charged Higgs boson mass parameters. The uncertainty bands include all statistical and systematic uncertainties. The normalization of the signal (shown for illustration) corresponds to the integral of the background.

D.4 $\tau + \mu$ PNN Scores

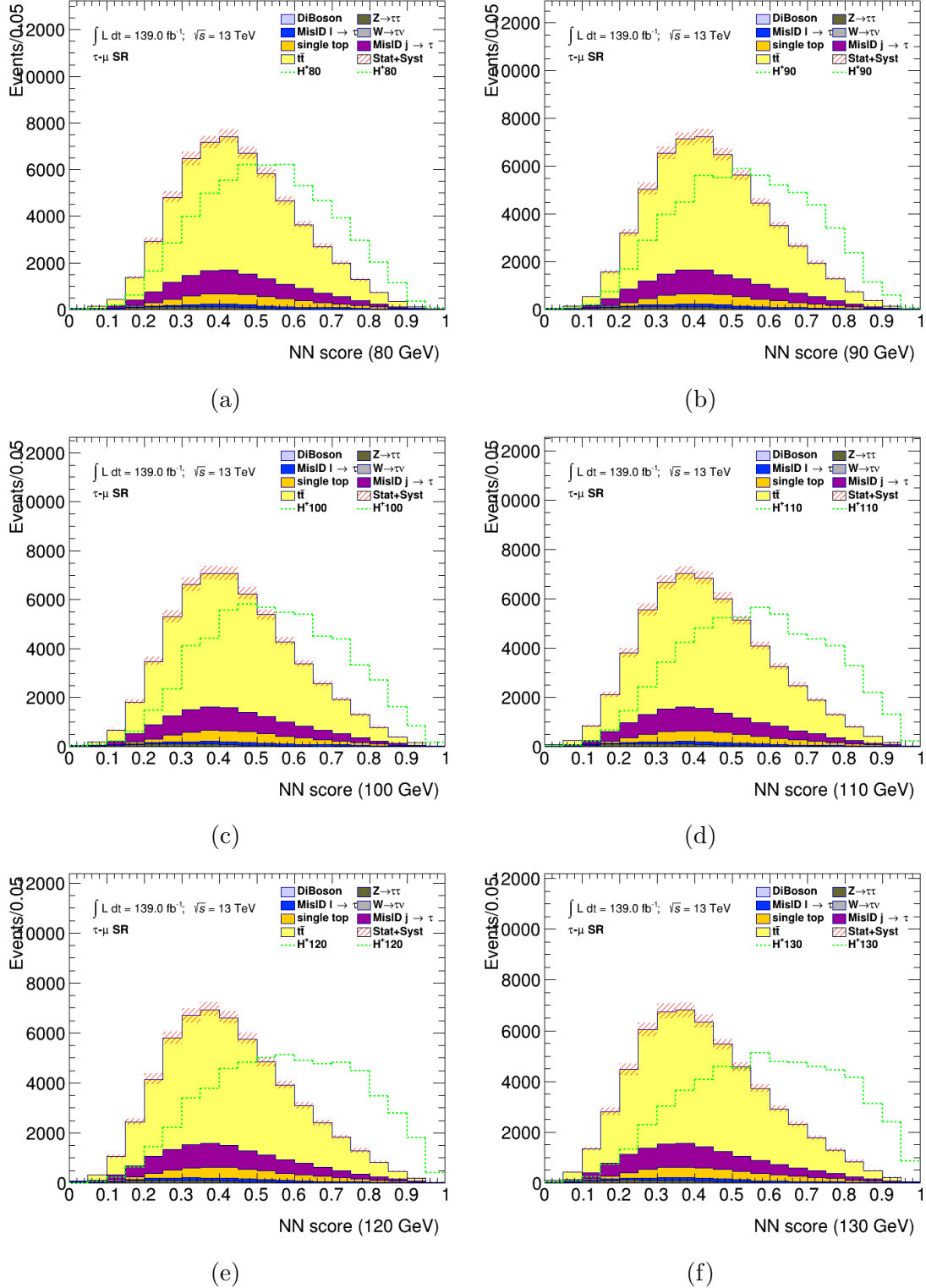


Figure D.19: PNN score distributions in the signal region of the $\tau+\mu$ channel, for the six charged Higgs boson mass parameters. The uncertainty bands include all statistical and systematic uncertainties. The normalization of the signal (shown for illustration) corresponds to the integral of the background.

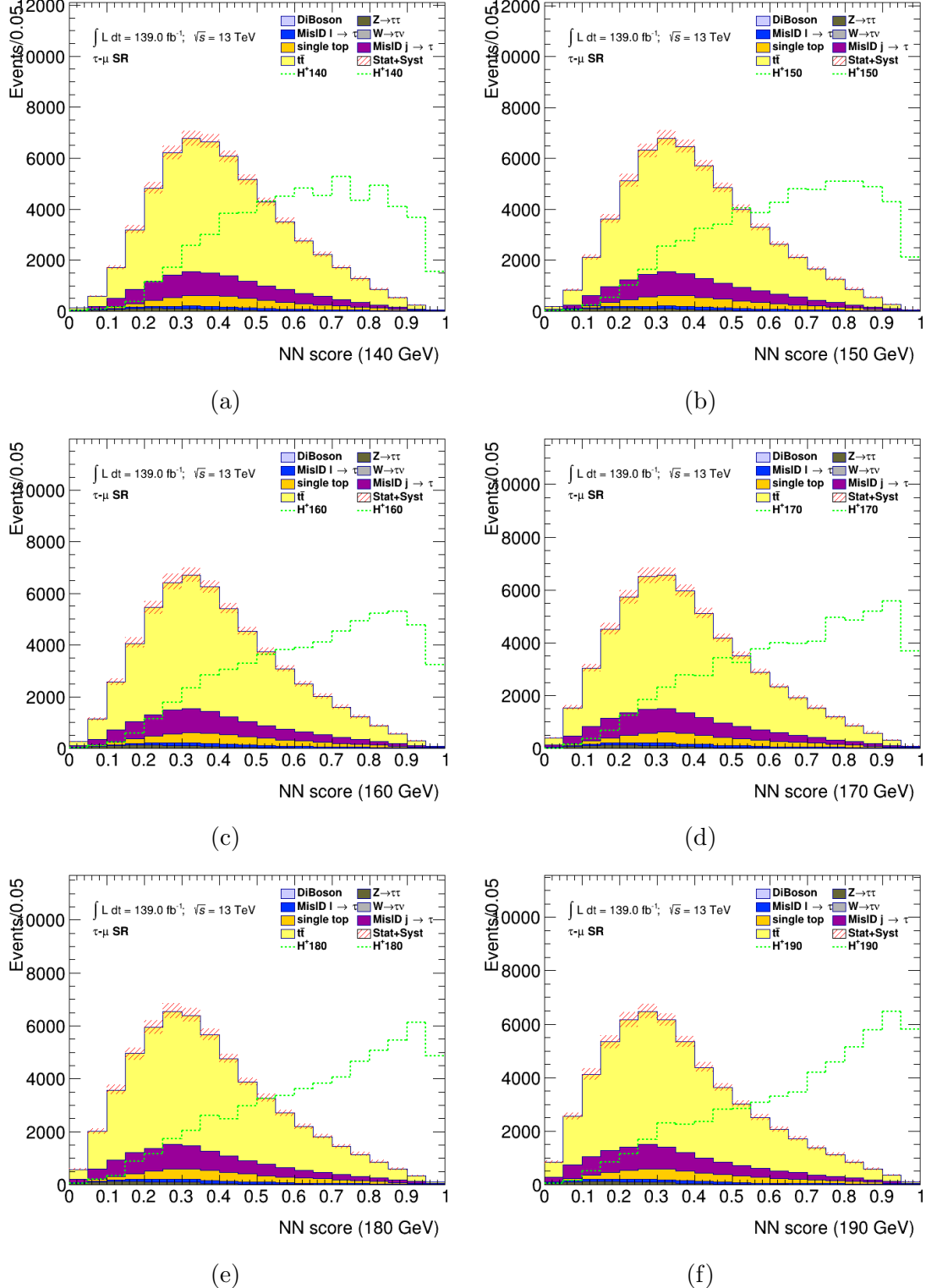


Figure D.20: PNN score distributions in the signal region of the $\tau+\mu$ channel, for the six charged Higgs boson mass parameters. The uncertainty bands include all statistical and systematic uncertainties. The normalization of the signal (shown for illustration) corresponds to the integral of the background.

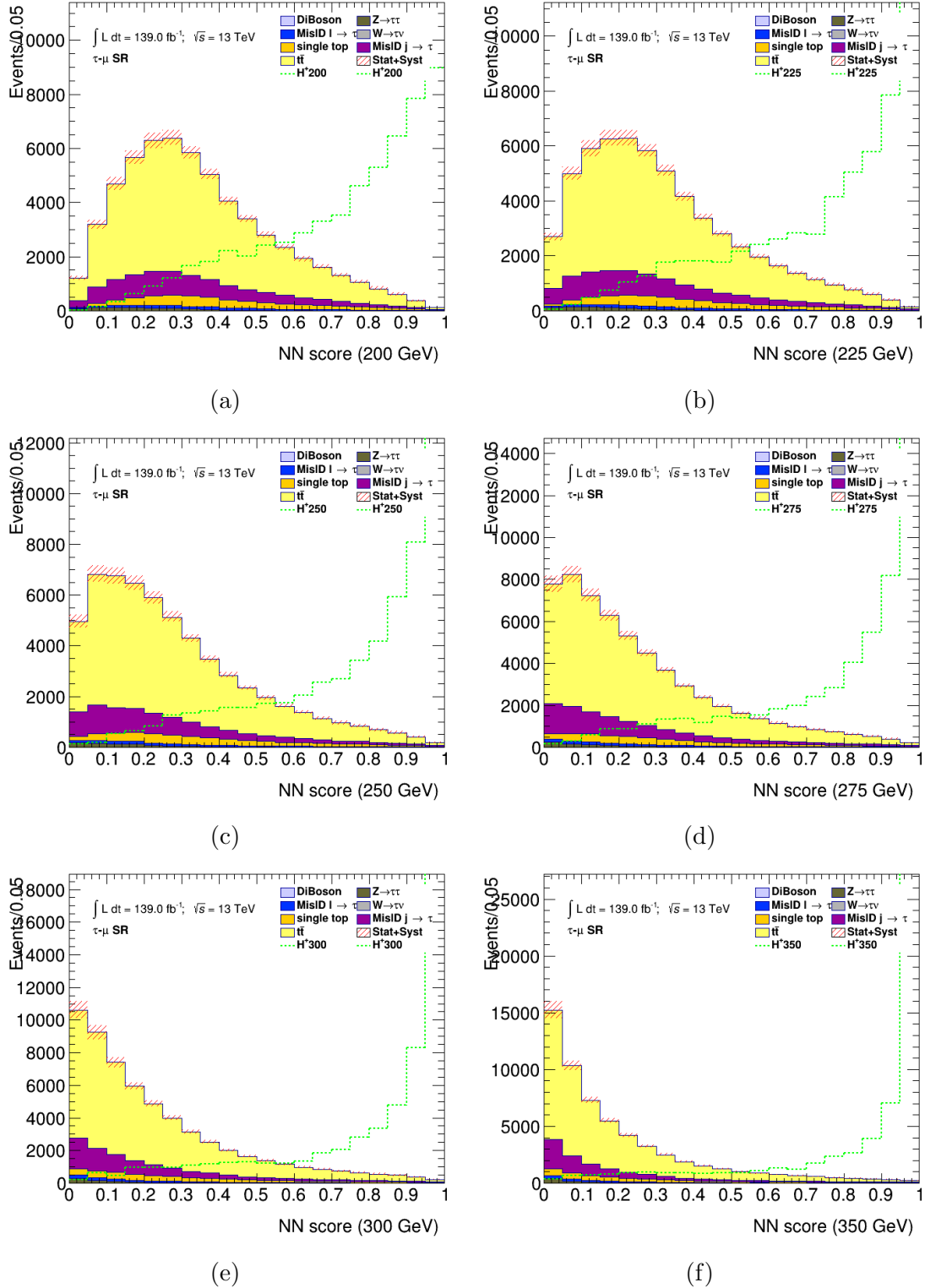


Figure D.21: PNN score distributions in the signal region of the $\tau+\mu$ channel, for the six charged Higgs boson mass parameters. The uncertainty bands include all statistical and systematic uncertainties. The normalization of the signal (shown for illustration) corresponds to the integral of the background.

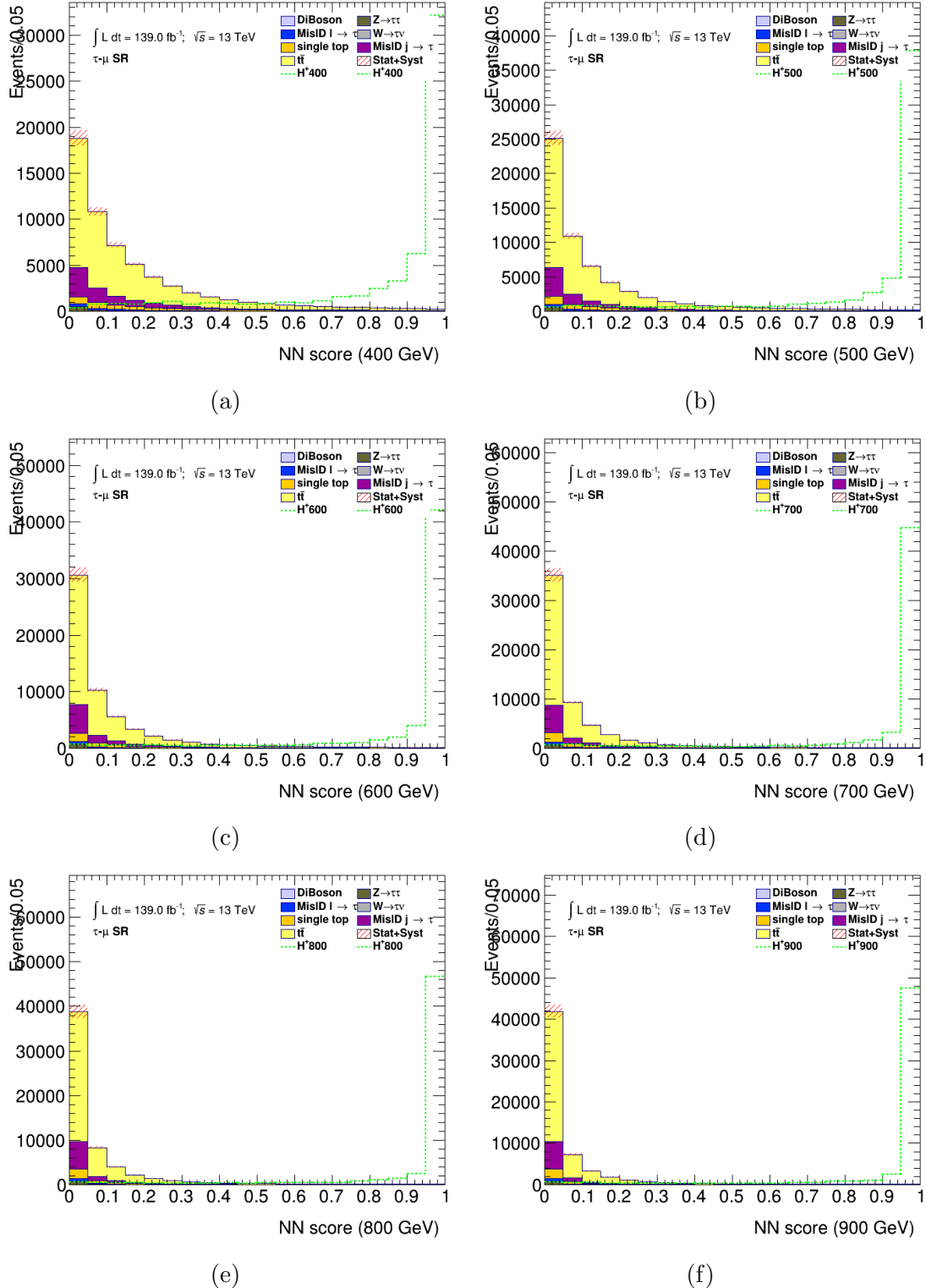


Figure D.22: PNN score distributions in the signal region of the $\tau+\mu$ channel, for the six charged Higgs boson mass parameters. The uncertainty bands include all statistical and systematic uncertainties. The normalization of the signal (shown for illustration) corresponds to the integral of the background.

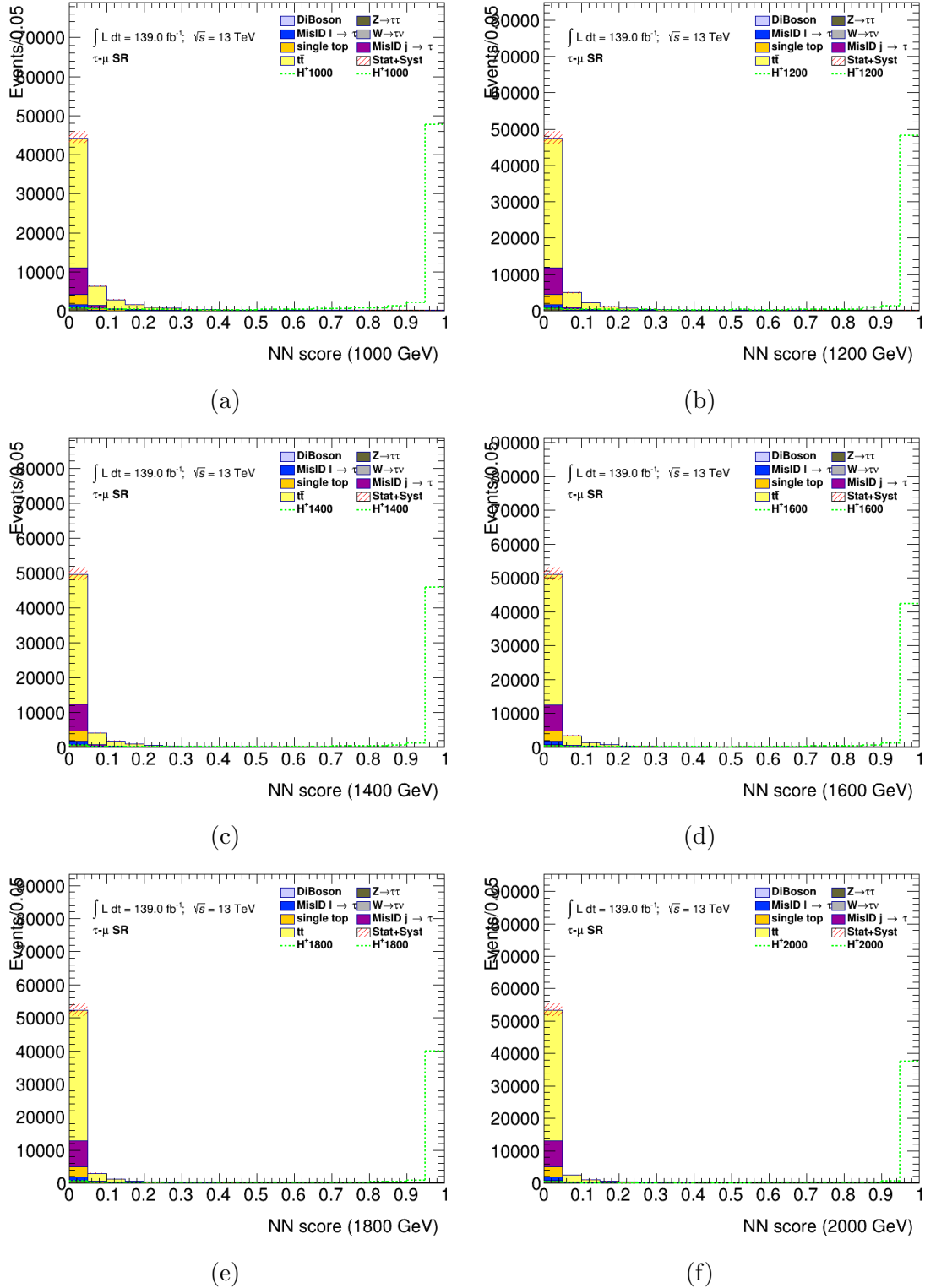


Figure D.23: PNN score distributions in the signal region of the $\tau + \mu$ channel, for the six charged Higgs boson mass parameters. The uncertainty bands include all statistical and systematic uncertainties. The normalization of the signal (shown for illustration) corresponds to the integral of the background.

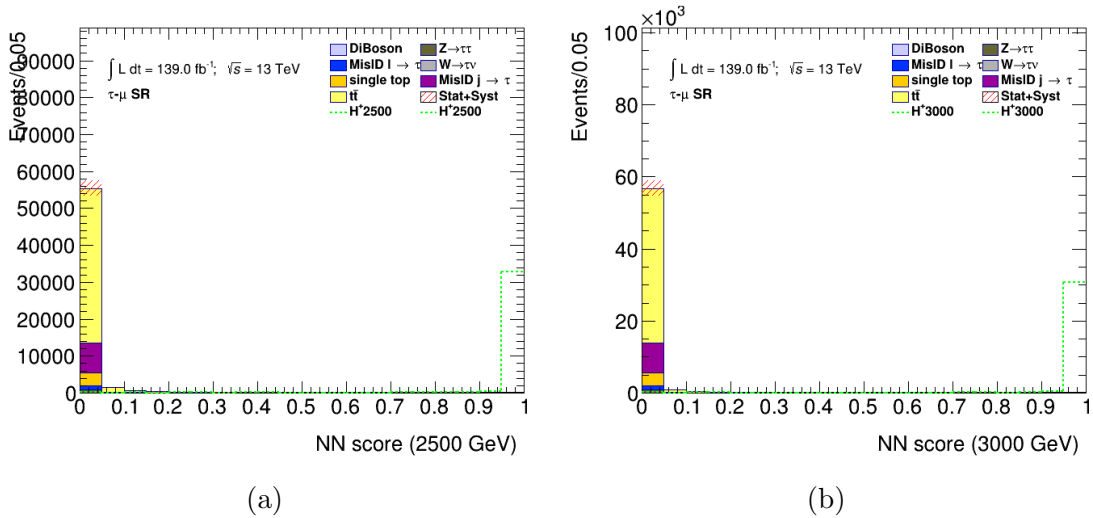


Figure D.24: PNN score distributions in the signal region of the $\tau + \mu$ channel, for the six charged Higgs boson mass parameters. The uncertainty bands include all statistical and systematic uncertainties. The normalization of the signal (shown for illustration) corresponds to the integral of the background.

ACRONYMS

2HDM 2-Higgs Doublet Model. ix, 3, 14, 99

ADC Analog to Digital Converter. 104

ATLAS A Toroidal LHC Apparatus. vi, ix, xiii, xiv, 1, 10, 14, 16, 23, 28, 29, 30, 31, 32, 33, 34, 38, 39, 42, 43, 44, 46, 47, 49, 50, 51, 52, 60, 61, 99, 102

AUC Area Under the Curve. x, xi, xvi, 84, 85, 87, 88

BDT Boosted Decision Tree. xv, 63, 79

BSM Beyond the Standard Model. 1

CB Combined μ Identification Strategy. 52

CERN Conseil Européen pour la Recherche Nucléaire. 1, 10, 23

CIS Charge Injection System. 103

CMS Compact Muon Solenoid. 10, 14, 23, 30

CR Control Region. 63, 66, 73, 110

CSC Cathode Strip Chamber. 42

CT Calorimeter-Tagged μ Identification Strategy. 53

DQ Data Quality. 102

DQM Data Quality Monitoring. 102

EM Electromagnetism. 5, 6, 7, 39, 40, 54, 103

EMB LAr Electromagnetic Main Barrel. xiv, 39, 40

EMEC LAr Electromagnetic End-Cap. 39, 40

FCAL LAr Forward Calorimeter. 39

FF Fake Factor. xv, 72, 73, 74

HEC LAr Hadronic End-Cap. 39

HLT High Level Trigger. 44, 45

HPO Hyperparameter Optimization. x, xi, 84, 87

IBL Insertable B Layer. 35, 36

ID Inner Detector. 33, 34, 35, 36, 51, 52, 53, 54, 60

IO Inside-Out μ Identification Strategy. 53

IOV Interval of Validity. 103

IP Interaction Point. xiv, 31, 34, 35, 36, 40, 41, 59

L1 Trigger Level-1 Trigger. 44

LAr Liquid Argon. 38, 39, 40, 186, 187

LB Luminosity Block. 102, 103

LHC Large Hadron Collider. ix, xiii, 1, 23, 24, 26, 29, 30, 31, 43, 102, 103

LL Leading-Logarithmic Order. 46

LO Leading Order. 46, 68

MC Monte Carlo. 46, 47, 49, 50, 68, 70, 72, 74, 79, 81

- MDT** Monitored Drift Tube. 42
- ME** Matrix Element. 46
- MS** Muon Spectrometer. 42, 52, 53
- MSSM** Minimal Supersymmetric Standard Model. v, ix, xii, xiii, 3, 12, 13, 14, 15, 17, 21, 83
- MVA** Multivariate Analysis Technique. 63
- NLO** Next-to-Leading Order. 46, 68
- NN** Neural Network. 80
- PDF** Parton Distribution Function. 46, 68
- PMT** Photomultiplier Tube. 41, 103
- PNN** Parameterized Neural Network. 1, x, xv, xvi, xxiii, xxiv, xxv, xxvi, 63, 79, 80, 81, 82, 83, 84, 85, 94, 95, 96, 97, 99, 156, 158, 159, 160, 161, 162, 163, 165, 166, 167, 168, 169, 170, 172, 173, 174, 175, 176, 177, 179, 180, 181, 182, 183, 184
- QCD** Quantum Chromodynamics. 6, 7, 63, 72
- QED** Quantum Electrodynamics. 6
- QFT** Quantum Field Theory. 3, 5, 6, 7
- RNN** Recurrent Neural Network. 61, 73
- RPC** Resistive Plate Chamber. 42
- SCT** Semiconductor Tracker. 34, 36, 51

SM Standard Model. ix, xvi, 1, 3, 4, 5, 6, 8, 9, 10, 11, 12, 13, 22, 61, 70, 95, 96, 97, 99

SR Signal Region. xi, 63, 89, 90, 91, 94, 99, 110

ST Segmented-tagged μ Identification Strategy. 53

SUSY Supersymmetry. 3, 11, 12, 16

TDAQ Trigger and Data Acquisition. xiv, 30, 43, 44, 45

TGC Thin Gap Chamber. 42

TileCal Tile Calorimeter. xiv, xvi, xvii, 40, 41, 42, 102, 103, 104, 105, 106

TRT Transition Radiation Tracker. 34, 36, 37, 38, 51

VEV Vacuum Expectation Value. 8

WP Working Point. 53, 54, 61

BIBLIOGRAPHY

- [1] D. Hemphill. *The behavior of the primordial universe*. Apr. 2020.
URL: https://www.physics.purdue.edu/about/prizes_awards/charlotte_ida_litman_tubis_award/2017_behavior_primordial_universe.html.
- [2] R. L. Workman et al. “Review of Particle Physics”. *PTEP* 2022 (2022), p. 083C01.
DOI: 10.1093/ptep/ptac097.
- [3] P. W. Higgs. “Broken Symmetries and the Masses of Gauge Bosons”.
Phys. Rev. Lett. 13 (16 Oct. 1964), pp. 508–509. DOI: 10.1103/PhysRevLett.13.508.
URL: <https://link.aps.org/doi/10.1103/PhysRevLett.13.508>.
- [4] F. Englert and R. Brout. “Broken Symmetry and the Mass of Gauge Vector Mesons”.
Phys. Rev. Lett. 13 (9 Aug. 1964), pp. 321–323. DOI: 10.1103/PhysRevLett.13.321.
URL: <https://link.aps.org/doi/10.1103/PhysRevLett.13.321>.
- [5] J. Ellis. “Higgs Physics” (Dec. 2013). 52 pages, 45 figures, Lectures presented at the ESHEP 2013 School of High-Energy Physics, to appear as part of the proceedings in a CERN Yellow Report, 117–168. 52 p. DOI: 10.5170/CERN-2015-004.117.
arXiv: 1312.5672. URL: <https://cds.cern.ch/record/1638469>.
- [6] ATLAS Collaboration. “Observation of a new particle in the search for the Standard Model Higgs boson with the ATLAS detector at the LHC”.
Physics Letters B 716.1 (2012), pp. 1–29.
- [7] CMS Collaboration. “Observation of a new boson at a mass of 125 GeV with the CMS experiment at the LHC”. *Physics Letters B* 716.1 (Sept. 2012), pp. 30–61.
DOI: 10.1016/j.physletb.2012.08.021.
URL: <https://doi.org/10.1016%2Fj.physletb.2012.08.021>.
- [8] G. Branco et al. “Theory and phenomenology of two-Higgs-doublet models”.
Physics Reports 516.1–2 (July 2012), pp. 1–102. ISSN: 0370-1573.

DOI: [10.1016/j.physrep.2012.02.002](https://doi.org/10.1016/j.physrep.2012.02.002).

URL: <http://dx.doi.org/10.1016/j.physrep.2012.02.002>.

- [9] ATLAS Collaboration. *Summary plots for beyond Standard Model Higgs boson benchmarks for direct and indirect searches*. Tech. rep.

All figures including auxiliary figures are available at

<https://atlas.web.cern.ch/Atlas/GROUPS/PHYSICS/PUBNOTES/ATL-PHYS-PUB-2022-043>. Geneva: CERN, 2022. URL: <http://cds.cern.ch/record/2827098>.

- [10] The ATLAS Collaboration. “Search for charged Higgs bosons decaying via $H^\pm \rightarrow \tau^\pm \nu_\tau$ in the $\tau + \text{jets}$ and $\tau + \text{lepton}$ final states with 36 fb^{-1} of pp collision data recorded at $\sqrt{s} = 13 \text{ TeV}$ with the ATLAS experiment”. *JHEP* 09 (2018), p. 139.

DOI: [10.1007/JHEP09\(2018\)139](https://doi.org/10.1007/JHEP09(2018)139). arXiv: 1807.07915 [hep-ex].

- [11] C. T. Dalla Potter. *Handbook of LHC Higgs Cross Sections: 3. Higgs Properties: Report of the LHC Higgs Cross Section Working Group*. en. 2013.

DOI: [10.5170/CERN-2013-004](https://doi.org/10.5170/CERN-2013-004). URL: <http://cds.cern.ch/record/1559921>.

- [12] M. Carena et al. “MSSM Higgs boson searches at the LHC: benchmark scenarios after the discovery of a Higgs-like particle”.

The European Physical Journal C 73.9 (Sept. 2013).

DOI: [10.1140/epjc/s10052-013-2552-1](https://doi.org/10.1140/epjc/s10052-013-2552-1).

URL: <https://doi.org/10.1140%2Fepjc%2Fs10052-013-2552-1>.

- [13] A. Djouadi et al. “The post-Higgs MSSM scenario: habemus MSSM?”

The European Physical Journal C 73.12 (Nov. 2013).

DOI: [10.1140/epjc/s10052-013-2650-0](https://doi.org/10.1140/epjc/s10052-013-2650-0).

URL: <https://doi.org/10.1140%2Fepjc%2Fs10052-013-2650-0>.

- [14] CMS Collaboration. “Search for charged Higgs bosons in the $H^\pm \rightarrow \tau^\pm \nu_\tau$ decay channel in proton-proton collisions at $\sqrt{s} = 13 \text{ TeV}$ ”.

Journal of High Energy Physics 2019.7 (July 2019). DOI: 10.1007/jhep07(2019)142.

URL: <https://doi.org/10.1007%2Fjhep07%282019%29142>.

- [15] ATLAS collaboration. “Search for charged Higgs bosons decaying into a top quark and a bottom quark at $\sqrt{s} = 13$ TeV with the ATLAS detector”. *Journal of High Energy Physics* 2021.6 (2021), p. 145. DOI: 10.1007/JHEP06(2021)145. URL: [https://doi.org/10.1007/JHEP06\(2021\)145](https://doi.org/10.1007/JHEP06(2021)145).
- [16] L. R. Evans and P. Bryant. “LHC Machine”. *JINST* 3 (2008). This report is an abridged version of the LHC Design Report (CERN-2004-003), S08001. 164 p. DOI: 10.1088/1748-0221/3/08/S08001. URL: <https://cds.cern.ch/record/1129806>.
- [17] CERN. *Facts and figures about the LHC*. URL: <https://home.cern/resources/faqs/facts-and-figures-about-lhc>.
- [18] X. C. Vidal and R. C. Manzano. *Lorentz Force Taking a closer look at LHC*. URL: https://www.lhc-closer.es/taking_a_closer_look_at_lhc/0.lorentz_force.
- [19] E. Lopienska. “The CERN accelerator complex, layout in 2022. Complexe des accélérateurs du CERN en janvier 2022” (Feb. 2022). General Photo. URL: <https://cds.cern.ch/record/2800984>.
- [20] ATLAS Collaboration. *Public atlas luminosity results for run-2 of the LHC*. URL: https://twiki.cern.ch/twiki/bin/view/AtlasPublic/LuminosityPublicResultsRun2#Integrated_and_Instantaneous_Lum.
- [21] ATLAS Collaboration. *Event displays from run 2 physics analyses not included in publications*. URL: <https://twiki.cern.ch/twiki/bin/view/AtlasPublic/EventDisplayRun2Physics>.

- [22] ATLAS Collaboration. “The ATLAS Experiment at the CERN Large Hadron Collider”. *JINST* 3 (2008). Also published by CERN Geneva in 2010, S08003. 437 p. DOI: 10.1088/1748-0221/3/08/S08003. URL: <https://cds.cern.ch/record/1129811>.
- [23] ATLAS Collaboration. *Atlas schematics*. URL: <https://atlas.cern/Resources/Schematics>.
- [24] *Pseudorapidity*. Wikipedia, Feb. 2009. URL: <https://en.wikipedia.org/wiki/File:Pseudorapidity2.png>.
- [25] ATLAS Collaboration. *ATLAS central solenoid: Technical Design Report*. Technical design report. ATLAS. Electronic version not available. Geneva: CERN, 1997. DOI: 10.17181/CERN.ZZVJ.2JYE. URL: <https://cds.cern.ch/record/331067>.
- [26] ATLAS Collaboration. *ATLAS tile calorimeter: Technical Design Report*. Technical design report. ATLAS. Geneva: CERN, 1996. DOI: 10.17181/CERN.JRBJ.7028. URL: <https://cds.cern.ch/record/331062>.
- [27] J. P. Badiou et al. *ATLAS barrel toroid: Technical Design Report*. Technical design report. ATLAS. Electronic version not available. Geneva: CERN, 1997. DOI: 10.17181/CERN.RF2A.CP5T. URL: <https://cds.cern.ch/record/331065>.
- [28] N. Wermes and G. Hallewel. *ATLAS pixel detector: Technical Design Report*. Technical design report. ATLAS. Geneva: CERN, 1998. URL: <https://cds.cern.ch/record/381263>.

- [29] M. Capeans et al. “ATLAS Insertable B-Layer Technical Design Report” (Sept. 2010). URL: <https://cds.cern.ch/record/1291633>.
- [30] ATLAS Collaboration. *ATLAS inner detector: Technical Design Report, 1*. Technical design report. ATLAS. Geneva: CERN, 1997. URL: <https://cds.cern.ch/record/331063>.
- [31] ATLAS Collaboration. “The ATLAS Experiment at the CERN Large Hadron Collider”. *Journal of Instrumentation* 3.08 (Aug. 2008), S08003–S08003. DOI: 10.1088/1748-0221/3/08/s08003. URL: <https://doi.org/10.1088/1748-0221/3/08/s08003>.
- [32] *ATLAS liquid-argon calorimeter: Technical Design Report*. Technical design report. ATLAS. Geneva: CERN, 1996. DOI: 10.17181/CERN.FWRW.F00Q. URL: <https://cds.cern.ch/record/331061>.
- [33] ATLAS Collaboration. *ATLAS muon spectrometer: Technical Design Report*. Technical design report. ATLAS. Geneva: CERN, 1997. URL: <https://cds.cern.ch/record/331068>.
- [34] ATLAS Collaboration. “Operation of the ATLAS trigger system in Run 2”. *Journal of Instrumentation* 15.10 (Oct. 2020), P10004–P10004. DOI: 10.1088/1748-0221/15/10/p10004. URL: <https://doi.org/10.1088/1748-0221/15/10/p10004>.
- [35] ATLAS Collaboration. *ATLAS DAQ Approved Plots*. URL: <https://twiki.cern.ch/twiki/bin/view/AtlasPublic/ApprovedPlotsDAQ>.

- [36] C. Wanotayaroj. “Search for a Scalar Partner of the Top Quark in the Jets+MET Final State with the ATLAS detector”. Presented 25 Oct 2016. Nov. 2016.
 URL: <http://cds.cern.ch/record/2242196>.
- [37] C. Bierlich et al. *A comprehensive guide to the physics and usage of PYTHIA 8.3*. 2022. DOI: 10.48550/ARXIV.2203.11601.
 URL: <https://arxiv.org/abs/2203.11601>.
- [38] S. Alioli et al. “A general framework for implementing NLO calculations in shower Monte Carlo programs: the POWHEG BOX”.
Journal of High Energy Physics 2010.6 (June 2010). DOI: 10.1007/jhep06(2010)043.
 URL: <https://doi.org/10.1007%2Fjhep06%282010%29043>.
- [39] S. Frixione, G. Ridolfi, and P. Nason. “A positive-weight next-to-leading-order Monte Carlo for heavy flavour hadroproduction”.
Journal of High Energy Physics 2007.09 (Sept. 2007), pp. 126–126.
 DOI: 10.1088/1126-6708/2007/09/126.
 URL: <https://doi.org/10.1088%2F1126-6708%2F2007%2F09%2F126>.
- [40] T. Gleisberg et al. “Event generation with SHERPA 1.1”.
Journal of High Energy Physics 2009.02 (Feb. 2009), pp. 007–007.
 DOI: 10.1088/1126-6708/2009/02/007.
 URL: <https://doi.org/10.1088%2F1126-6708%2F2009%2F02%2F007>.
- [41] S. Agostinelli et al. “Geant4 a simulation toolkit”.
Nuclear Instruments and Methods in Physics Research Section A: Accelerators, Spectrometers, Detectors and Associated Equipment 506.3 (2003), pp. 250–303.
 ISSN: 0168-9002. DOI: [https://doi.org/10.1016/S0168-9002\(03\)01368-8](https://doi.org/10.1016/S0168-9002(03)01368-8). URL:
<https://www.sciencedirect.com/science/article/pii/S0168900203013688>.

- [42] ATLAS Collaboration. “The ATLAS Simulation Infrastructure”. *The European Physical Journal C* 70.3 (Sept. 2010), pp. 823–874.
DOI: 10.1140/epjc/s10052-010-1429-9.
URL: <https://doi.org/10.1140%2Fepjc%2Fs10052-010-1429-9>.
- [43] ATLAS Collaboration. *Athena*. Version 22.0.1. Apr. 2019.
DOI: 10.5281/zenodo.2641997. URL: <https://doi.org/10.5281/zenodo.2641997>.
- [44] Garelli, Nicoletta on behalf of the ATLAS Collaboration.
“Performance of the ATLAS Detector in Run-2”. *EPJ Web Conf.* 164 (2017), p. 01021.
DOI: 10.1051/epjconf/201716401021.
URL: <https://doi.org/10.1051/epjconf/201716401021>.
- [45] ATLAS Collaboration. “Topological cell clustering in the ATLAS calorimeters and its performance in LHC Run 1”. *The European Physical Journal C* 77.7 (2017), p. 490.
DOI: 10.1140/epjc/s10052-017-5004-5.
URL: <https://doi.org/10.1140/epjc/s10052-017-5004-5>.
- [46] ATLAS Collaboration. “Muon reconstruction and identification efficiency in ATLAS using the full Run 2 pp collision data set at $\sqrt{s} = 13$ TeV”. *Eur. Phys. J. C* 81.7 (2021), p. 578. DOI: 10.1140/epjc/s10052-021-09233-2.
arXiv: 2012.00578 [hep-ex].
- [47] ATLAS Collaboration. “Electron and photon performance measurements with the ATLAS detector using the 2015–2017 LHC proton-proton collision data”. *Journal of Instrumentation* 14.12 (Dec. 2019), P12006–P12006.
DOI: 10.1088/1748-0221/14/12/p12006.
URL: <https://doi.org/10.1088/1748-0221/14/12/p12006>.
- [48] ATLAS Collaboration.
“Jet reconstruction and performance using particle flow with the ATLAS Detector”.

- The European Physical Journal C* 77.7 (2017), p. 466.
 DOI: 10.1140/epjc/s10052-017-5031-2.
 URL: <https://doi.org/10.1140/epjc/s10052-017-5031-2>.
- [49] M. Cacciari, G. P. Salam, and G. Soyez. “The anti- k_T jet clustering algorithm”.
Journal of High Energy Physics 2008.04 (Apr. 2008), pp. 063–063.
 DOI: 10.1088/1126-6708/2008/04/063.
 URL: <https://doi.org/10.48550/arXiv.0802.1189>.
- [50] M. Cacciari, G. P. Salam, and G. Soyez. “The catchment area of jets”.
Journal of High Energy Physics 2008.04 (Apr. 2008), pp. 005–005.
 DOI: 10.1088/1126-6708/2008/04/005.
 URL: <https://doi.org/10.1088/1126-6708/2008/04/005>.
- [51] ATLAS Collaboration. “Jet energy scale and resolution measured in proton–proton collisions at $\sqrt{s} = 13$ TeV with the ATLAS detector”.
The European Physical Journal C 81.8 (2021), p. 689.
 DOI: 10.1140/epjc/s10052-021-09402-3.
 URL: <https://doi.org/10.1140/epjc/s10052-021-09402-3>.
- [52] P. O. Hansson Adrian. “The ATLAS b -jet Trigger”
 (Nov. 2011). Comments: 4 pages, 6 figures, conference proceedings for PIC2011.
 arXiv: 1111.4190. URL: <https://cds.cern.ch/record/1397942>.
- [53] ATLAS Collaboration. “Optimisation and performance studies of the ATLAS b -tagging algorithms for the 2017-18 LHC run”
 (July 2017). All figures including auxiliary figures are available at
<https://atlas.web.cern.ch/Atlas/GROUPS/PHYSICS/PUBNOTES/ATL-PHYS-PUB-2017-013>. URL: <http://cds.cern.ch/record/2273281>.

- [54] ATLAS Collaboration. “Expected performance of the ATLAS b -tagging algorithms in Run-2” (July 2015). All figures including auxiliary figures are available at <https://atlas.web.cern.ch/Atlas/GROUPS/PHYSICS/PUBNOTES/ATL-PHYS-PUB-2015-022>. URL: <https://cds.cern.ch/record/2037697>.
- [55] ATLAS Collaboration. “Identification and energy calibration of hadronically decaying tau leptons with the ATLAS experiment in pp collisions at $\sqrt{s} = 8$ TeV”. *The European Physical Journal C* 75.7 (2015), p. 303.
DOI: [10.1140/epjc/s10052-015-3500-z](https://doi.org/10.1140/epjc/s10052-015-3500-z).
URL: <https://doi.org/10.1140/epjc/s10052-015-3500-z>.
- [56] ATLAS Collaboration. “Identification of hadronic tau lepton decays using neural networks in the ATLAS experiment” (2019). All figures including auxiliary figures are available at <https://atlas.web.cern.ch/Atlas/GROUPS/PHYSICS/PUBNOTES/ATL-PHYS-PUB-2019-033>. URL: <https://cds.cern.ch/record/2688062>.
- [57] ATLAS Collaboration. “ E_T^{miss} performance in the ATLAS detector using 2015-2016 LHC p-p collisions” (June 2018). All figures including auxiliary figures are available at <https://atlas.web.cern.ch/Atlas/GROUPS/PHYSICS/CONFNOTES/ATLAS-CONF-2018-023>. URL: <https://cds.cern.ch/record/2625233>.
- [58] ATLAS Collaboration. “Luminosity determination in pp collisions at $\sqrt{s} = 13$ TeV using the ATLAS detector at the LHC” (June 2019). All figures including auxiliary figures are available at <https://atlas.web.cern.ch/Atlas/GROUPS/PHYSICS/CONFNOTES/ATLAS-CONF-2019-021>. URL: <http://cds.cern.ch/record/2677054>.

- [59] R. D. Ball et al. “Parton distributions for the LHC run II”.
Journal of High Energy Physics 2015.4 (Apr. 2015). doi: 10.1007/jhep04(2015)040.
 URL: <https://doi.org/10.1007%2Fjhep04%282015%29040>.
- [60] R. D. Ball et al. “Parton distributions with LHC data”.
Nuclear Physics B 867.2 (Feb. 2013), pp. 244–289.
 DOI: 10.1016/j.nuclphysb.2012.10.003.
 URL: <https://doi.org/10.1016%2Fj.nuclphysb.2012.10.003>.
- [61] ATLAS Collaboration. “A study of optimal parameter setting for MADGRAPH5_AMC@NLO + PYTHIA 8 matched setup” (Nov. 2015). All figures including auxiliary figures are available at <https://atlas.web.cern.ch/Atlas/GROUPS/PHYSICS/PUBNOTES/ATL-PHYS-PUB-2015-048>. URL: <https://cds.cern.ch/record/2103221>.
- [62] P. Baldi et al. “Parameterized neural networks for high-energy physics”.
The European Physical Journal C 76.5 (2016), p. 235.
 DOI: 10.1140/epjc/s10052-016-4099-4.
 URL: <https://doi.org/10.1140/epjc/s10052-016-4099-4>.
- [63] Keras. URL: <https://keras.io/>.
- [64] Martín Abadi et al.
TensorFlow: Large-Scale Machine Learning on Heterogeneous Systems.
 Software available from tensorflow.org. 2015. URL: <https://www.tensorflow.org/>.
- [65] N. Srivastava et al.
 “Dropout: A Simple Way to Prevent Neural Networks from Overfitting”.
Journal of Machine Learning Research 15.56 (2014), pp. 1929–1958.
 URL: <http://jmlr.org/papers/v15/srivastava14a.html>.

- [66] B. Burghgrave. “Search for charged Higgs Bosons in the $\tau +$ lepton final state with 36.1 fb^{-1} of pp collision data recorded at $\sqrt{s} = 13 \text{ TeV}$ with the ATLAS experiment”. PhD thesis. Northern Illinois U., 2018.
- [67] ATLAS Collaboration. “Measurement of τ polarization in $W \rightarrow \tau\nu$ decays with the ATLAS detector in pp collisions at $\sqrt{s} = 7 \text{ TeV}$ ”. *The European Physical Journal C* 72.7 (July 2012).
 DOI: [10.1140/epjc/s10052-012-2062-6](https://doi.org/10.1140/epjc/s10052-012-2062-6).
 URL: <https://doi.org/10.1140%2Fepjc%2Fs10052-012-2062-6>.
- [68] ATLAS Collaboration. “Reconstruction, Energy Calibration, and Identification of Hadronically Decaying Tau Leptons in the ATLAS Experiment for Run-2 of the LHC” (2015). All figures including auxiliary figures are available at <https://atlas.web.cern.ch/Atlas/GROUPS/PHYSICS/PUBNOTES/ATL-PHYS-PUB-2015-045>. URL: <https://cds.cern.ch/record/2064383>.
- [69] ATLAS Collaboration. “Electron and photon energy calibration with the ATLAS detector using data collected in 2015 at $\sqrt{s} = 1 \text{ TeV}$ ” (2016). All figures including auxiliary figures are available at <https://atlas.web.cern.ch/Atlas/GROUPS/PHYSICS/PUBNOTES/ATL-PHYS-PUB-2016-015>. URL: <https://cds.cern.ch/record/2203514>.
- [70] ATLAS Collaboration. “Muon reconstruction performance of the ATLAS detector in proton–proton collision data at $\sqrt{s} = 13 \text{ TeV}$ ”. *The European Physical Journal C* 76.5 (2016), p. 292.
 DOI: [10.1140/epjc/s10052-016-4120-y](https://doi.org/10.1140/epjc/s10052-016-4120-y).
 URL: <https://doi.org/10.1140/epjc/s10052-016-4120-y>.
- [71] G. Cowan et al. “Asymptotic formulae for likelihood-based tests of new physics”. *The European Physical Journal C* 71.2 (Feb. 2011).

DOI: [10.1140/epjc/s10052-011-1554-0](https://doi.org/10.1140/epjc/s10052-011-1554-0).

URL: <https://doi.org/10.1140%2Fepjc%2Fs10052-011-1554-0>.

- [72] A. L. Read.

“Presentation of search results: Presentation of search results: the CL_s technique”.

Journal of Physics G: Nuclear and Particle Physics 28.10 (Sept. 2002), pp. 2693–2704.

DOI: [10.1088/0954-3899/28/10/313](https://doi.org/10.1088/0954-3899/28/10/313).

URL: <https://doi.org/10.1088/0954-3899/28/10/313>.

- [73] ATLAS Tile Collaboration and Parrish, Elliot.

“Operation and Performance of the ATLAS Tile Calorimeter and its readiness for Run 3” (2022). URL: <https://cds.cern.ch/record/2815951>.

- [74] ATLAS Collaboration.

“ATLAS data quality operations and performance for 2015–2018 data-taking”.

Journal of Instrumentation 15.04 (Apr. 2020), P04003–P04003.

DOI: [10.1088/1748-0221/15/04/p04003](https://doi.org/10.1088/1748-0221/15/04/p04003).

URL: <https://doi.org/10.1088/1748-0221/15/04/p04003>.